AD-A268 324

Atlas of Formability

Hastelloy C-22

93 8 17 04 9
~~92 12 28 069~~

93-19153

NCEMT

REPORT DOCUMENTATION PAGE

Public reporting burden for this collection of information is estimated to average 1 hour per response, including the time for reviewing instructions, searching existing data sources, gathering and maintaining the data needed, and completing and reviewing the collection of information. Send comments regarding this burden estimate or any other aspect of this collection of information, including suggestions for reducing this burden, to Washington Headquarters Services, Directorate for Information Operations and Reports, 1215 Jefferson Davis Highway, Suite 1204, Arlington, VA 22202-4302, and to the Office of Management and Budget, Paperwork Reduction Project (0704-0188), Washington, DC 20503

1. AGENCY USE ONLY (Leave blank)	2. REPORT DATE 30 Sept, 1992	3. REPORT TYPE AND DATES COVERED Final, 6/30/92 - 9/30/92

4. TITLE AND SUBTITLE

Atlas of Formability
Hastelloy C-22

5. FUNDING NUMBERS

C-N00140-88-C-RC21

6. AUTHOR(S)

Prabir Chaudhury
Dan Zhao

7. PERFORMING ORGANIZATION NAME(S) AND ADDRESS(ES)

National Center for Excellence in Metalworking
Technology (NCEMT)
1450 Scalp Avenue
Johnstown, PA 15904

8. PERFORMING ORGANIZATION REPORT NUMBER

9. SPONSORING/MONITORING AGENCY NAME(S) AND ADDRESS(ES)

Naval Industrial Resources Support Activity
Building 75-2, Naval Base
Philadelphia, PA 19112-5078

10. SPONSORING/MONITORING AGENCY REPORT NUMBER

11. SUPPLEMENTARY NOTES

12a. DISTRIBUTION/AVAILABILITY STATEMENT

12b. DISTRIBUTION CODE

13. ABSTRACT (Maximum 200 words)

In this investigation, flow behavior of Hastelloy C-22 was studied by conducting compression tests at various temperatures and strain rates. Constitutive relations were determined from the flow behavior, and a dynamic material modeling for this alloy was performed. Thus, the optimum processing condition in terms of temperature and strain rate was determined. Microstructural changes during high temperature deformation were also characterized to aid process design engineers to select processing conditions in terms of resulting microstructure.

14. SUBJECT TERMS

Hastelloy C-22, Deformation Processing, High Temperature Deformation, Processing Map, Metalworking

15. NUMBER OF PAGES

65

16. PRICE CODE

17. SECURITY CLASSIFICATION OF REPORT	18. SECURITY CLASSIFICATION OF THIS PAGE	19. SECURITY CLASSIFICATION OF ABSTRACT	20. LIMITATION OF ABSTRACT
Unclassified	Unclassified	Unclassified	

DISCLAIMER NOTICE
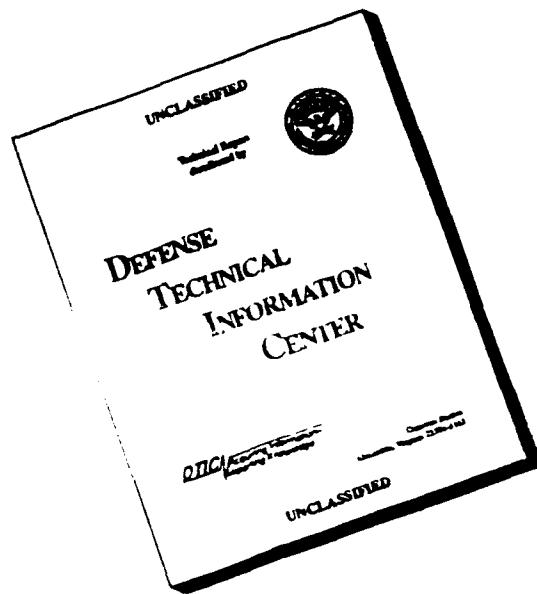
THIS DOCUMENT IS BEST QUALITY AVAILABLE. THE COPY FURNISHED TO DTIC CONTAINED A SIGNIFICANT NUMBER OF PAGES WHICH DO NOT REPRODUCE LEGIBLY.

ATLAS OF FORMABILITY

HASTELLOY C-22

by

Prabir K. Chaudhury and Dan Zhao

National Center for Excellence in Metalworking Technology
1450 Scalp Avenue
Johnstown, PA 15904

for

September 30, 1992

TABLE OF CONTENTS

DTIC QUALITY INSPECTED 3

LIST OF TABLE

Hastelloy C-22

Introduction

Hastelloys are noted for their relatively high strength in corrosive environments at high temperatures. The C-22 is a versatile nickel-Chromium-molydenum-tungsten alloy with improved resistance to both uniform and localized corrosion. The C-22 also exhibits superior weldability and is used as overalloy filler wire and weld overlay consumables to improve resistance to corrosion. In this investigation, flow behavior of Hastelloy C-22 was studied by conducting compression tests at various temperatures and strain rates. Constitutive relations were determined from the flow behavior, and a dynamic material modeling for this alloy was performed. Thus, the optimum processing condition in terms of temperature and strain rate was determined. Microstructural changes during high temperature deformation were also characterized to aid process design engineers to select processing conditions in terms of resulting microstructure.

Experimental Procedure

The material used in this investigation was Hastelloy C-22 wrought bars in annealed condition. The composition (in wt%) is as follows

C	Co	Cr	Fe	Mn	Mo	Ni	P	S	V	W	Si
.003	2.02	21.0	4.2	.26	13.3	BAL	.008	.002	.13	3.1	.027

The typical microstructure of the as-received material consists of a uniform equiaxed grain with an average size of 96 μm (ASTM 3.5) as shown in Figure 1. Cylindrical compression test specimens with a diameter of 12.7 mm and a height of 15.9 mm were machined from the bars. Isothermal compression testing was conducted on an MTS testing machine under vacuum environment. The test matrix was as follows:

Temperature, C (F): 950 (1742), 1000 (1832), 1050 (1922), 1100 (2012), 1125 (2057), 1150 (2102), and 1200 (2192);

Strain rate, s^{-1}: 0.001, 0.01, 0.05, 0.1, 0.5, 1, 5 and 20.

Load and stroke data from the tests were acquired by a computer and later converted to true stress-true strain curves. Immediately after the compression test, the specimens were quenched with forced helium gas in order to retain the deformed microstructure. Longitudinal and transverse sections of the specimens were examined using optical microscope. The photomicrographs presented were taken from the center of the longitudinal section of the specimens.

Results

Table 1 is a list of the figures, test conditions and the observed microstructures. The true stress-true strain flow curves with the corresponding deformed microstructure are shown in Figure 2 to Figure 57. True stress versus strain rate was plotted in log-log scale in Figure 58 at a true strain of 0.55. The slope of the plot gives the strain rate sensitivity m, which is not constant over the range of strain rate tested. Log stress vs. 1/T at the same true strain is shown in Figure 69. A processing map at this strain was developed for the Hastelloy C-22 alloy and is shown in Figure 60. The optimum processing conditions from the map can be obtained by selecting the temperature and strain rate combination which provides the maximum efficiency in the stable region. This condition is approximately 1050 C and 0.001 s^{-1} for this material.

Table 1. List of figures, testing conditions and microstructural observations for Hastelloy C-22

Figure No	Temperature C(F)	Strain Rate S-1	Microstructure Optical Microscopy	Page No
1	As received	-	Uniform large equiaxed grains of ~96μm (ASTM 3.50) with some twinning	4
2	950(1742)	0.001	Elongated deformed grains with ~10% necklacing. Slip bands and twinning are present.	5
3	950(1742)	0.01		6
4	950(1742)	0.05	Elongated deformed grains with ~2% necklacing, slip bands and twinning are present.(twins showed a large degree of deformation)	7
5	950(1742)	0.10	Same as above, but the twin boundaries show the presence of necklacing.	8
6	950(1742)	0.50		9
7	950(1742)	1.0	Elongated grains with ~10 % of small recrystallized grains. Some necklacing at the twin boundaries and slip bands are present.	10
8	950(1742)	5.0		11
9	950(1742)	20.0	Elongated grains with ~15 % of small recrystallized grains (~9 μm). Some necklacing around the elongated grains and twin boundaries. Slip bands are also present.	12
10	1000(1832)	0.001	Elongated grains with ~20 % of recrystallized grains (~25 μm). Some recrystallization at the twin boundaries. Slip bands are not present.	13
11	1000(1832)	0.01	Elongated grains with ~15 % of recrystallized grains. Some of the new grains show twinning. Slip bands and extensive necklacing at twin and grain boundaries are present.	14
12	1000(1832)	0.05	Same as above, but a higher proportion of recrystallization is observed.	15
13	1000(1832)	0.10		16
14	1000(1832)	0.50		17
15	1000(1832)	1.0	Elongated grains and ~32% of equiaxed recrystallized grains. Slip bands are present and recrystallization at twin boundaries is also observed.	18
16	1000(1832)	5.0		19
17	1000(1832)	20.0	Some elongated grains and a large proportion of equiaxed recrystallized grains, some slip bands are also present.	20
18	1050(1922)	0.001	~98% of equiaxed recrystallized grains, some of them show the presence of twinning.	21
19	1050(1922)	0.01		22
20	1050(1922)	0.05	Some elongated deformed grains and equiaxed recrystallized grains (~80%) with the presence of twinning.	23
21	1050(1922)	0.1		24
22	1050(1922)	0.5		25

2

23	1050(1922)	1	Some elongated deformed grains and equiaxed recrystallized grains (~75%) with the presence of twinning.	26
24	1050(1922)	5		27
25	1050(1922)	20	Some elongated deformed grains and equiaxed recrystallized grains (~65%) with the presence of twinning.	28
26	1100(2012)	0.001	Equiaxed recrystallized grains with an average grain size of 25 μm. Grain size is not uniform.	29
27	1100(2012)	0.01	Same as above	30
28	1100(2012)	0.05		31
29	1100(2012)	0.1	Equiaxed recrystallized grains with a duplex size, average grain size 18 μm. A small proportion of large equiaxed grains (2-5%) with a size of ~70μm. Twinning of the new grains is present.	32
30	1100(2012)	0.5		33
31	1100(2012)	1	Equiaxed recrystallized grains with a duplex size. A small proportion of large equiaxed grains (~2%). Twinning of the new grains is present.	34
32	1100(2012)	5		35
33	1100(2012)	20	Equiaxed recrystallized grains with a relatively uniform grain size (~19 μm).	36
34	1125(2057)	0.001	Large equiaxed recrystallized grains, some show twinning	37
35	1125(2057)	0.01		38
36	1125(2057)	0.05	Same as above, but smaller grain size.	39
37	1125(2057)	0.1		40
38	1125(2057)	0.5		41
39	1125(2057)	1	Same as above	42
40	1125(2057)	5		43
41	1125(2057)	20	Same as above	44
42	1150(2102)	0.001	Large equiaxed recrystallized grains with a size range. The larger grains show the presence of a substructure. Twinning is also evident.	45
43	1150(2102)	0.01	Large equiaxed recrystallized grains with extensive twinning. There is also a small proportion of larger grains.	46
44	1150(2102)	0.05		47
45	1150(2102)	0.1	Equiaxed recrystallized grains showing some twinning.	48
46	1150(2102)	0.5		49
47	1150(2102)	1	Same as above	50
48	1150(2102)	5		51
49	1150(2102)	20	Same as above, but smaller grain size	52
50	1200(2192)	0.001	Equiaxed recrystallized grains with an average grain size of 80 μm. Twinning is also present.	53
51	1200(2192)	0.01		54
52	1200(2192)	0.05	Large equiaxed recrystallized grains with an average grain size of 43 μm. Twinning is also present in the microstructure.	55

3

| 53	1200(2192)	0.1	Same as above, but with smaller grain size.	56
54	1200(2192)	0.5	Same as above	57
55	1200(2192)	1		58
56	1200(2192)	5		59
57	1200(2192)	20	Same as above	60
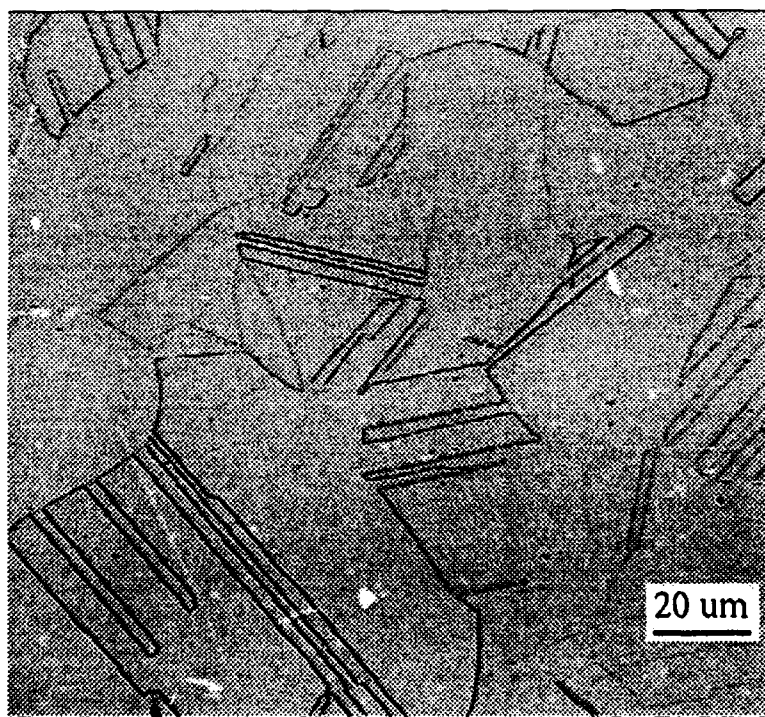
Figure 1. As-received microstructure of Hastelloy C-22.
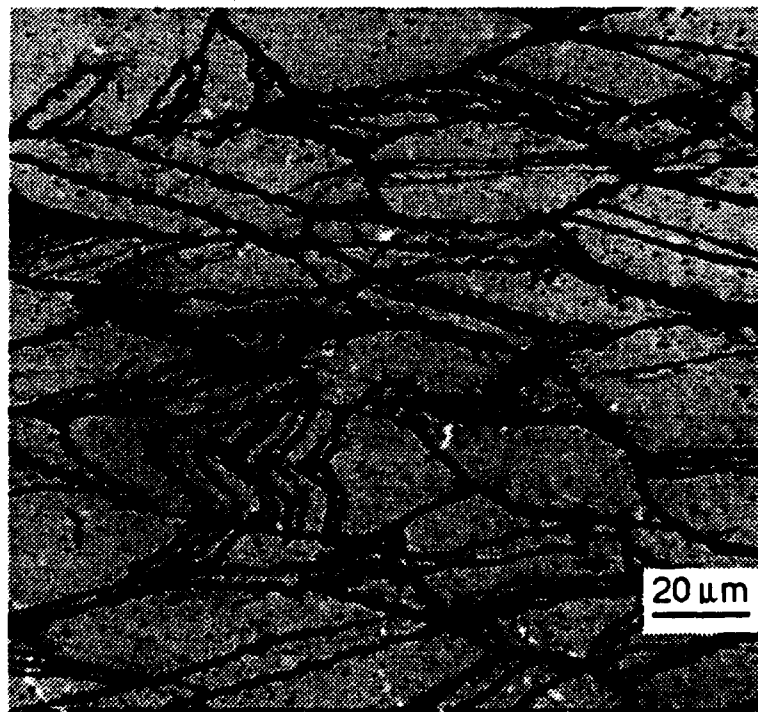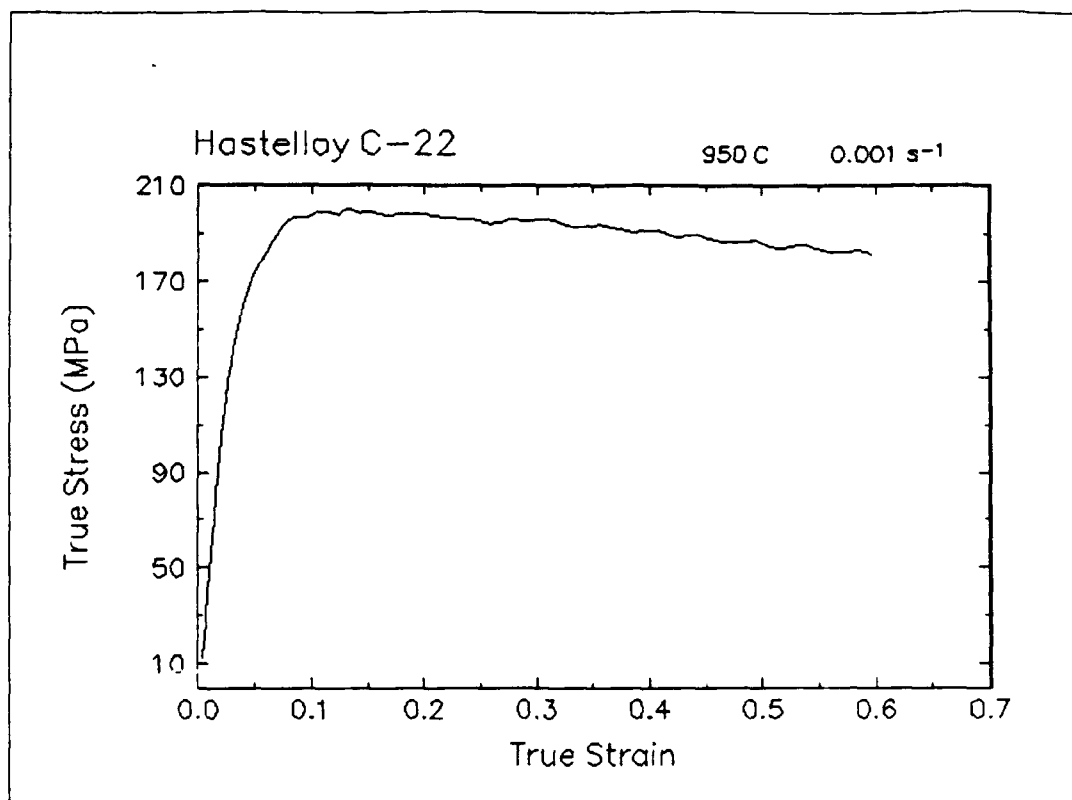
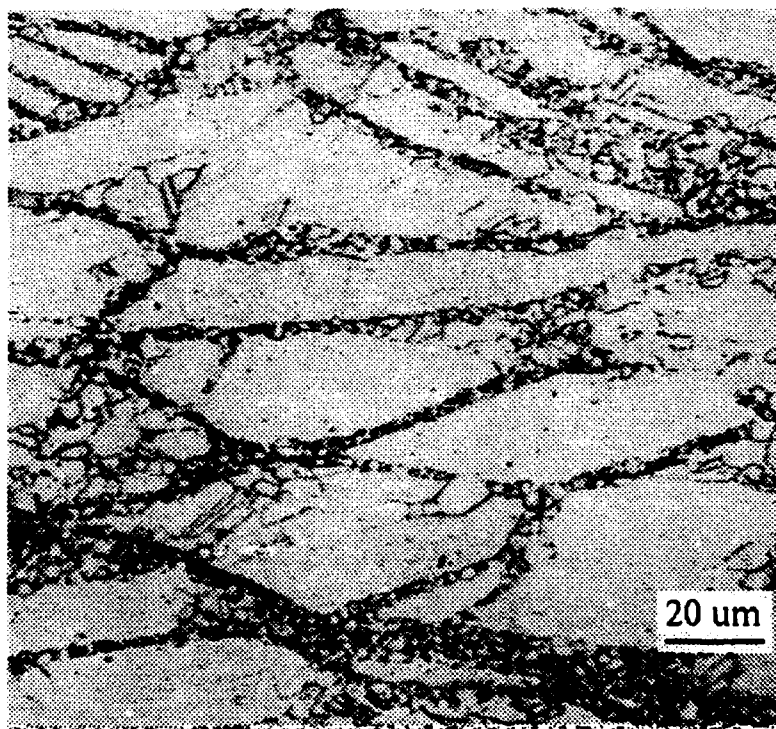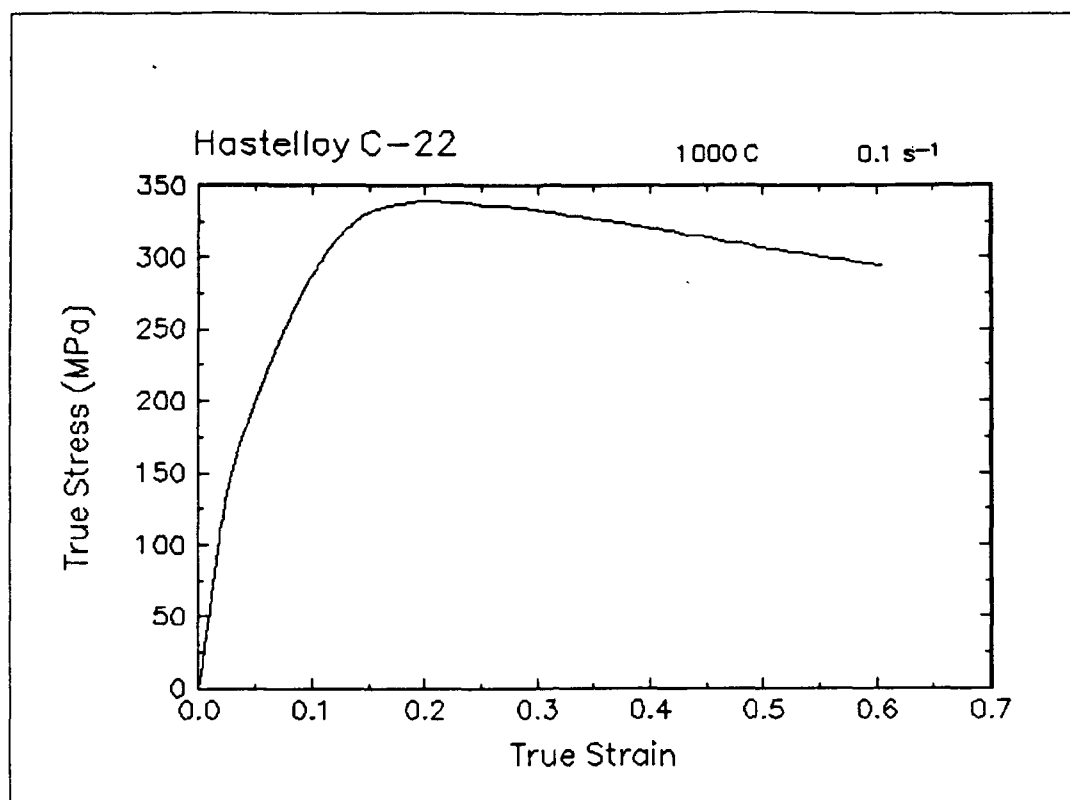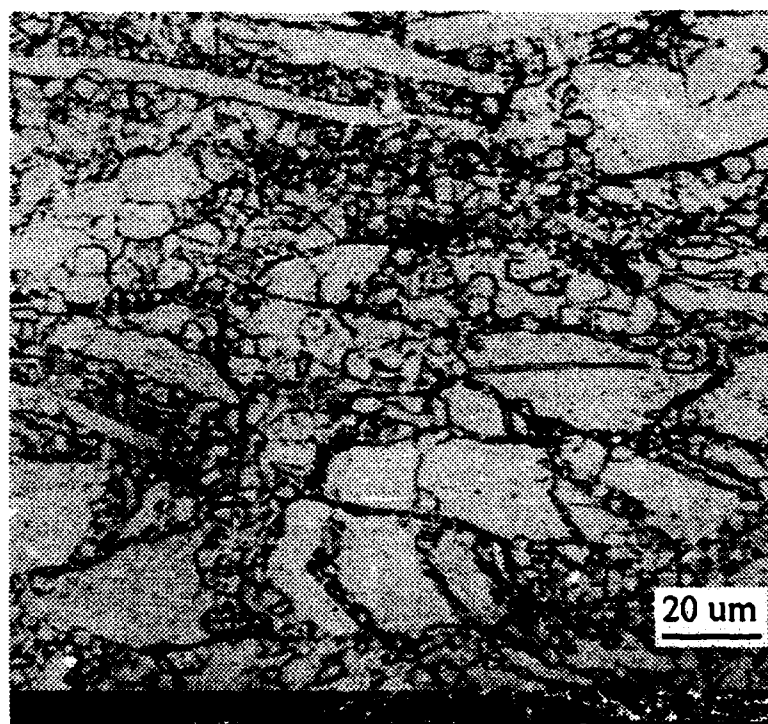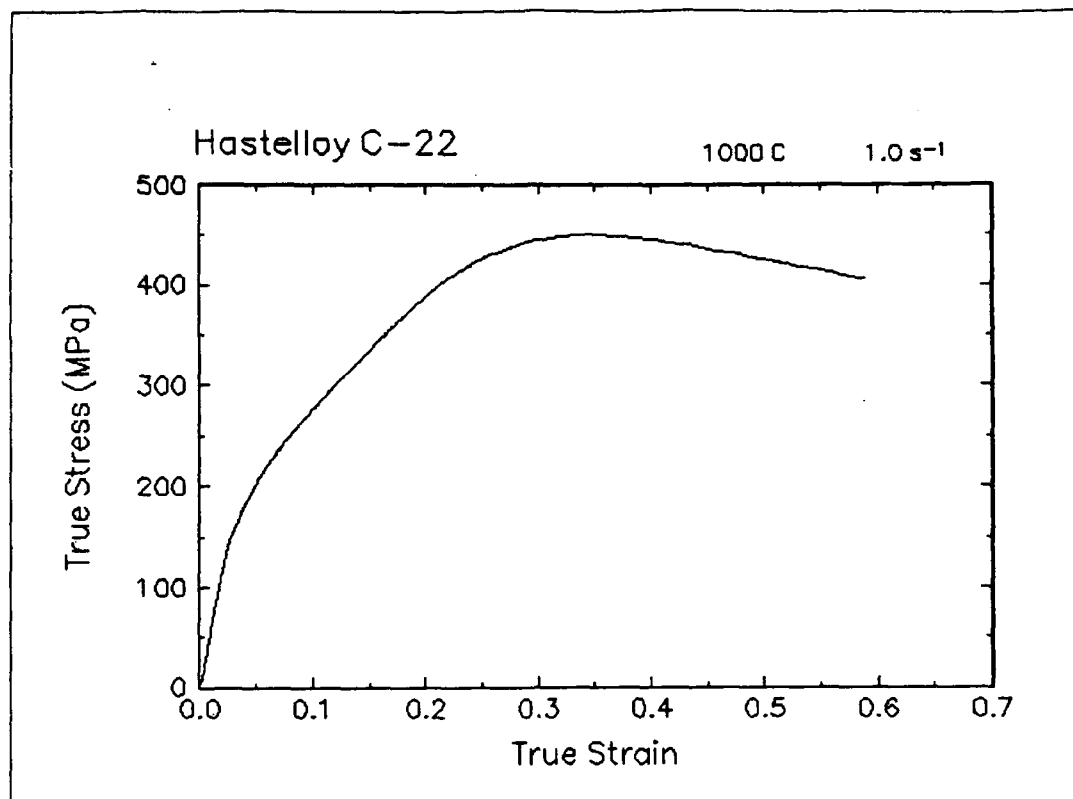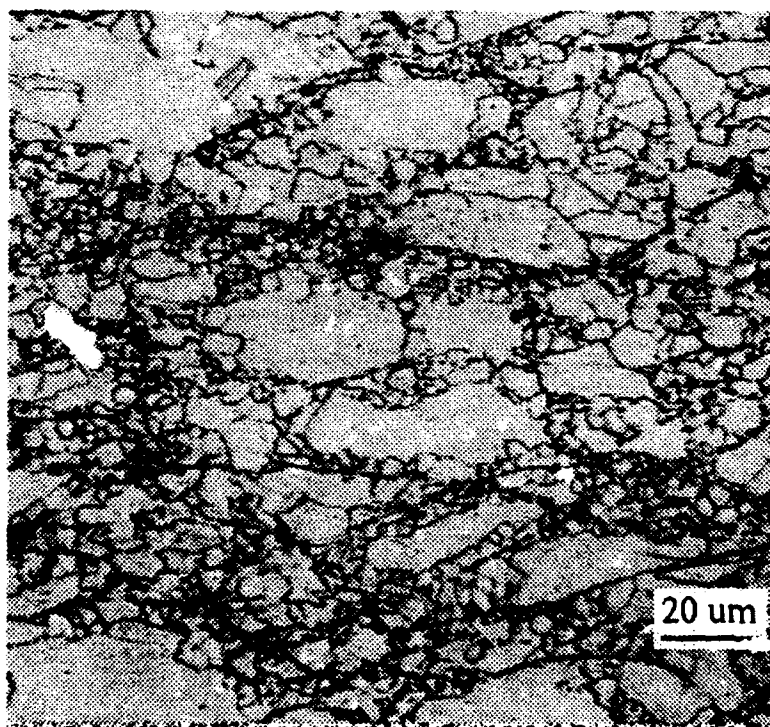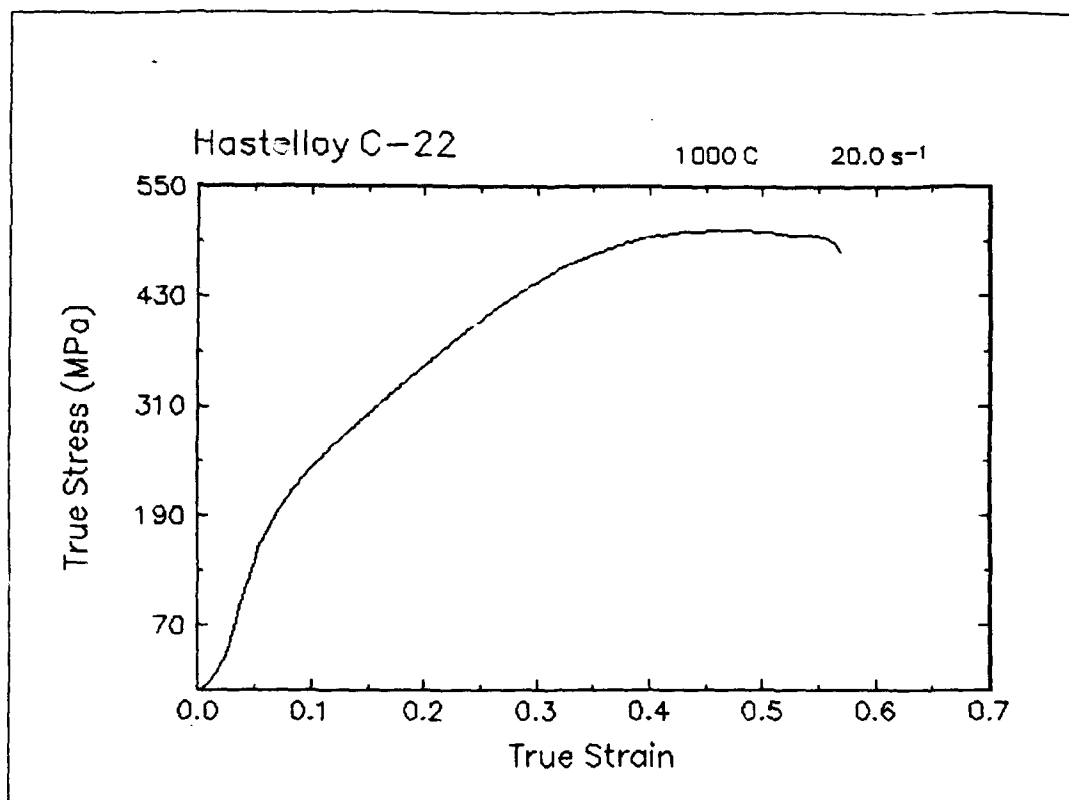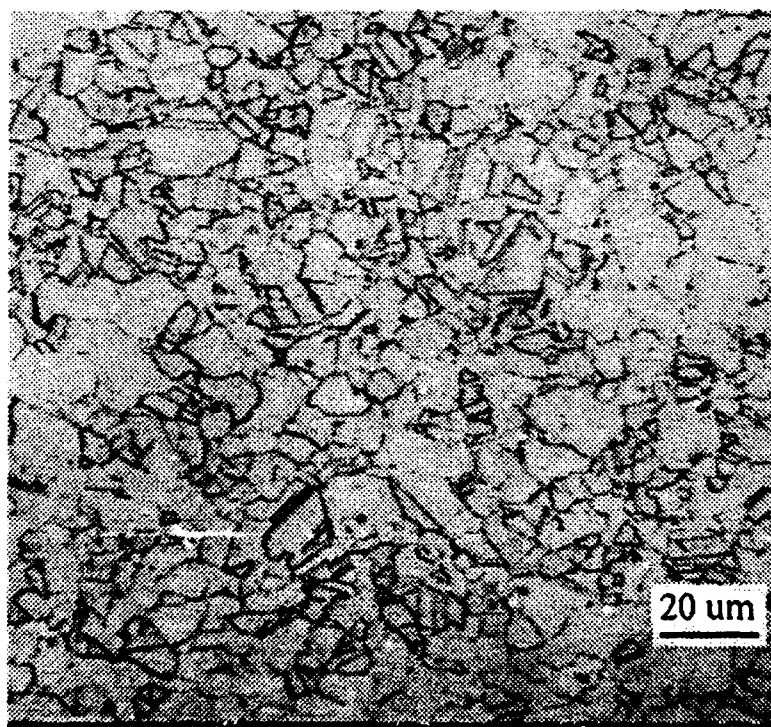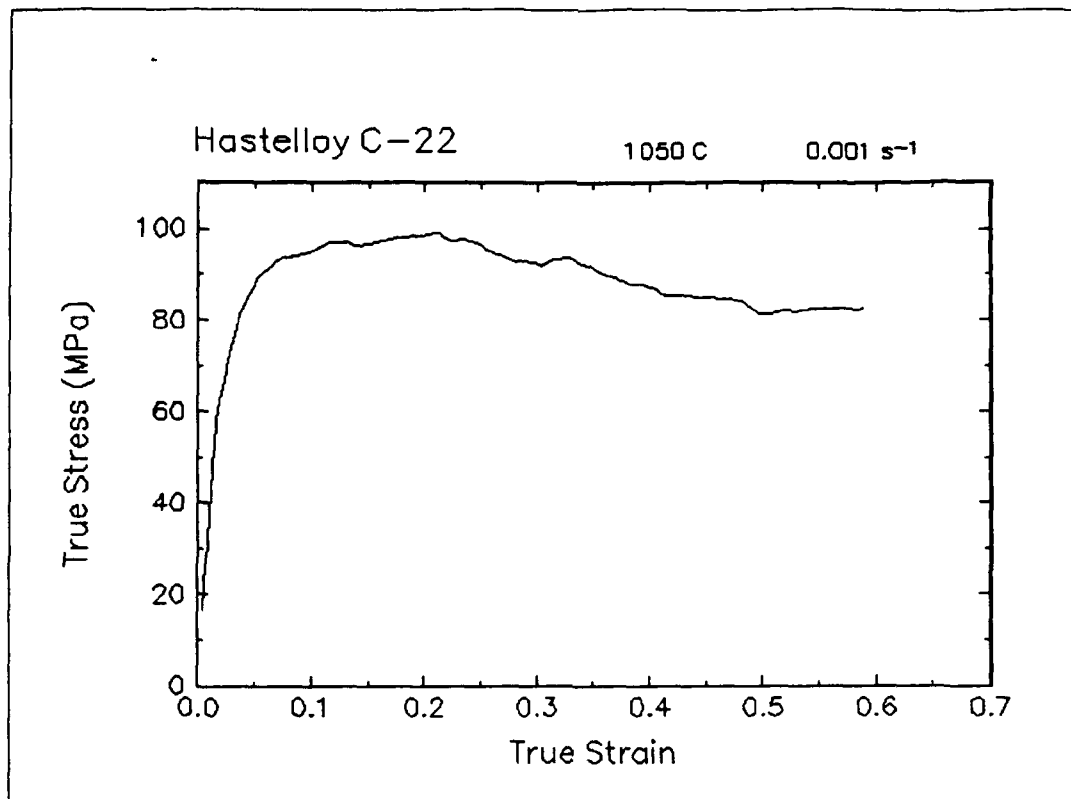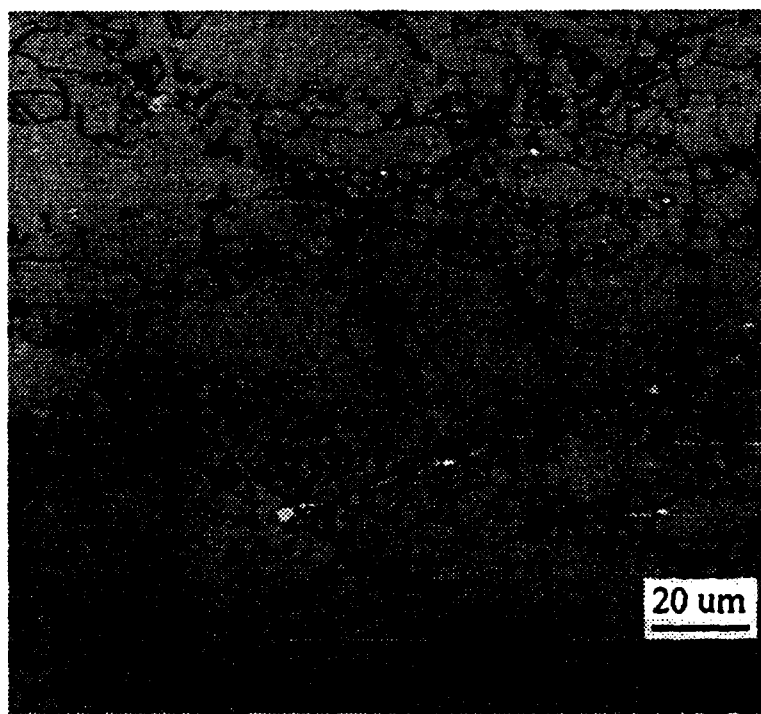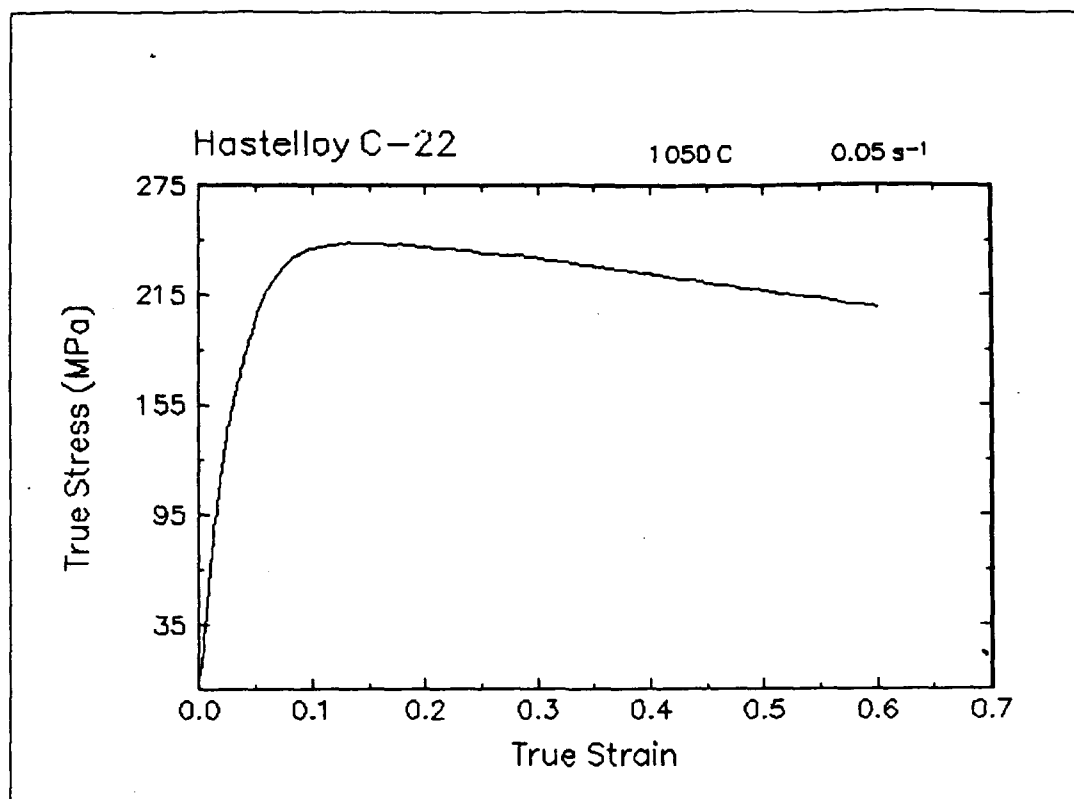Figure 2. True stress-true strain curve and an optical micrograph from the center of the compressed sample cut through the compression axis, 950 C and 0.001 s^{-1}.
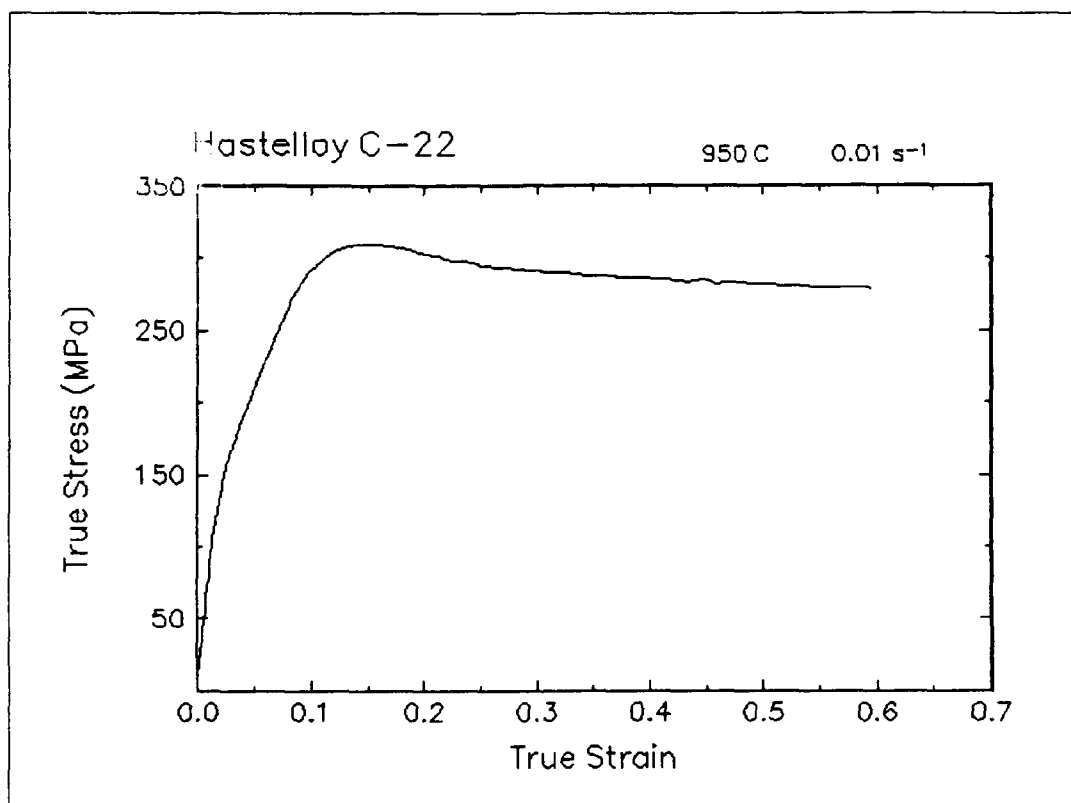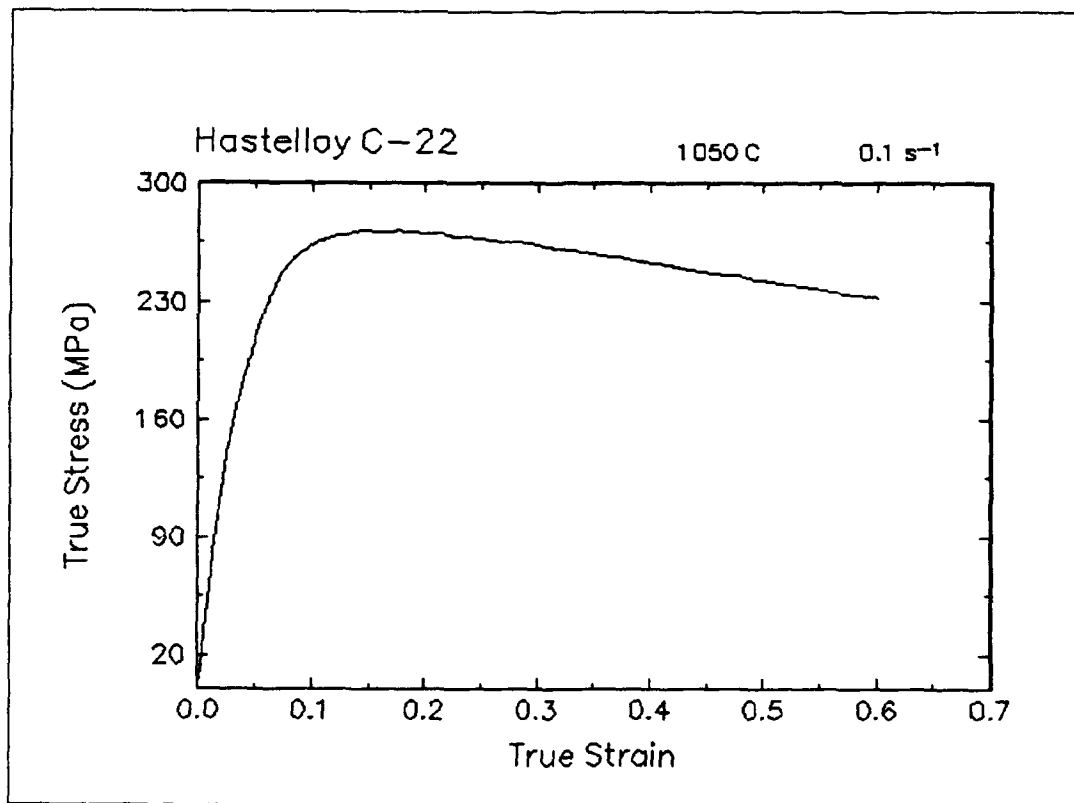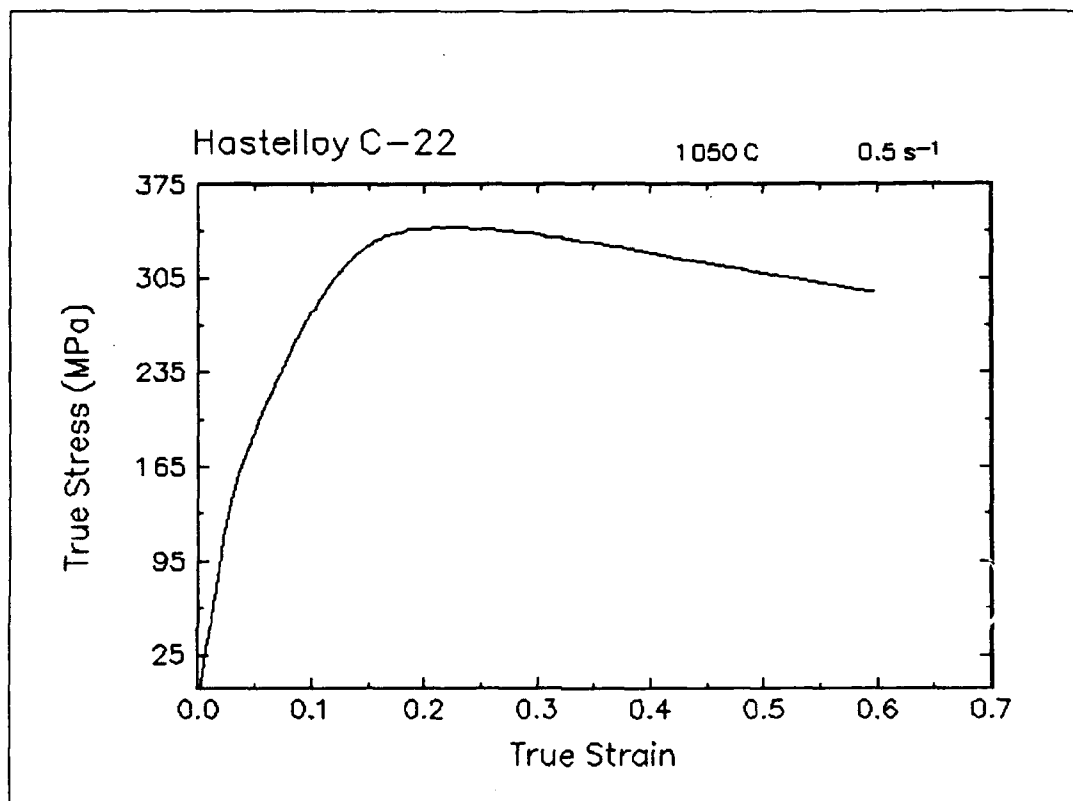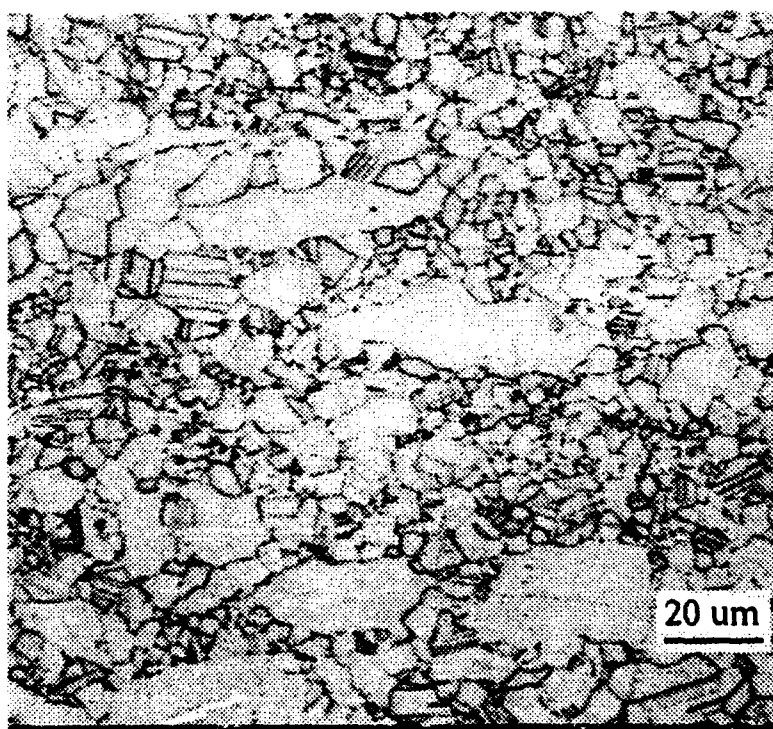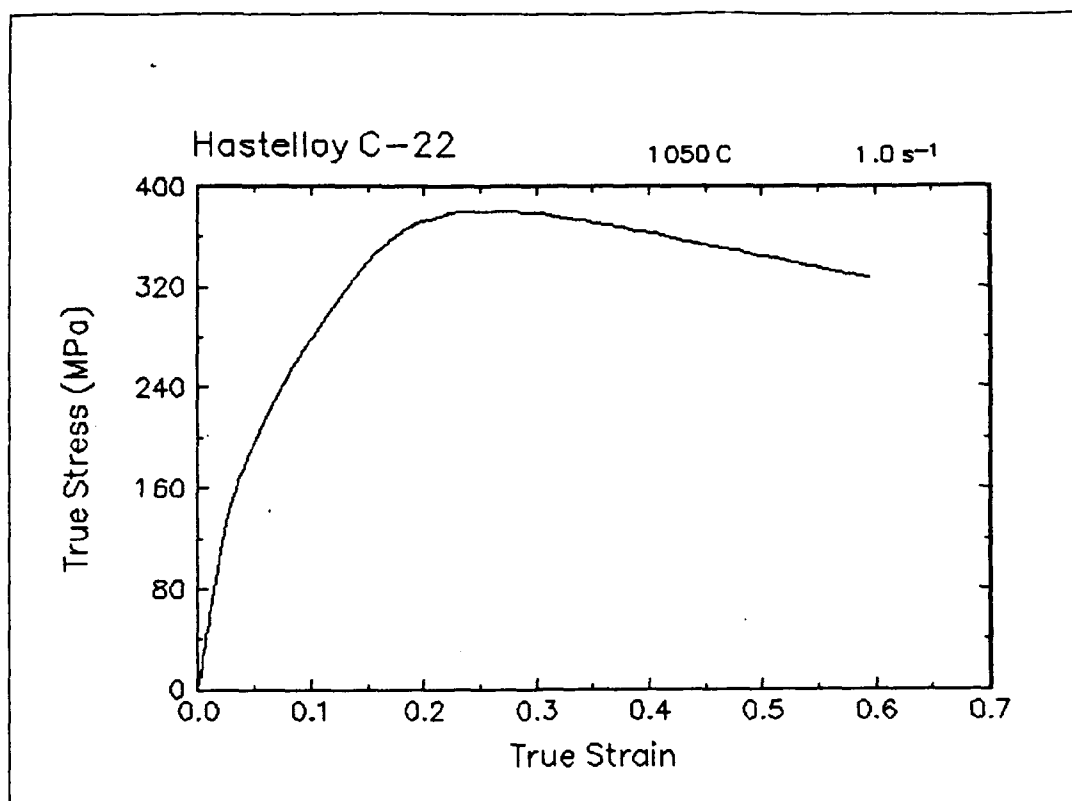
Figure 3. True stress-true strain curve, 950 C and 0.01 s^{-1}.
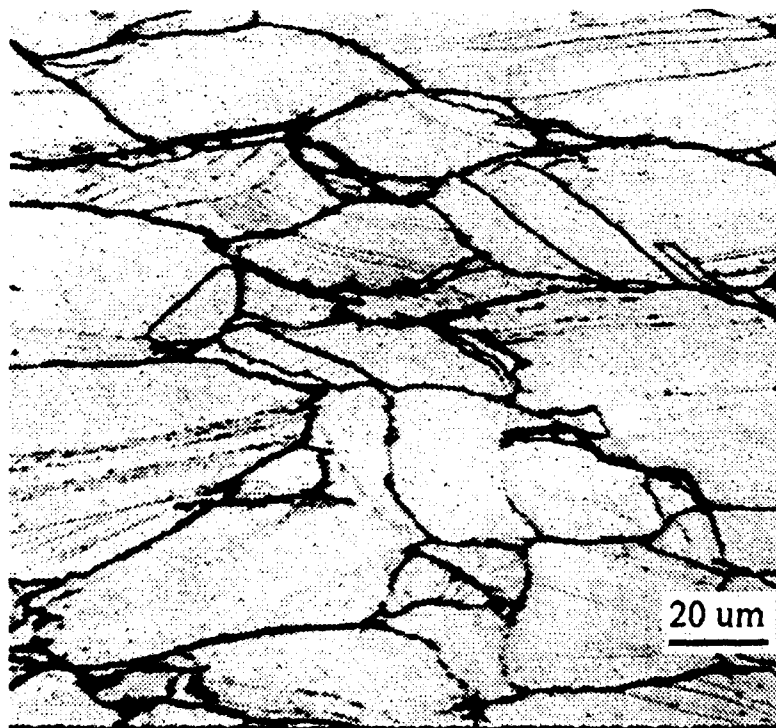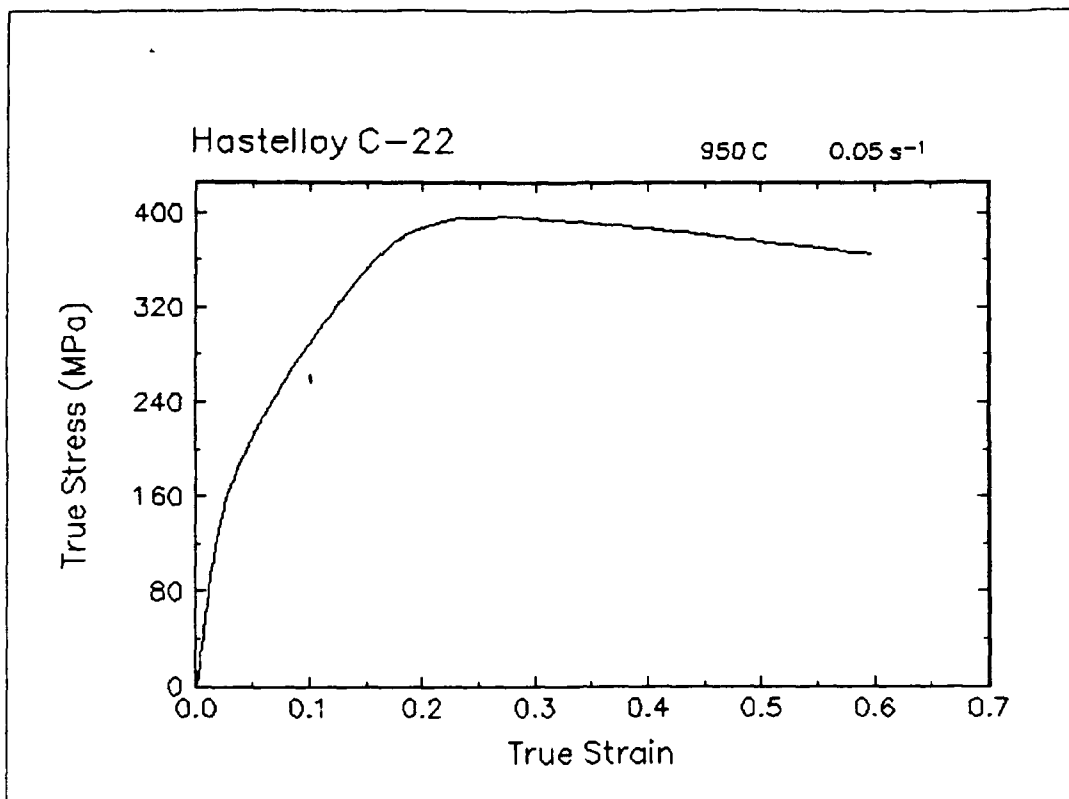
Figure 4. True stress-true strain curve and an optical micrograph from the center of the compressed sample cut through the compression axis, 950 C and 0.05 s^{-1}.
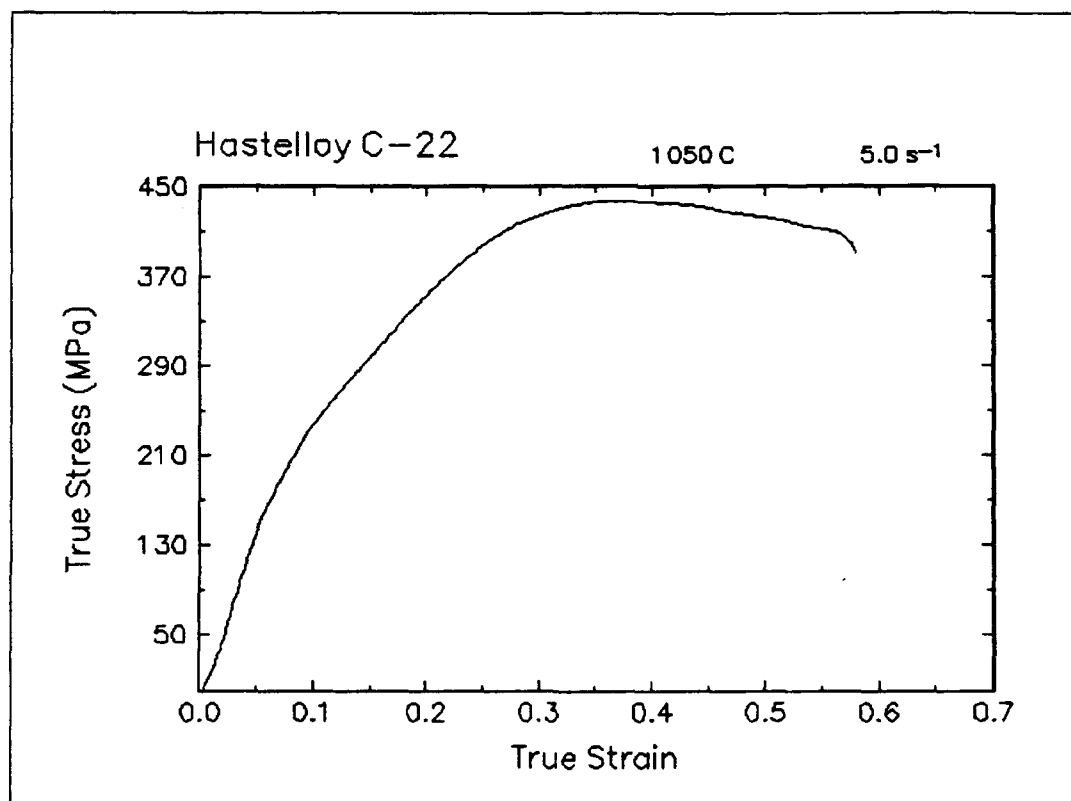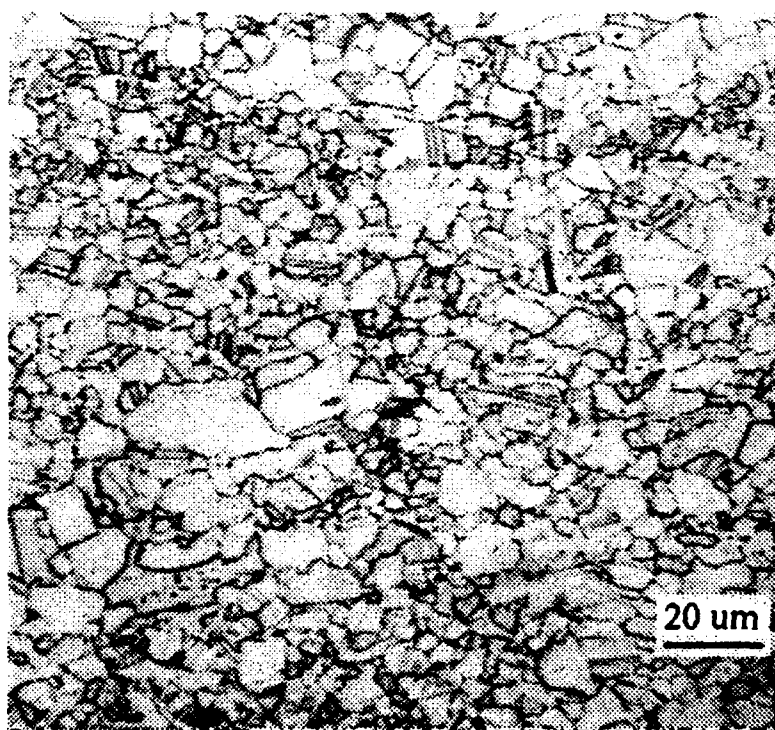
7
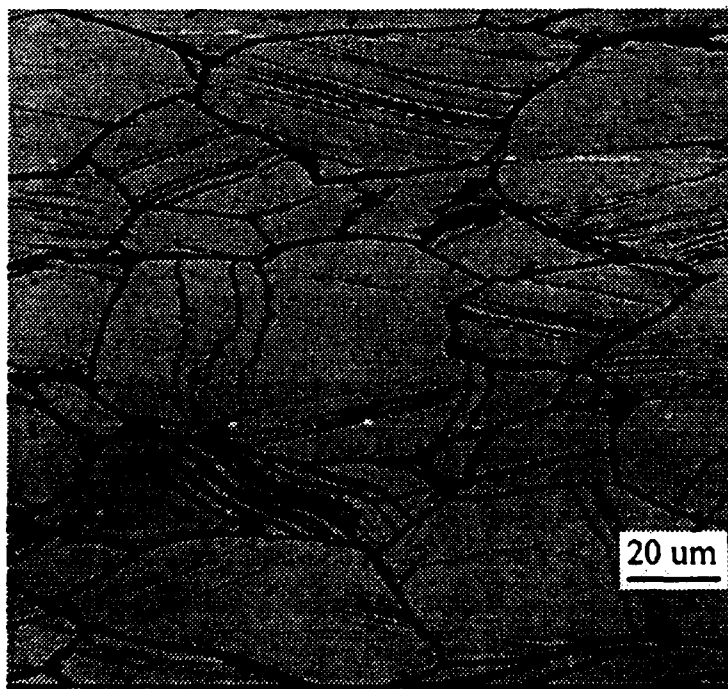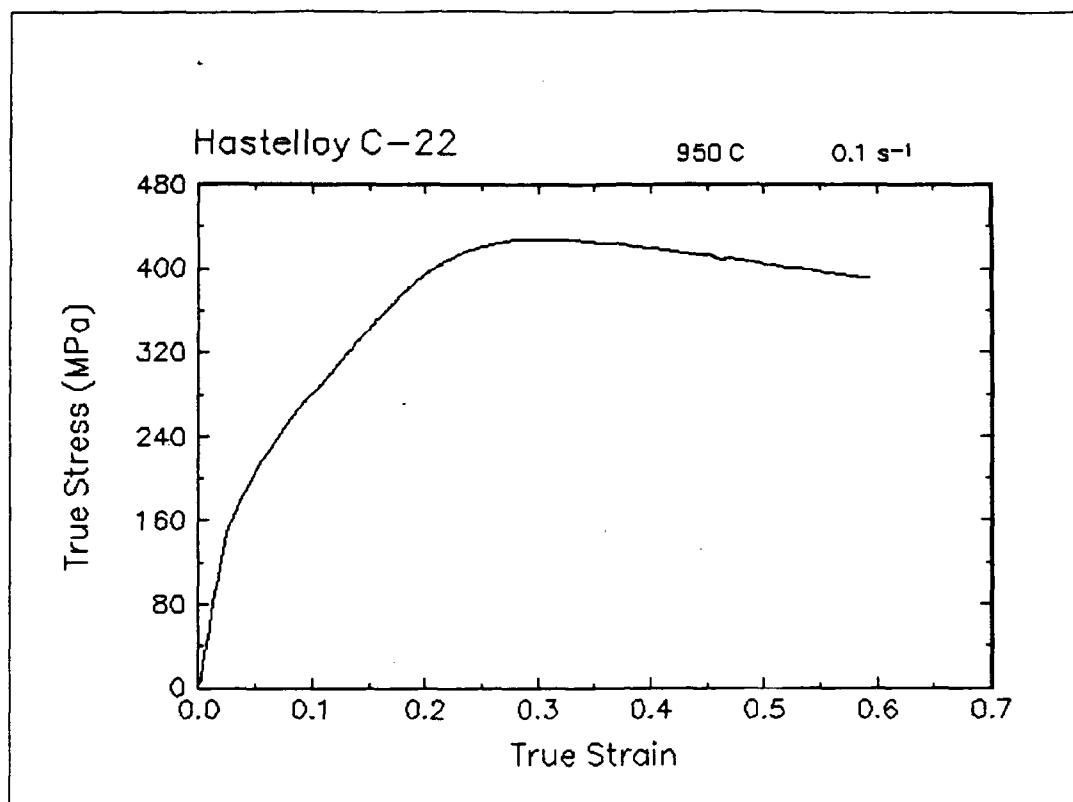
Figure 5. True stress-true strain curve and an optical micrograph from the center of the compressed sample cut through the compression axis, 950 C and 0.1 s^{-1}.
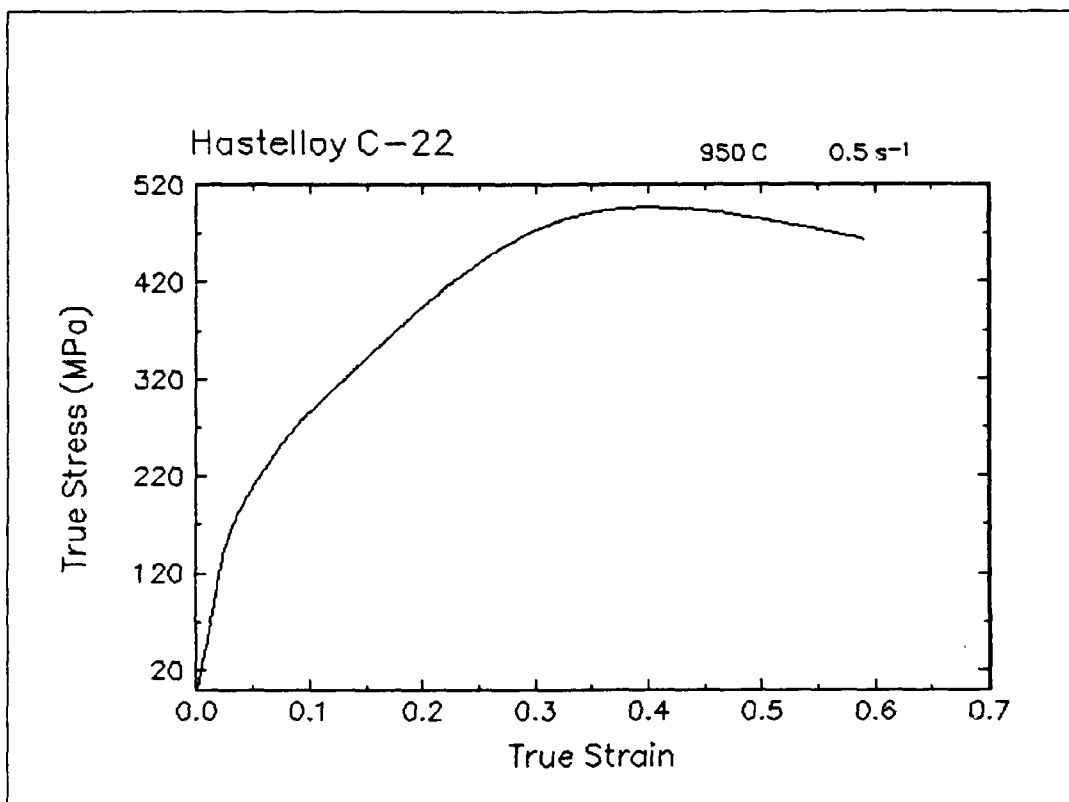
Figure 6. True stress-true strain curve, 950 C and 0.5 s^{-1}.
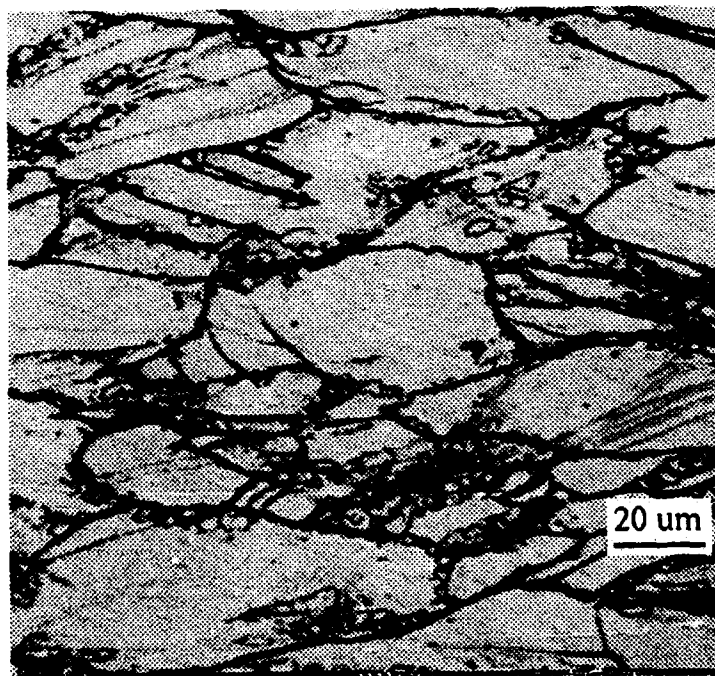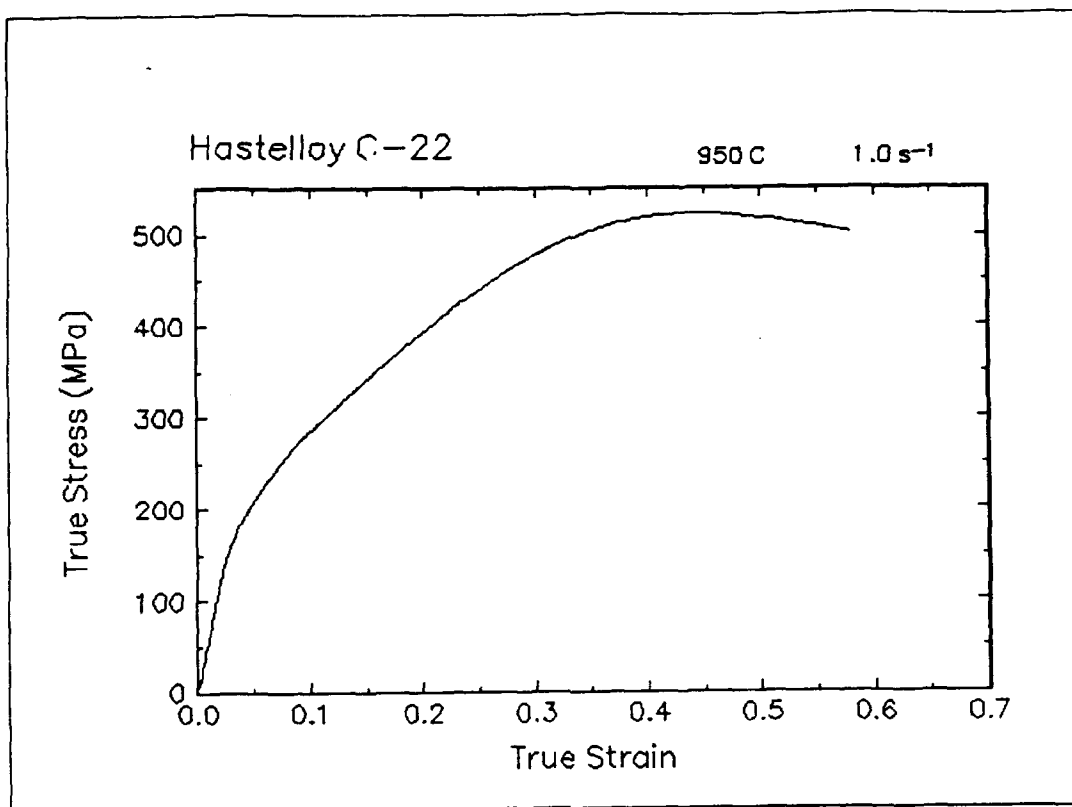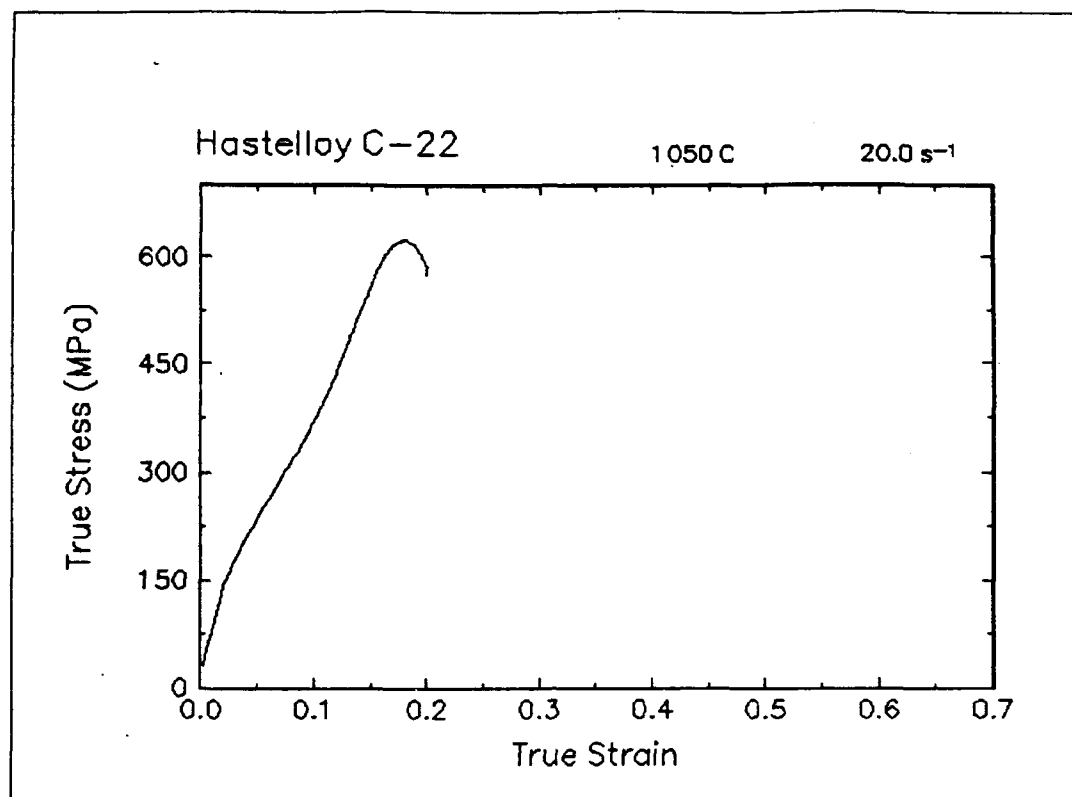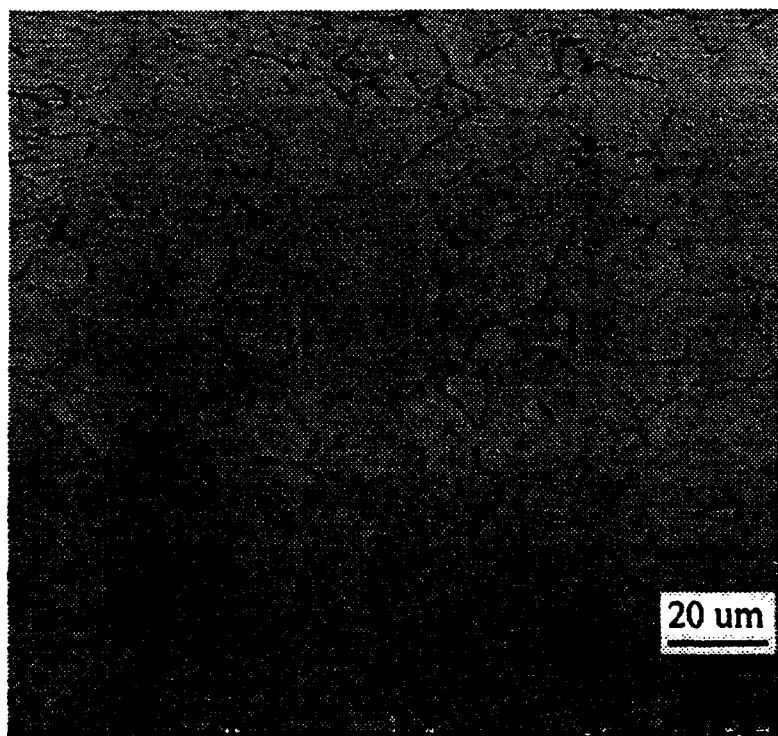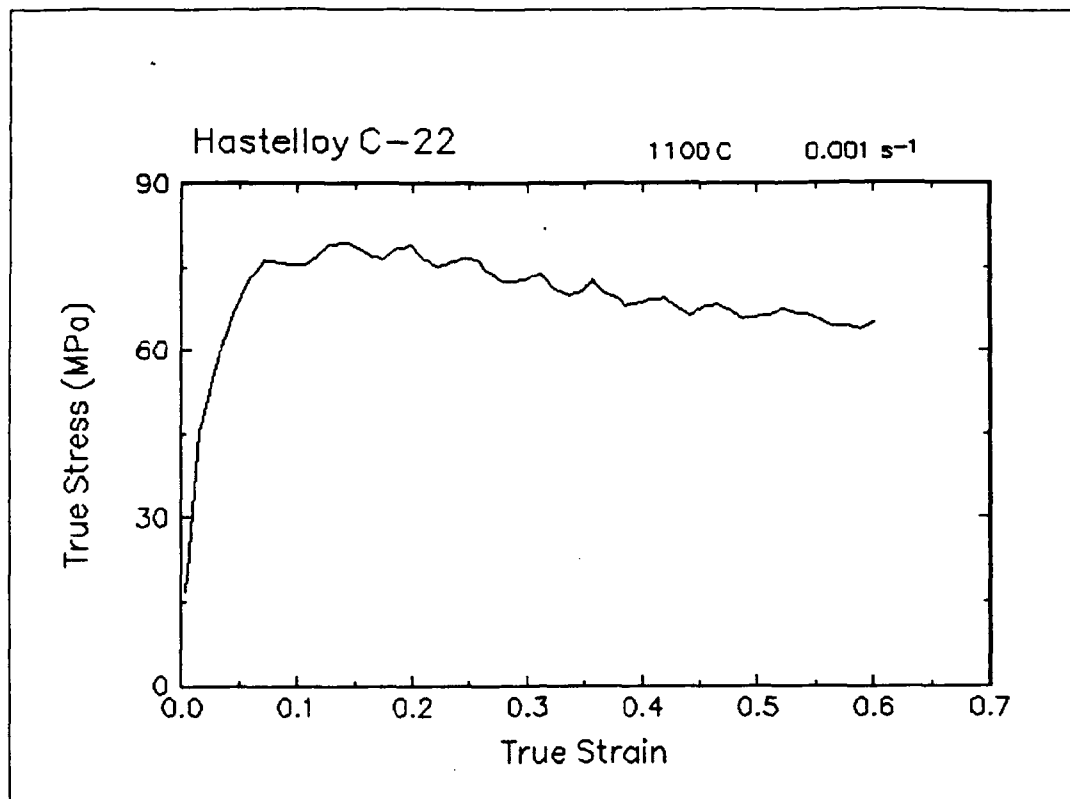
Figure 7. True stress-true strain curve and an optical micrograph from the center of the compressed sample cut through the compression axis, 950 C and 1 s^{-1}.
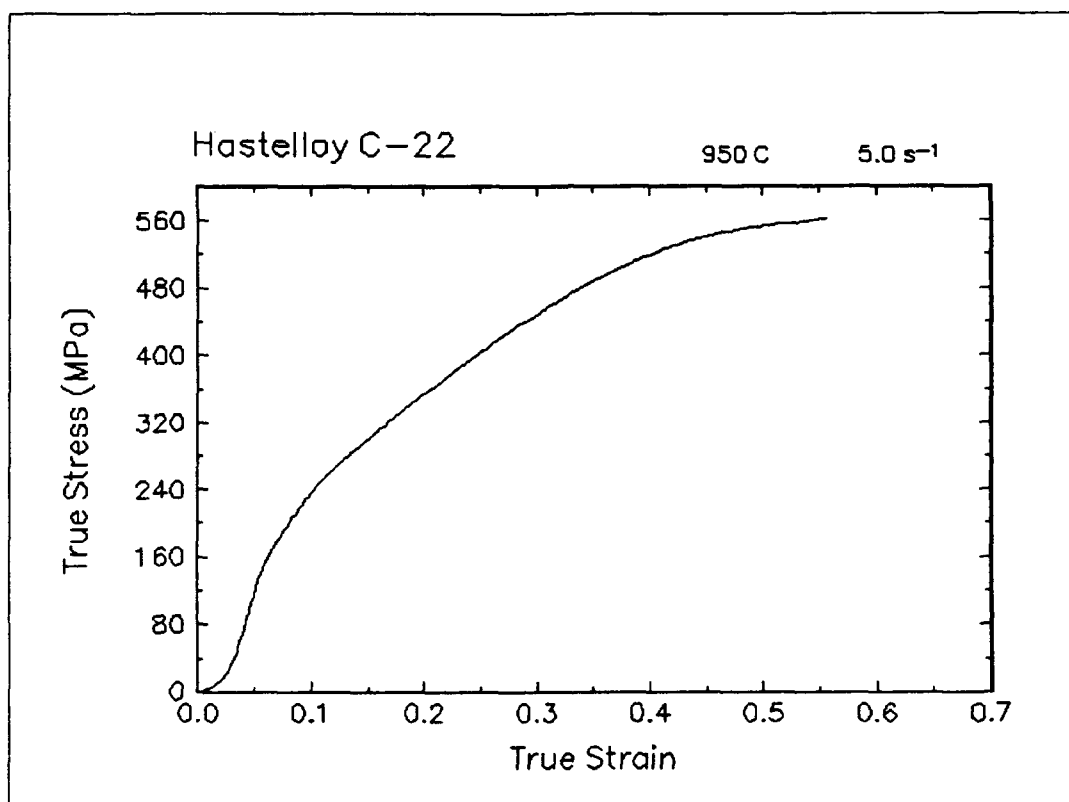
Figure 8. True stress-true strain curve, 950 C and 5 s^{-1}.
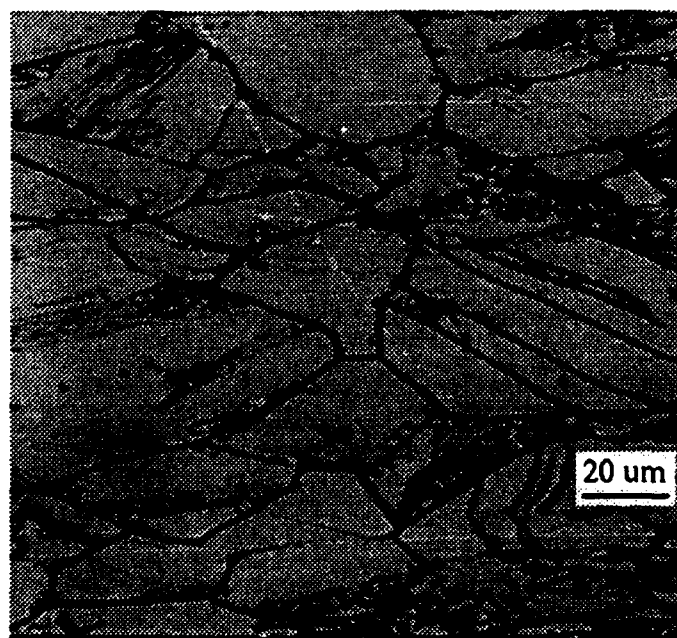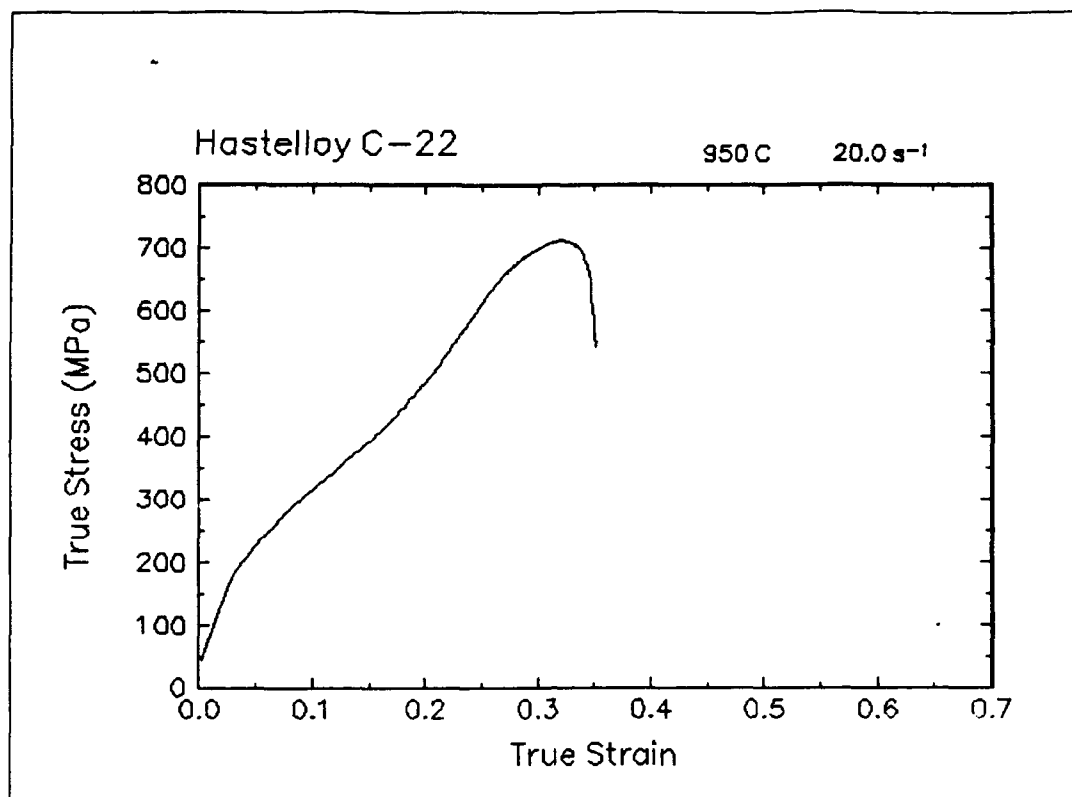
Figure 9. True stress-true strain curve and an optical micrograph from the center of the compressed sample cut through the compression axis, 950 C and 20 s^{-1}.
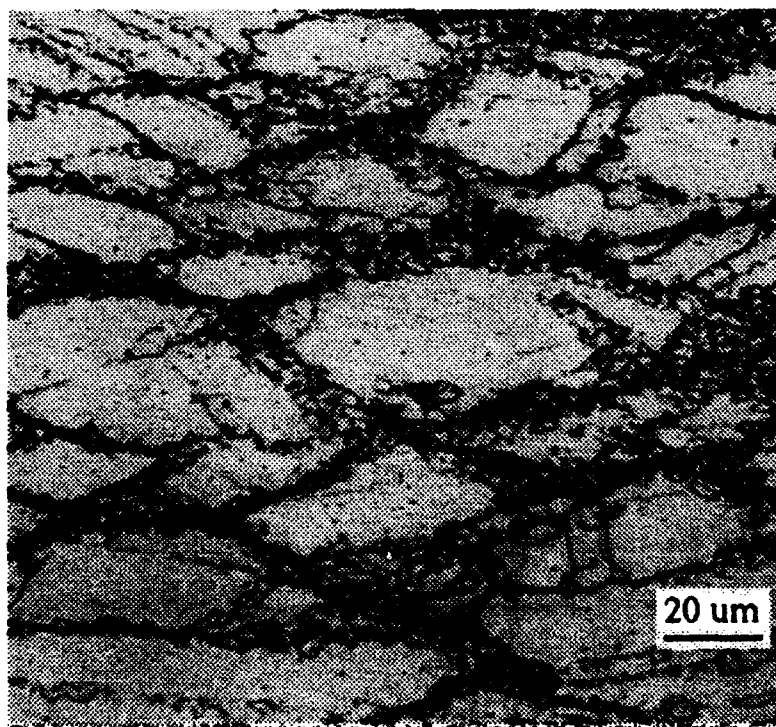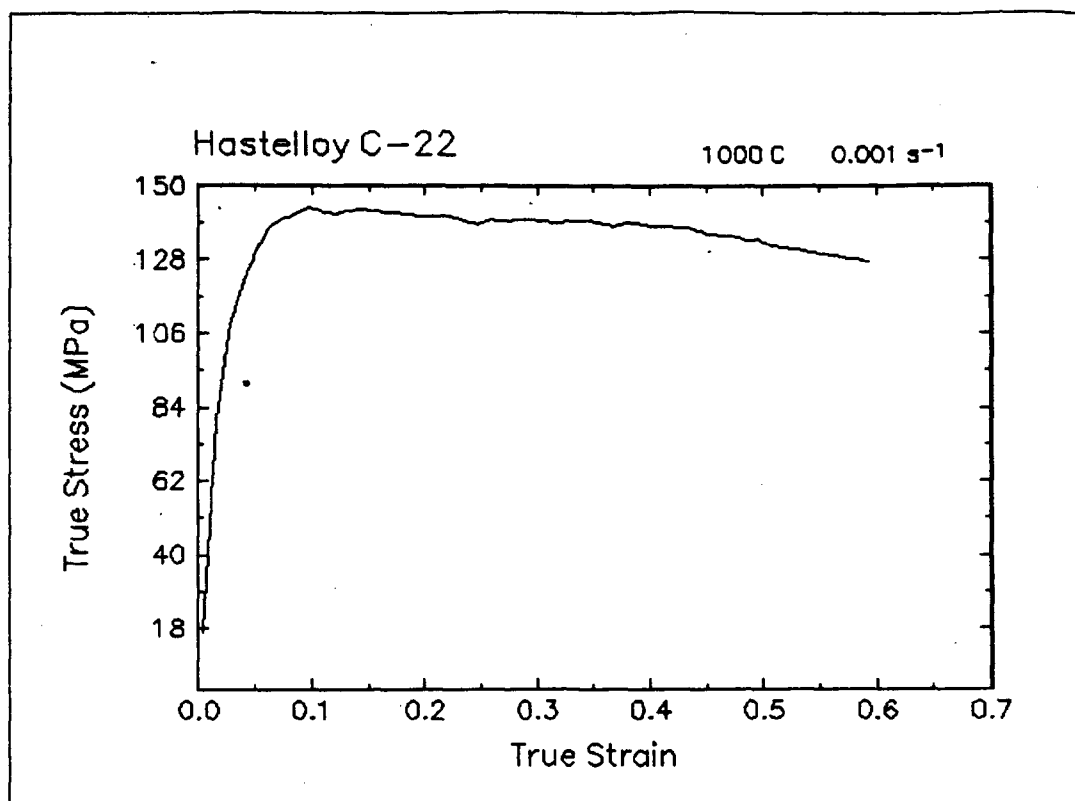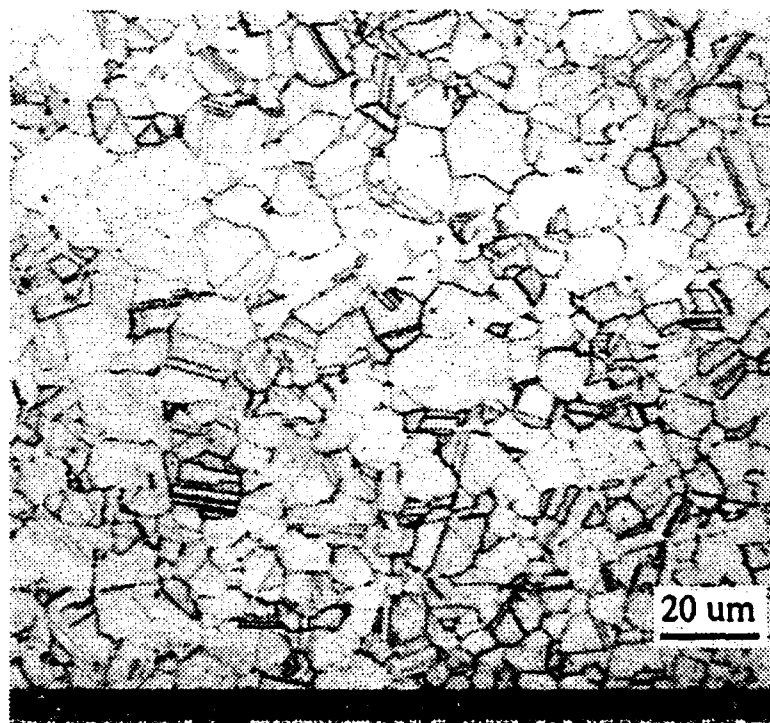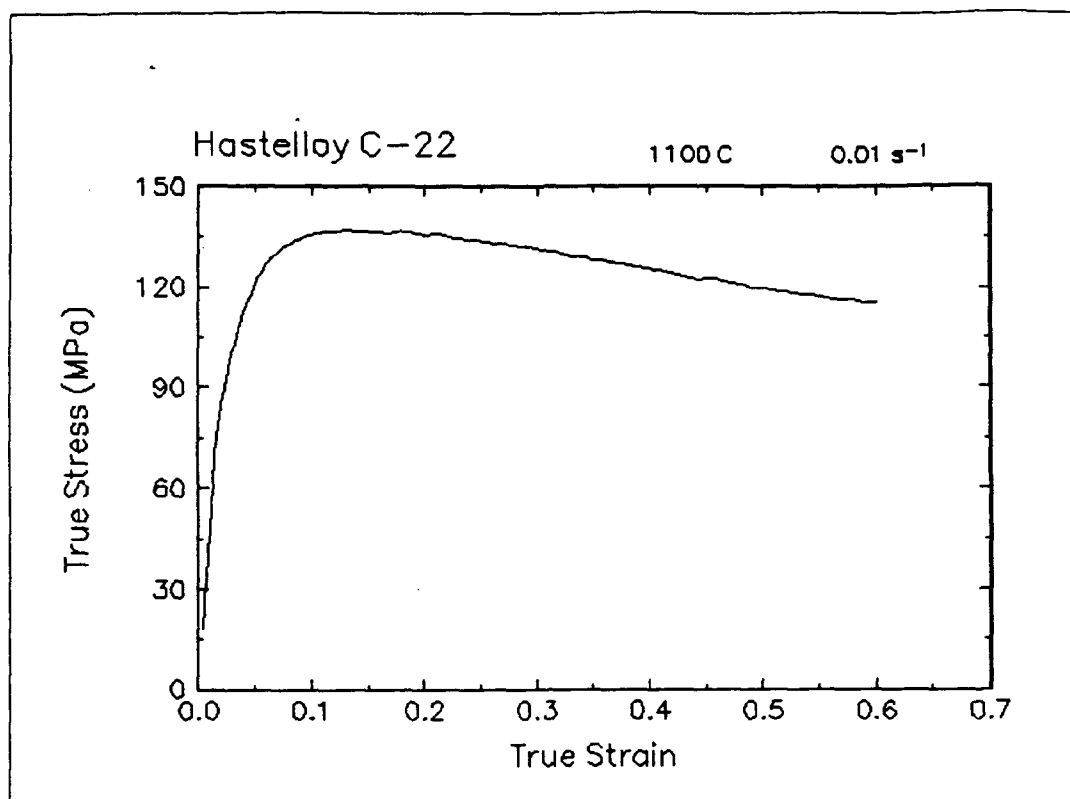
Figure 10. True stress-true strain curve and an optical micrograph from the center of the compressed sample cut through the compression axis, 1000 C and 0.001 s⁻¹.
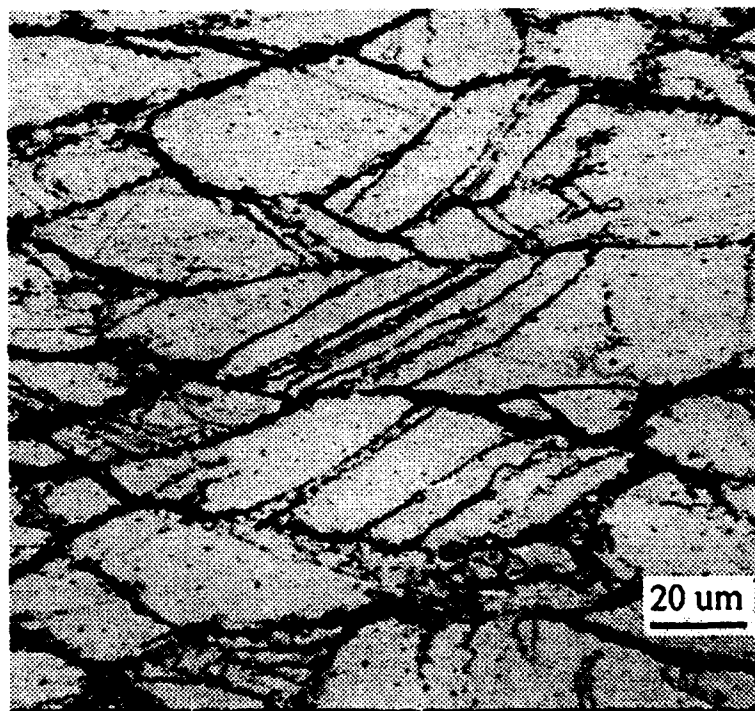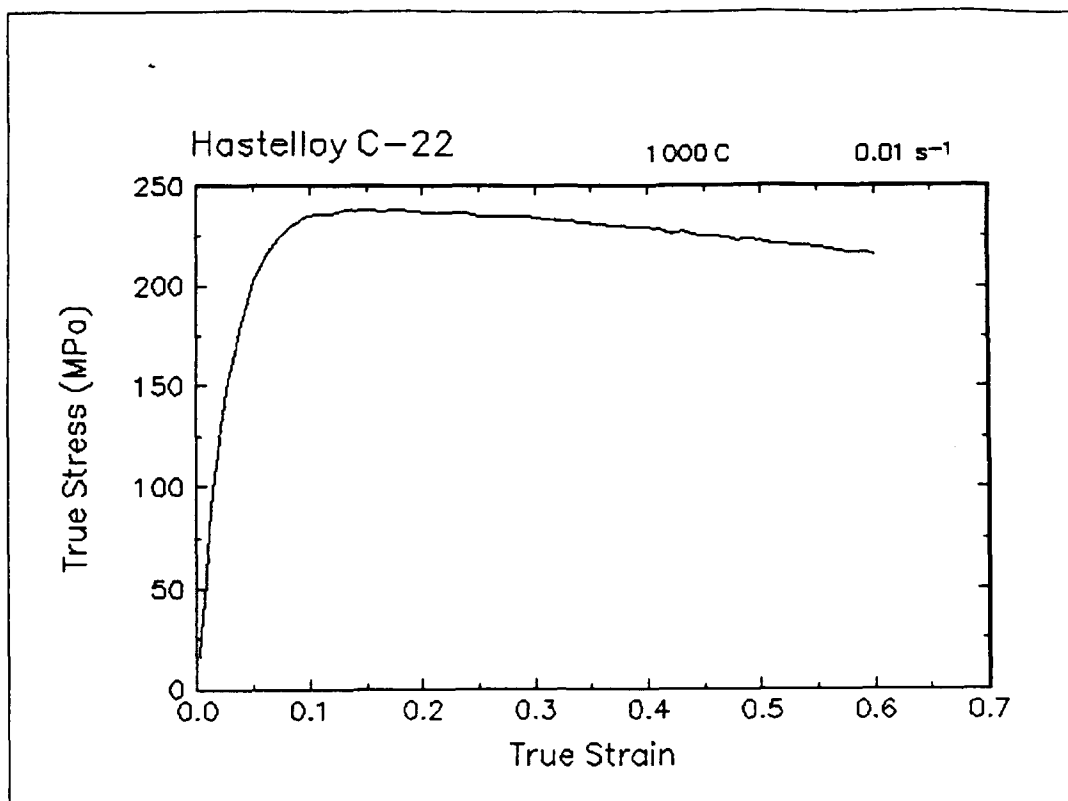
Figure 11. True stress-true strain curve and an optical micrograph from the center of the compressed sample cut through the compression axis, 1000 C and 0.01 s^{-1}.
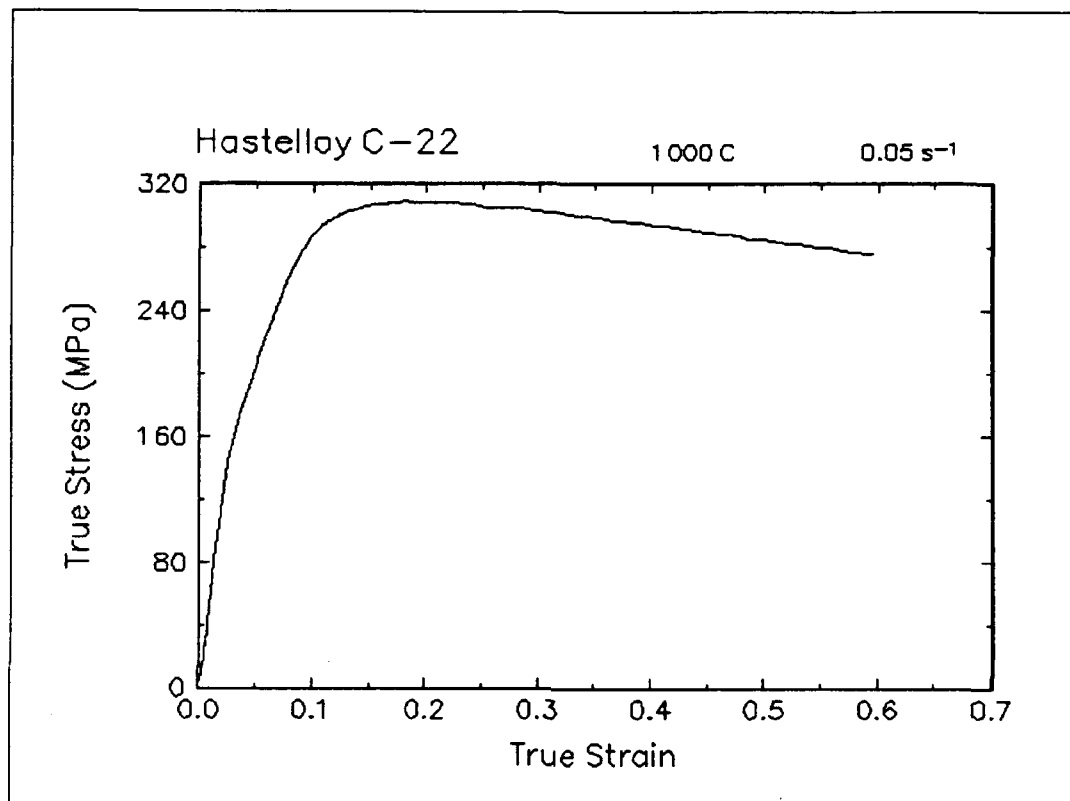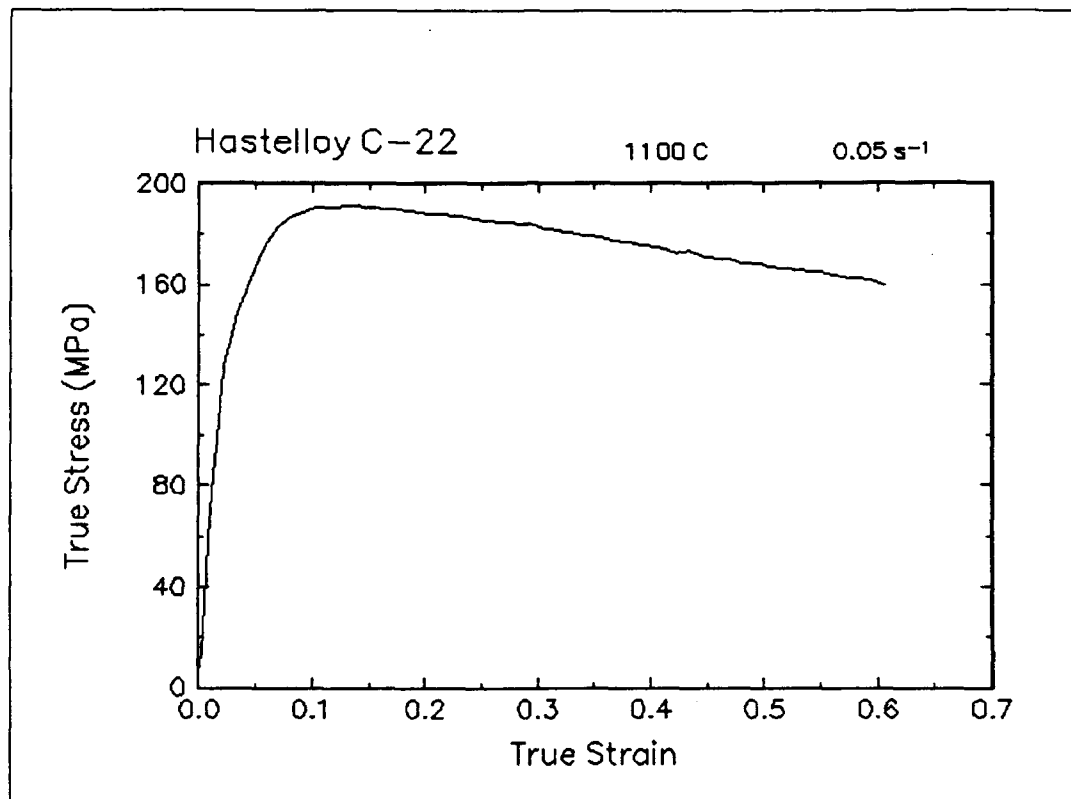
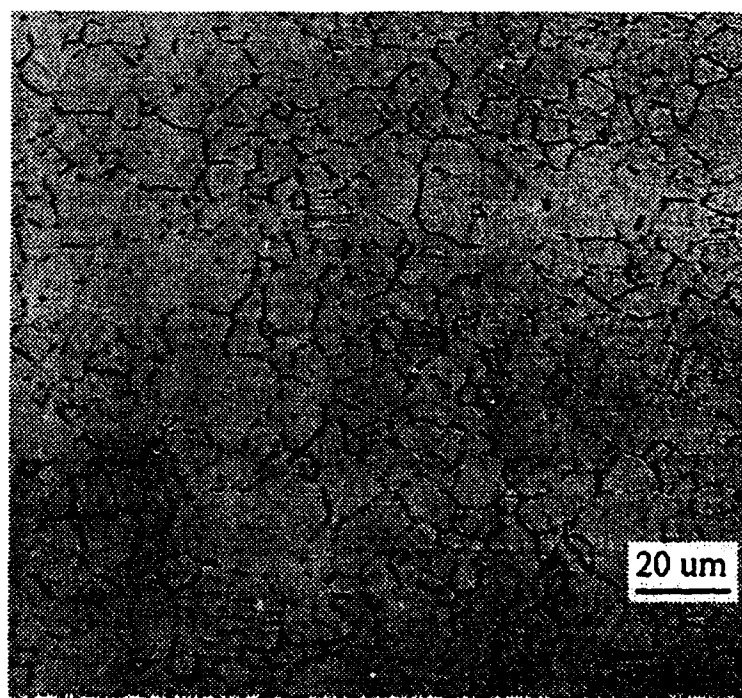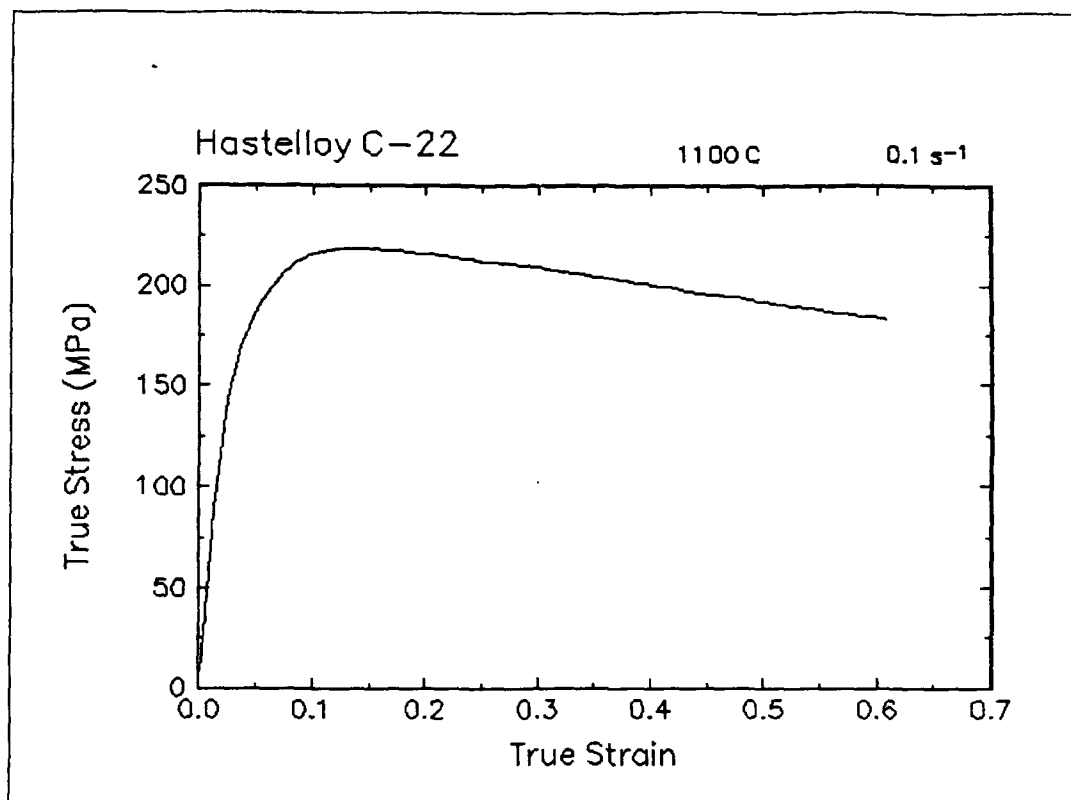Figure 12. True stress-true strain curve, 1000 C and 0.05 s^{-1}.

Figure 13. True stress-true strain curve and an optical micrograph from the center of the compressed sample cut through the compression axis, 1000 C and 0.1 s^{-1}.
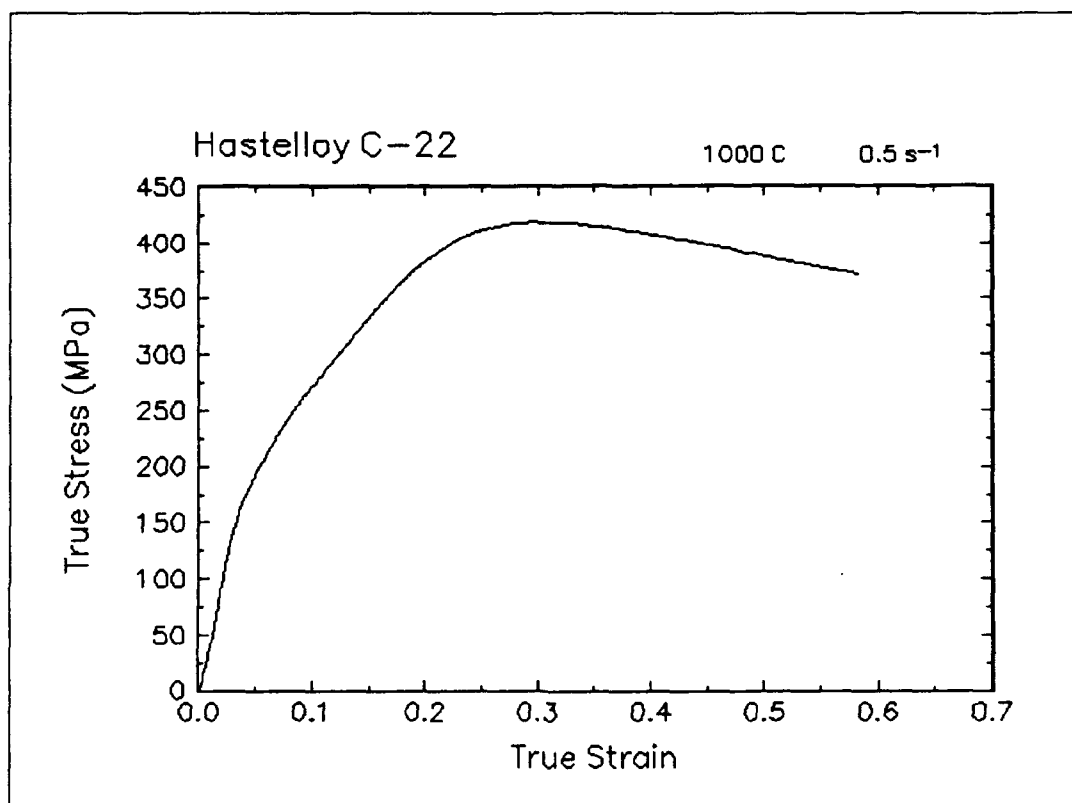
Figure 14. True stress-true strain curve, 1000 C and 0.5 s^{-1}.

Figure 15. True stress-true strain curve and an optical micrograph from the center of the compressed sample cut through the compression axis, 1000 C and 1 s^{-1}.
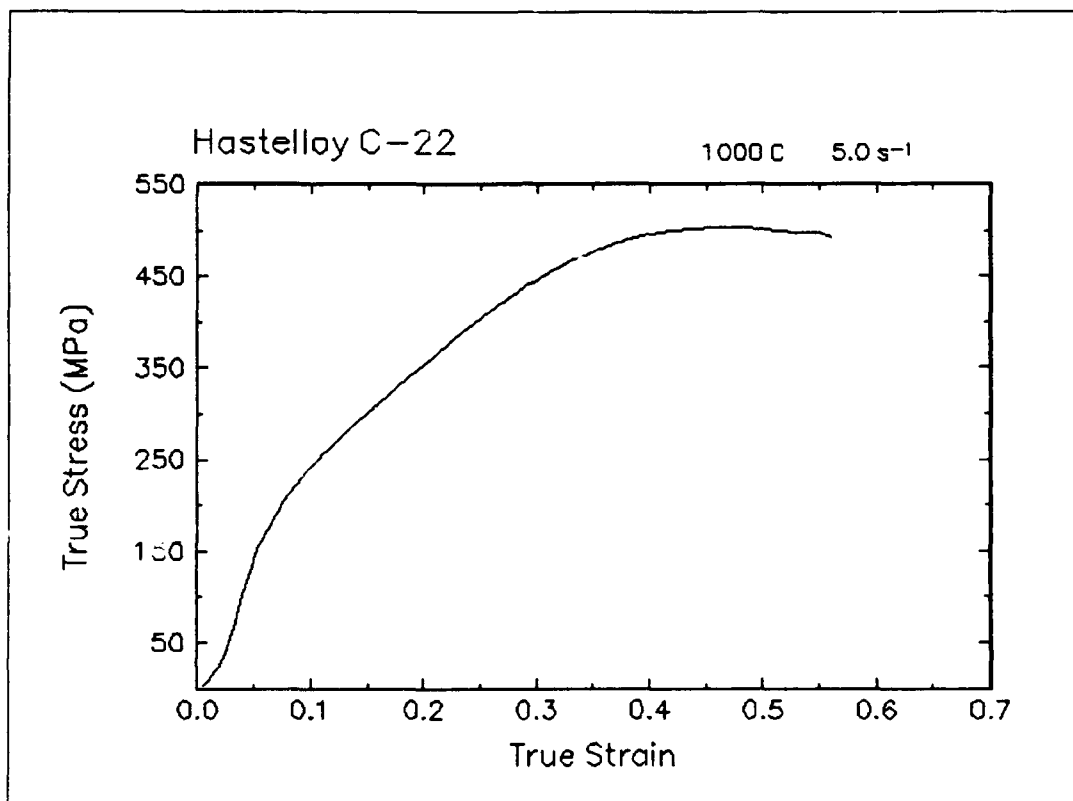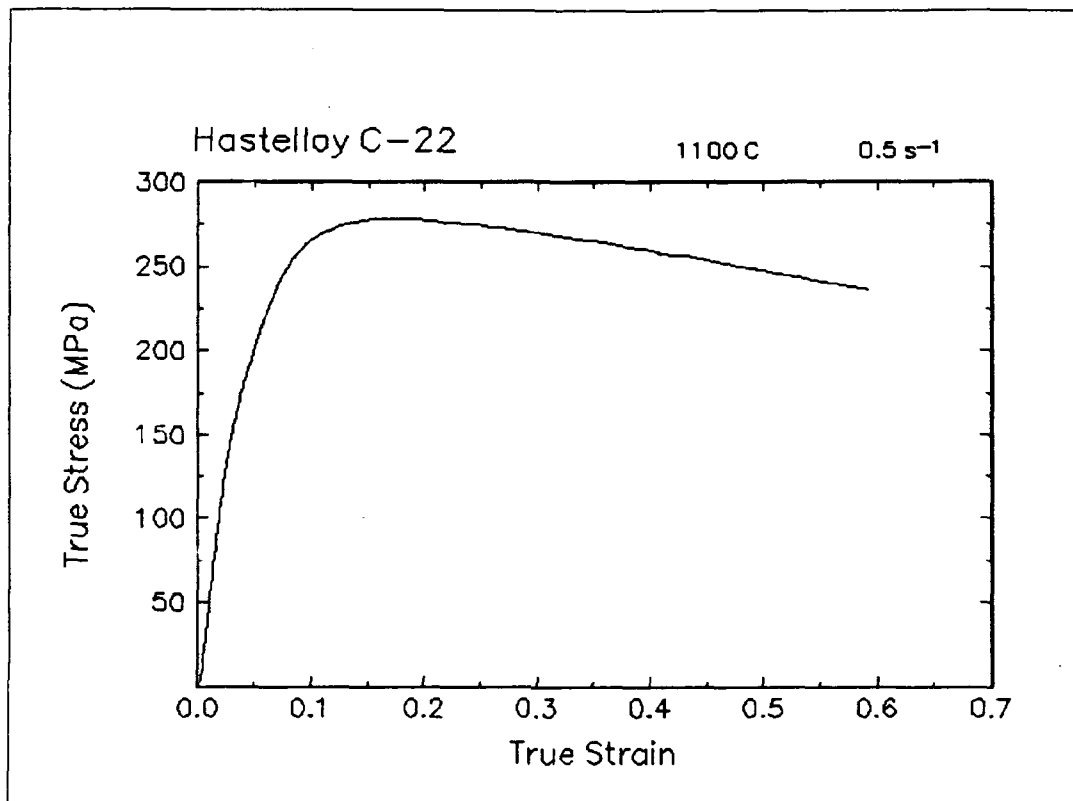
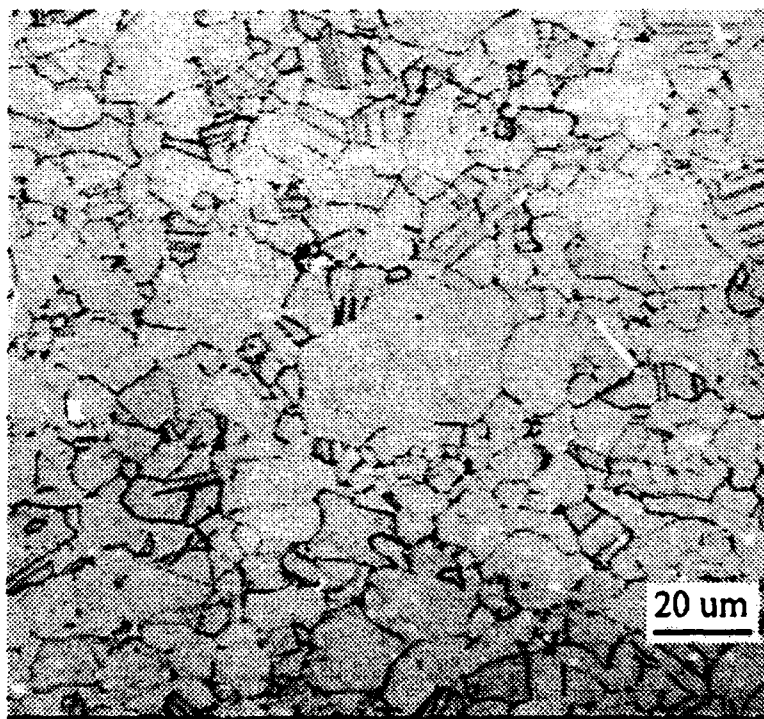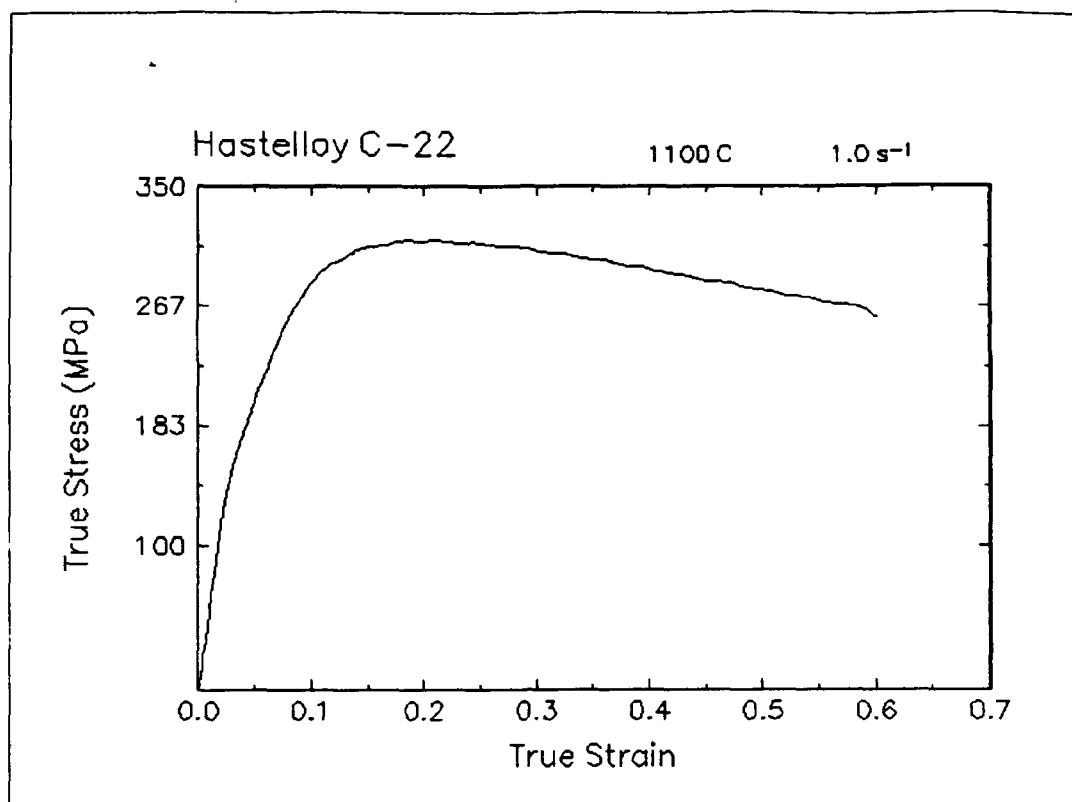Figure 16. True stress-true strain curve, 1000 C and 5 s⁻¹.

Figure 17. True stress-true strain curve and an optical micrograph from the center of the compressed sample cut through the compression axis, 1000 C and 20 s^{-1}.

20

Figure 18. True stress-true strain curve and an optical micrograph from the center of the compressed sample cut through the compression axis, 1050 C and 0.001 s^{-1}.

21
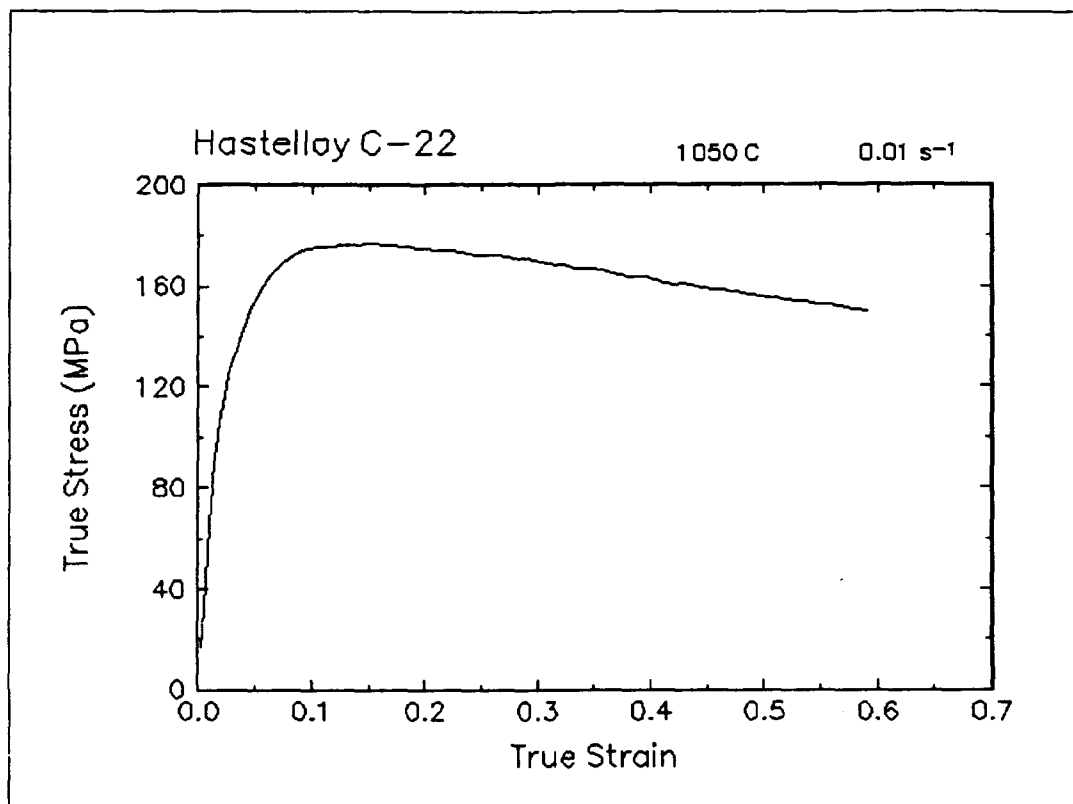
Figure 19. True stress-true strain curve, 1050 C and 0.01 s^{-1}.

Figure 20. True stress-true strain curve and an optical micrograph from the center of the compressed sample cut through the compression axis, 1050 C and 0.05 s⁻¹.
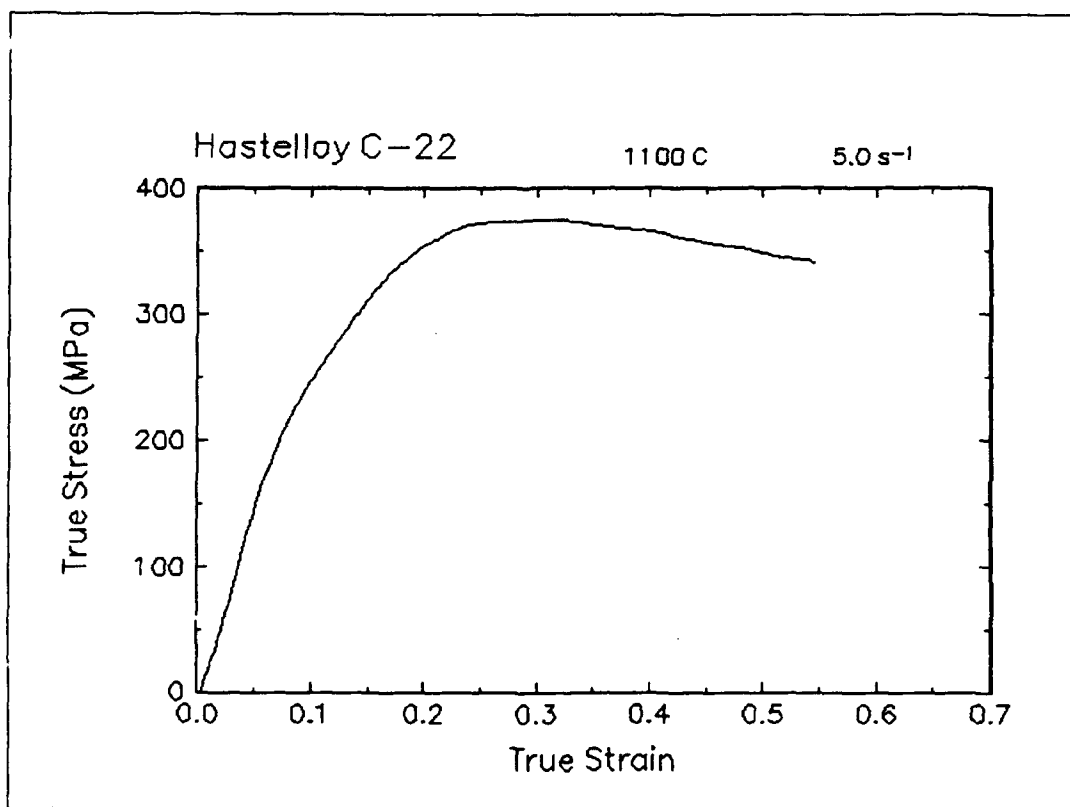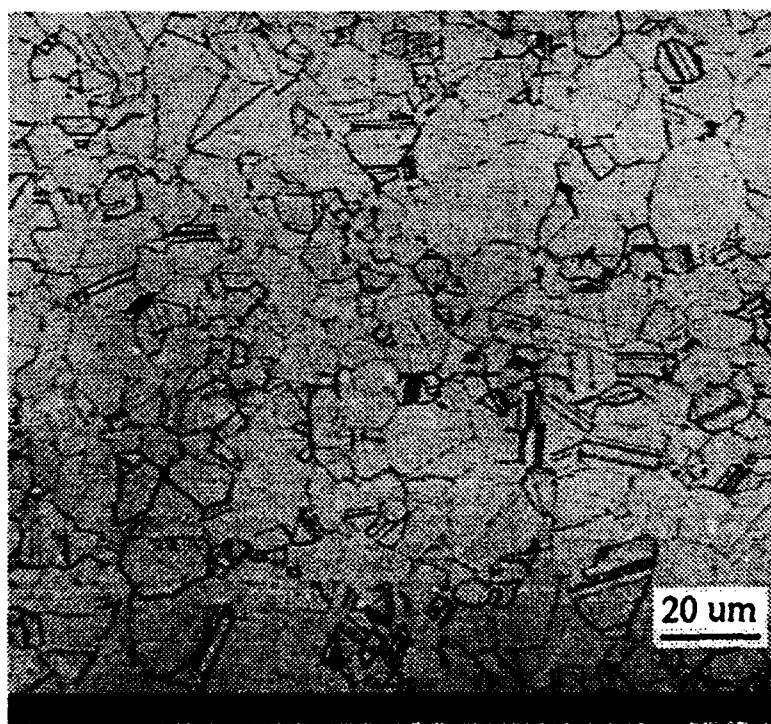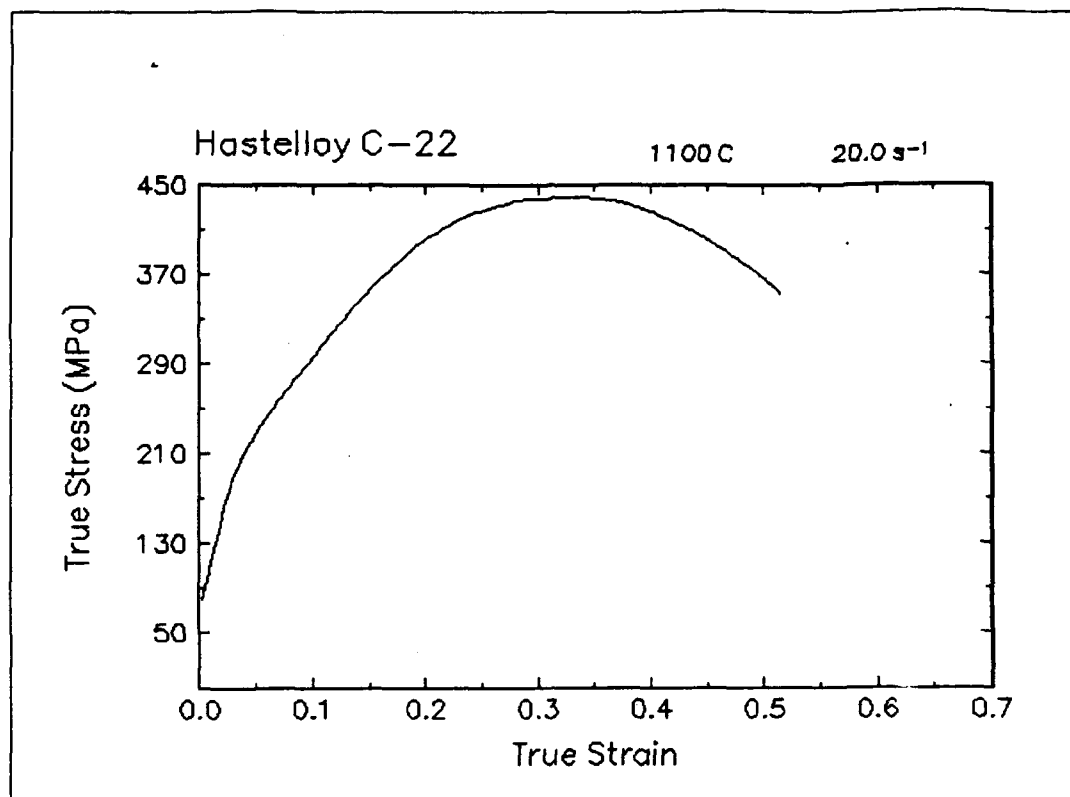
Figure 21. True stress-true strain curve, 1050 C and 0.1 s⁻¹.

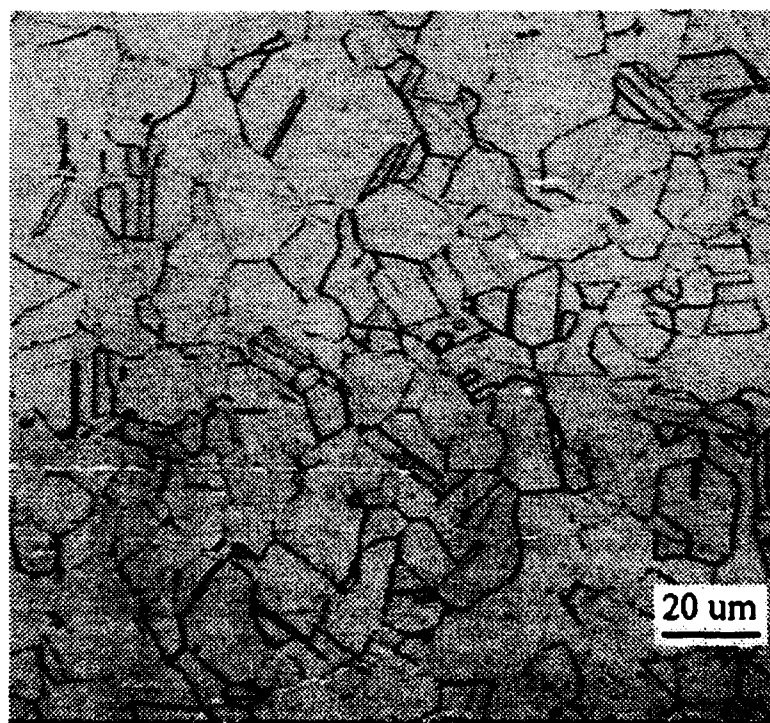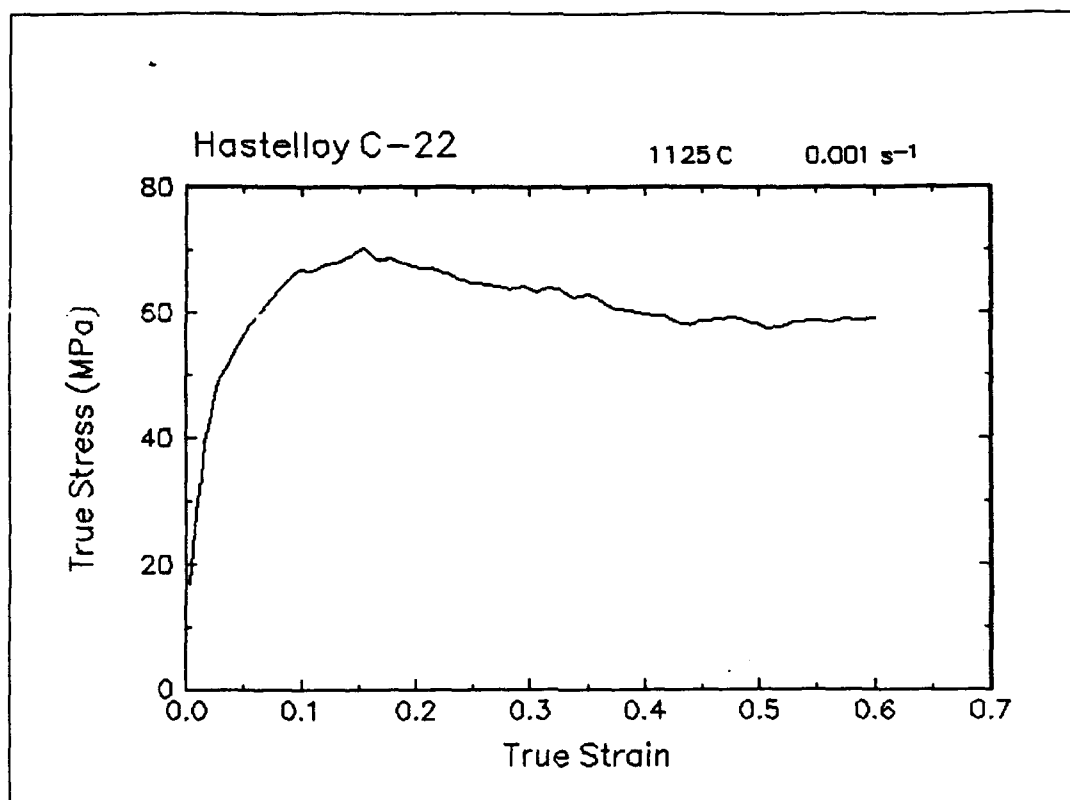Figure 22. True stress-true strain curve, 1050 C and 0.5 s^{-1}.

Figure 23. True stress-true strain curve and an optical micrograph from the center of the compressed sample cut through the compression axis, 1050 C and 1 s^{-1}.

Figure 24. True stress-true strain curve, 1050 C and 5 s^{-1}.

Figure 25. True stress-true strain curve and an optical micrograph from the center of the compressed sample cut through the compression axis, 1050 C and 20 s^{-1}.

28

Figure 26. True stress-true strain curve and an optical micrograph from the center of the compressed sample cut through the compression axis, 1100 C and 0.001 s^{-1}.
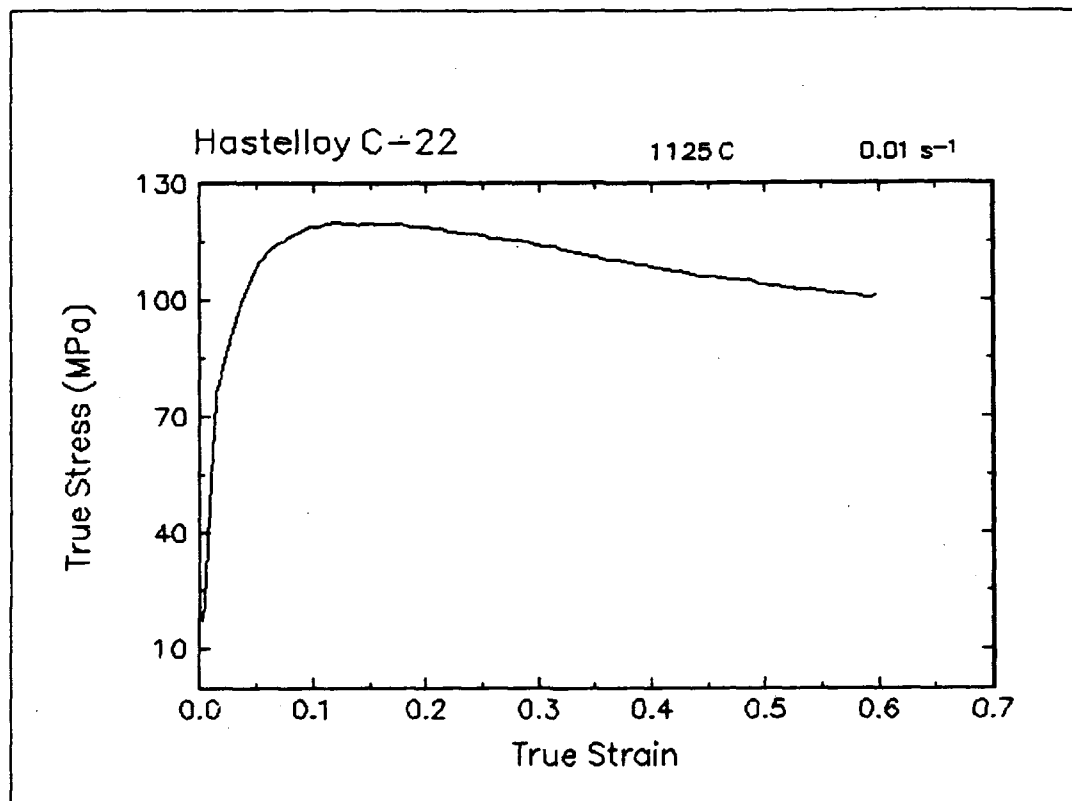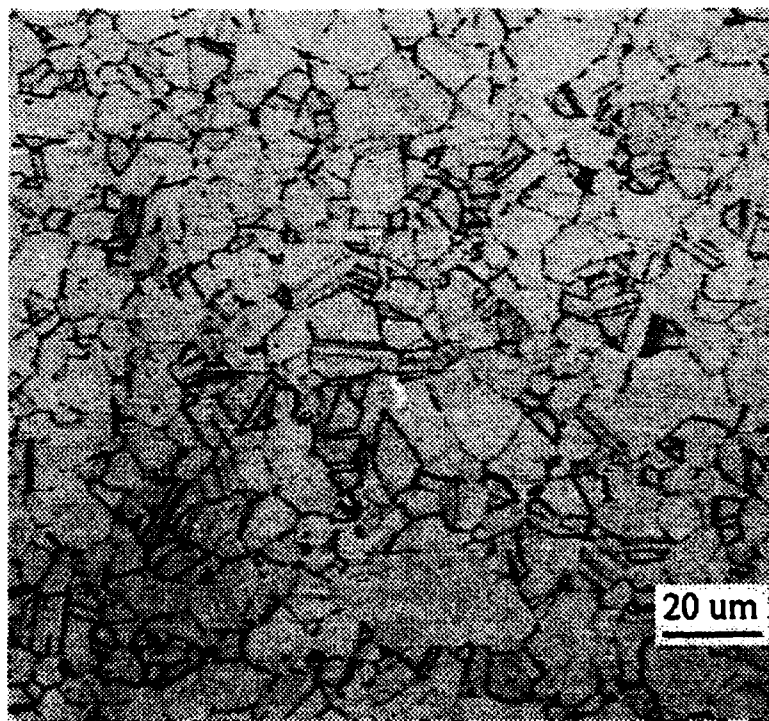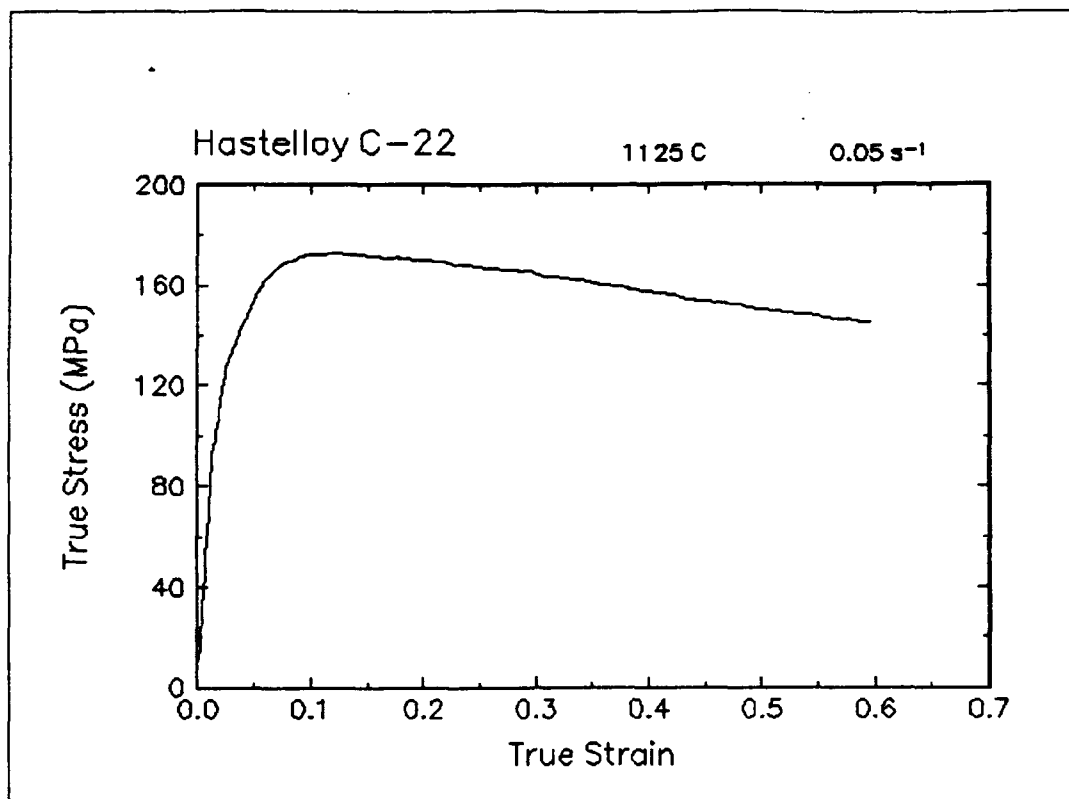
Figure 27. True stress-true strain curve and an optical micrograph from the center of the compressed sample cut through the compression axis, 1100 C and 0.01 s^{-1}.
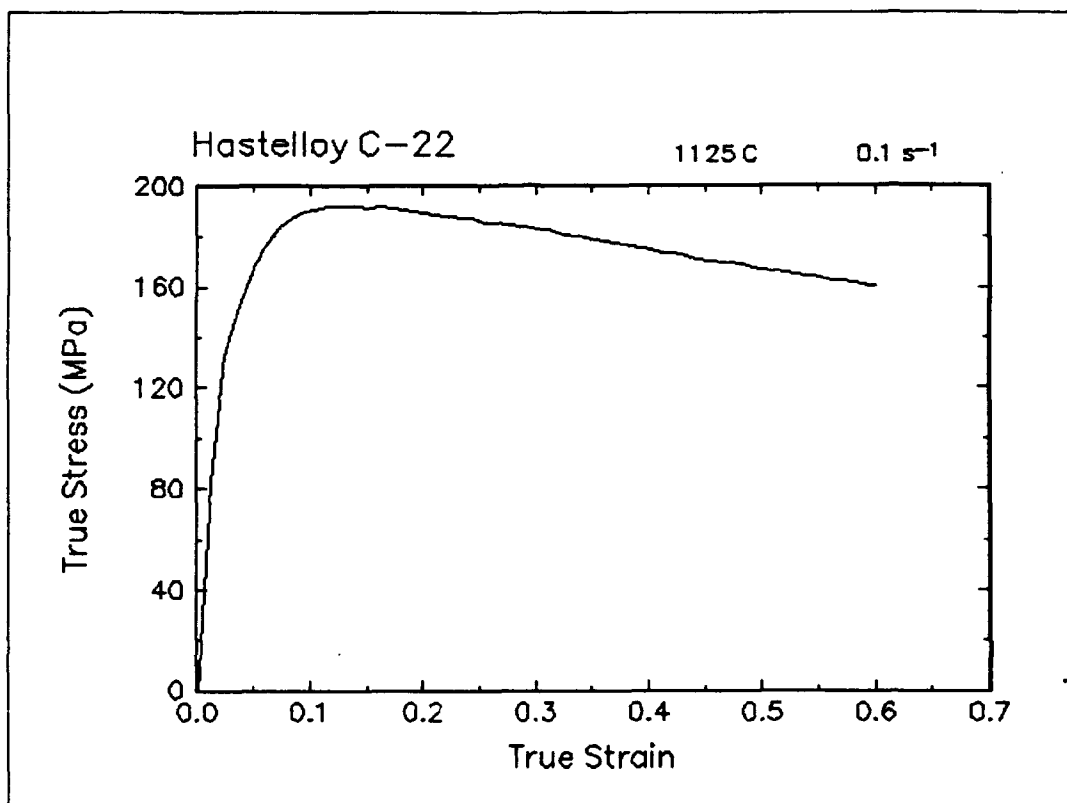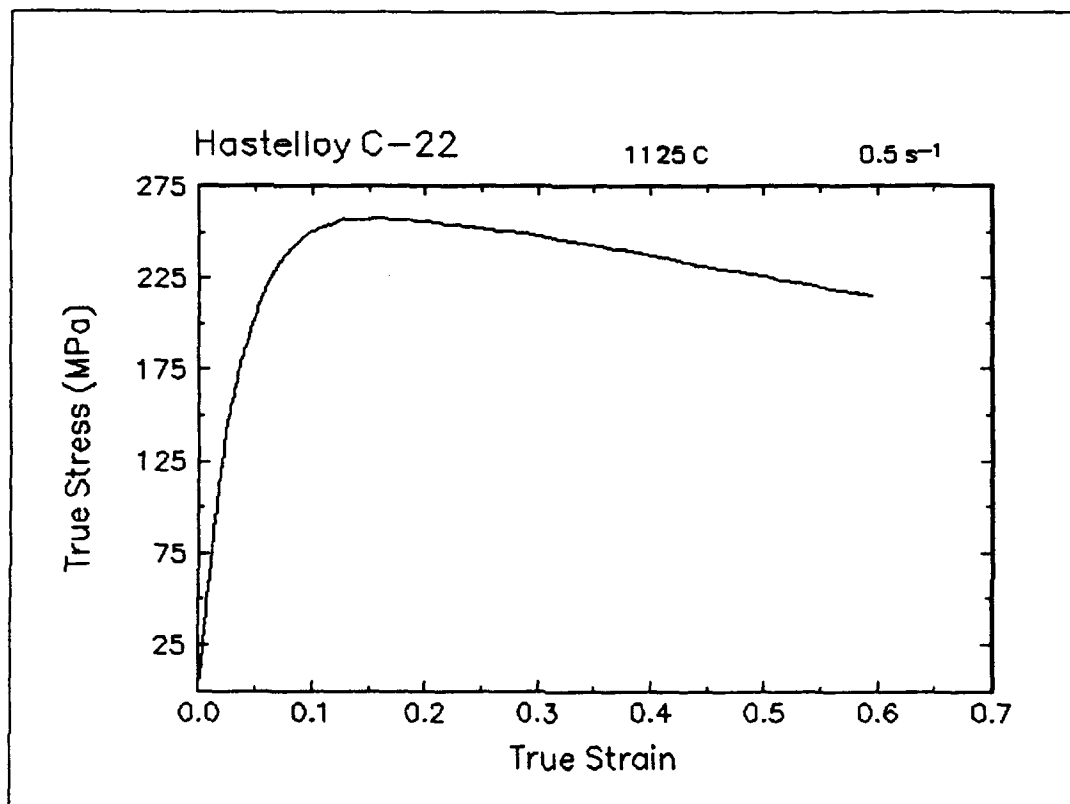
Figure 28. True stress-true strain curve, 1100 C and 0.05 s^{-1}.

Figure 29. True stress-true strain curve and an optical micrograph from the center of the compressed sample cut through the compression axis, 1100 C and 0.1 s^{-1}.

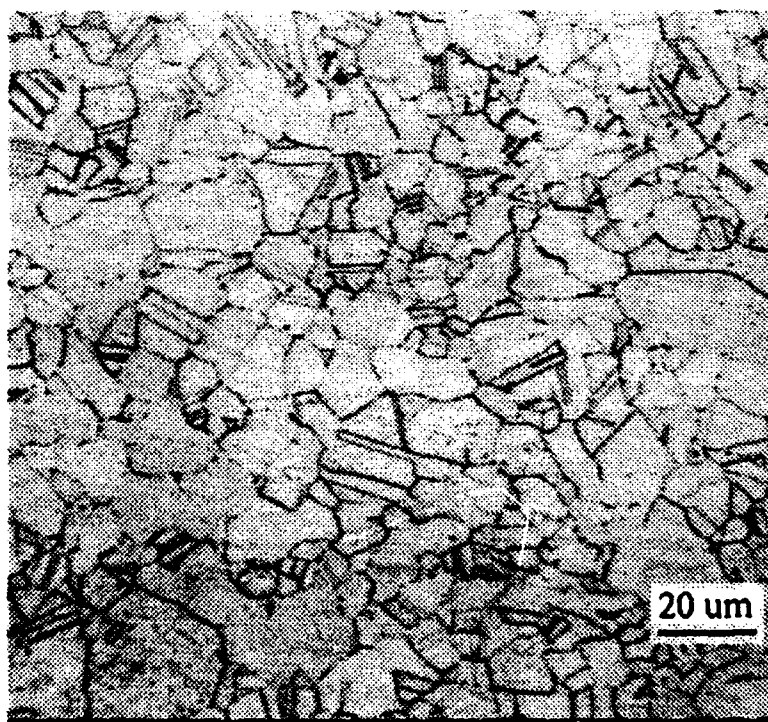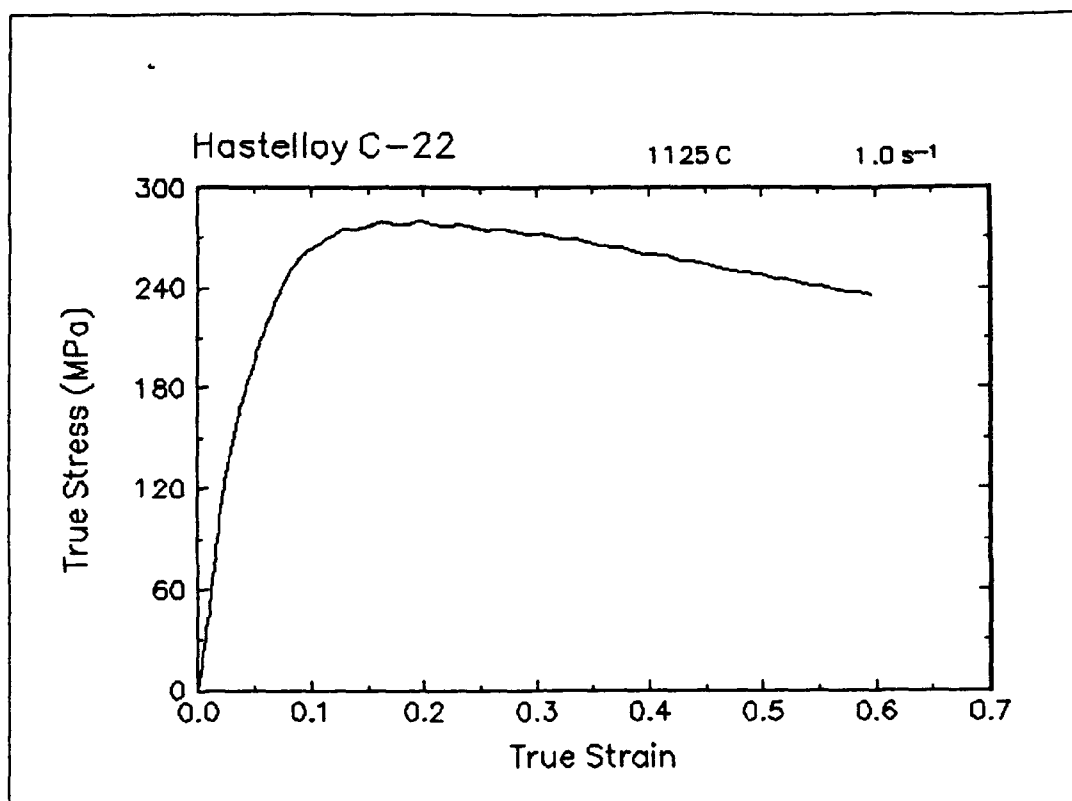Figure 30. True stress-true strain curve, 1100 C and 0.5 s^{-1}.

Figure 31. True stress-true strain curve and an optical micrograph from the center of the compressed sample cut through the compression axis, 1100 C and 1 s^{-1}.

Figure 32. True stress-true strain curve, 1100 C and 5 s^{-1}.

Figure 33. True stress-true strain curve and an optical micrograph from the center of the compressed sample cut through the compression axis, 1100 C and 20 s⁻¹.

Figure 34. True stress-true strain curve and an optical micrograph from the center of the compressed sample cut through the compression axis, 1125 C and 0.001 s⁻¹.
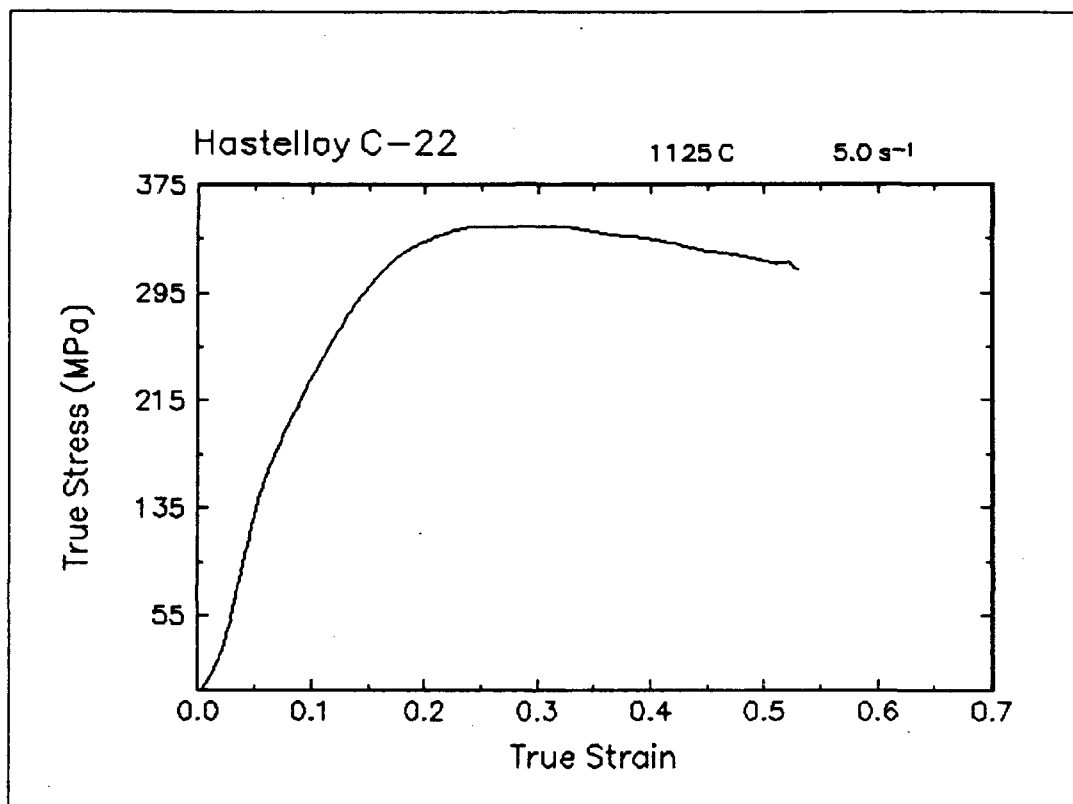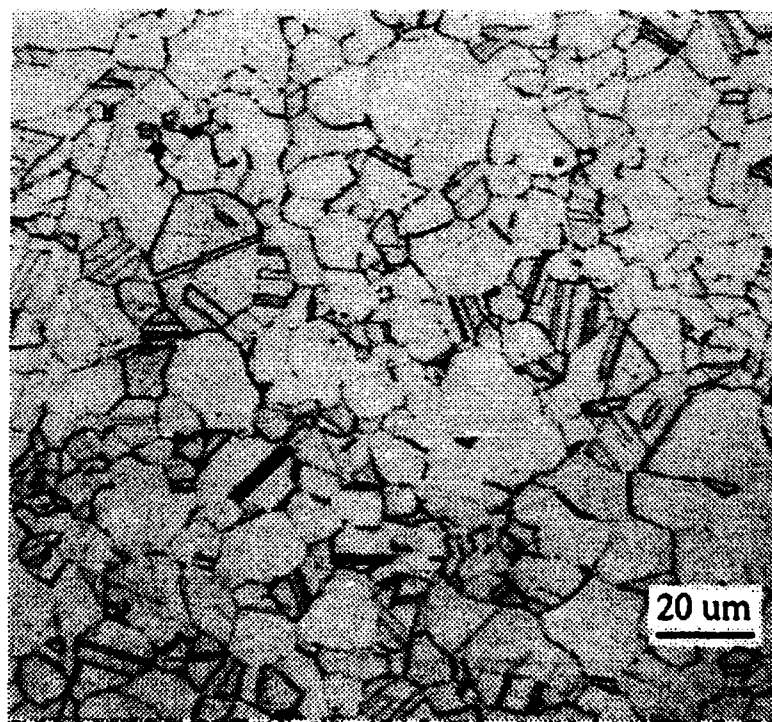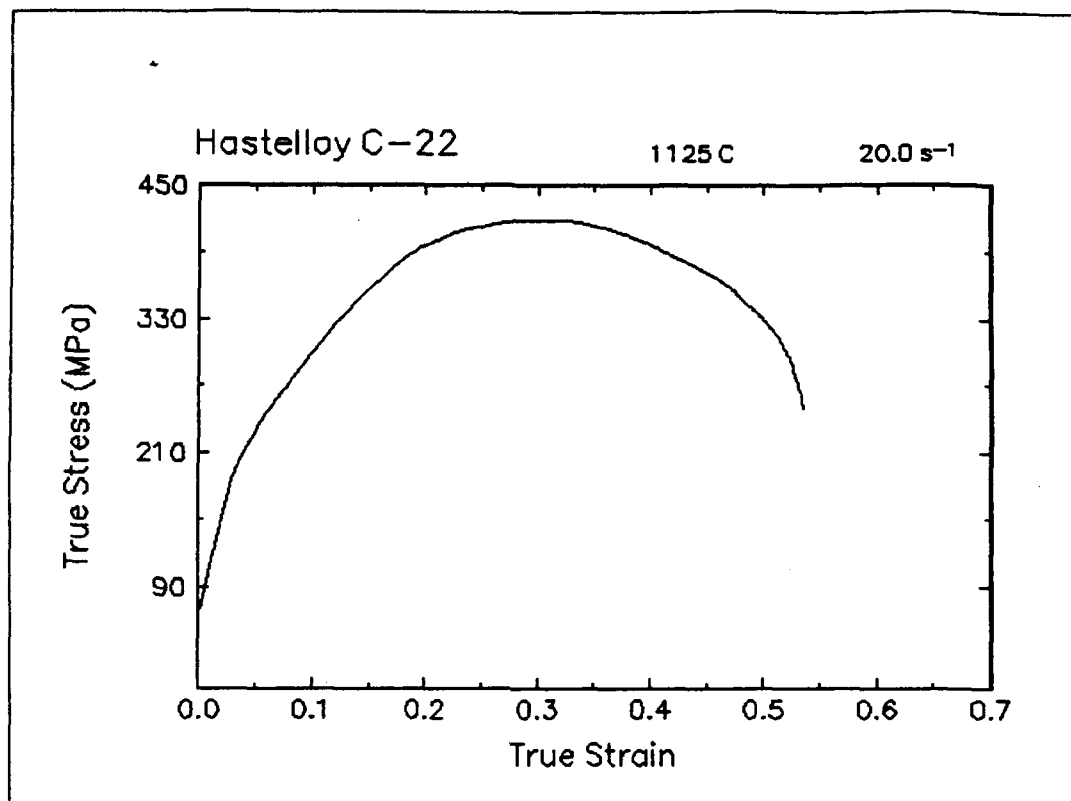
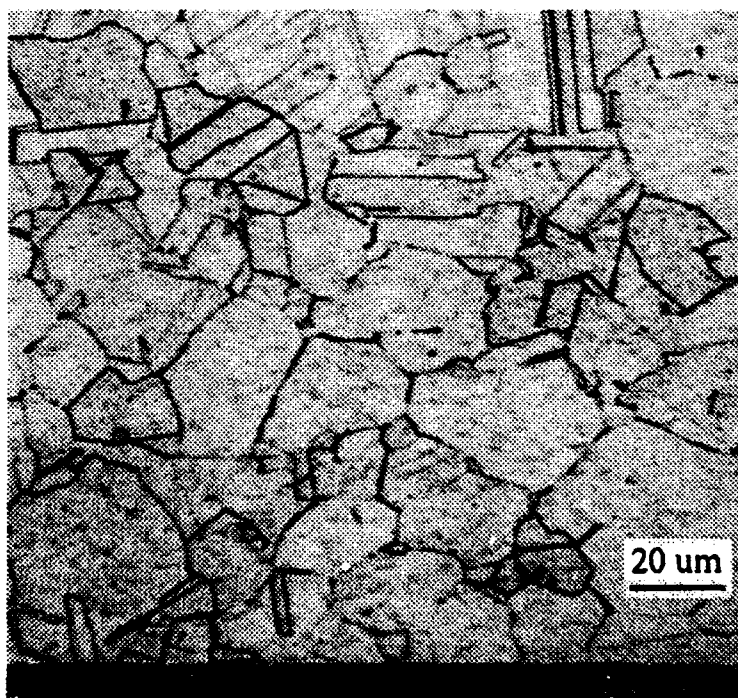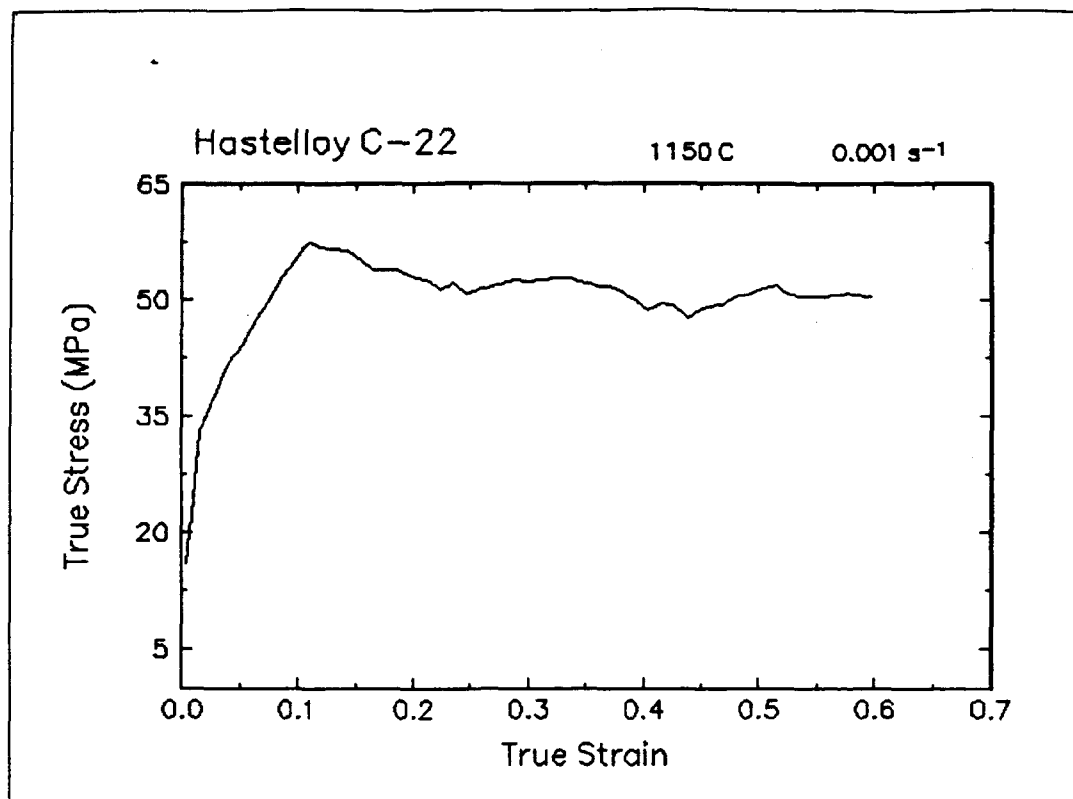Figure 35. True stress-true strain curve, 1125 C and 0.01 s^{-1}.

Figure 36. True stress-true strain curve and an optical micrograph from the center of the compressed sample cut through the compression axis, 1125 C and 0.05 s^{-1}.

39

Figure 37. True stress-true strain curve, 1125 C and 0.1 s^{-1}.

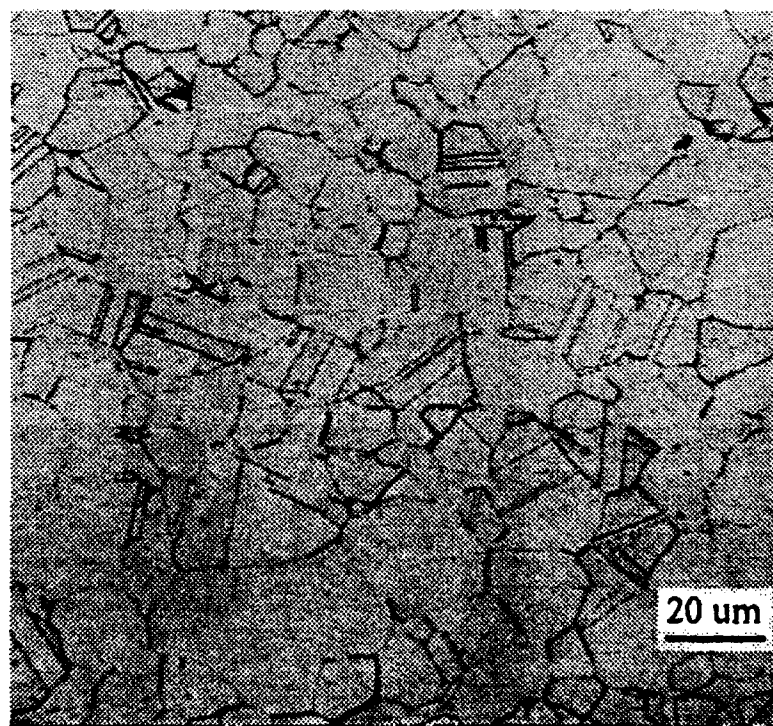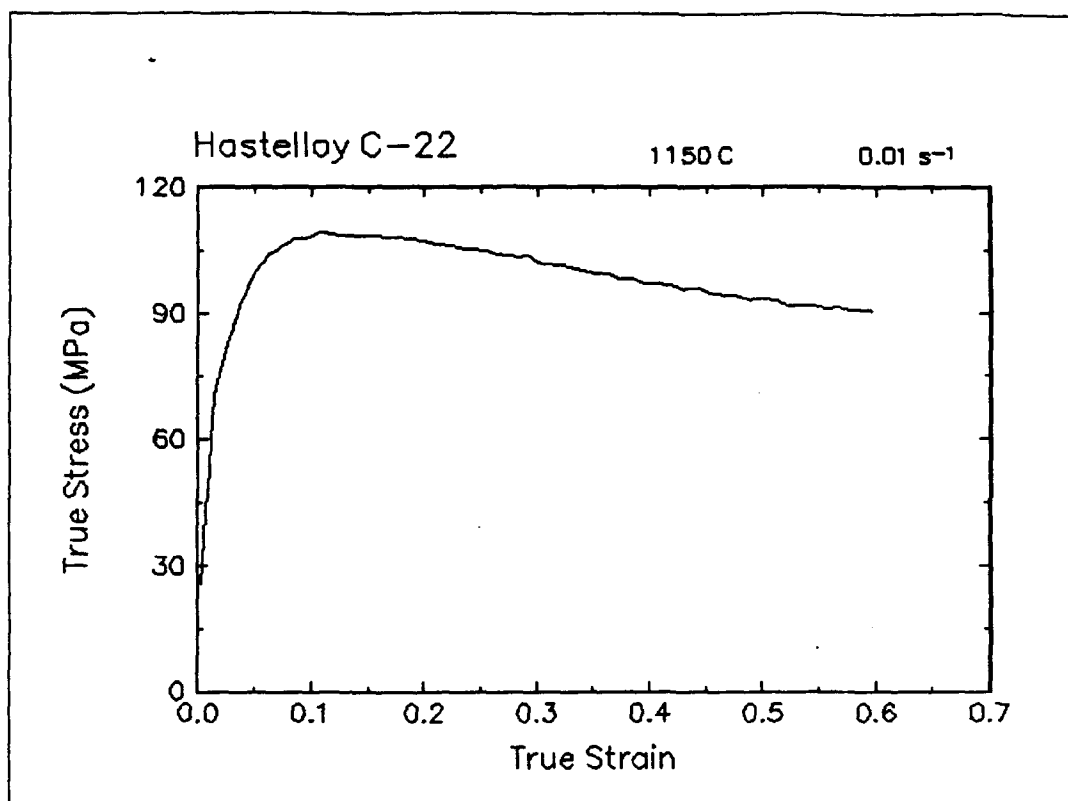Figure 38. True stress-true strain curve, 1125 C and 0.5 s^{-1}.

Figure 39.   True stress-true strain curve and an optical micrograph from the center of the compressed sample cut through the compression axis, 1125 C and 1 s⁻¹.
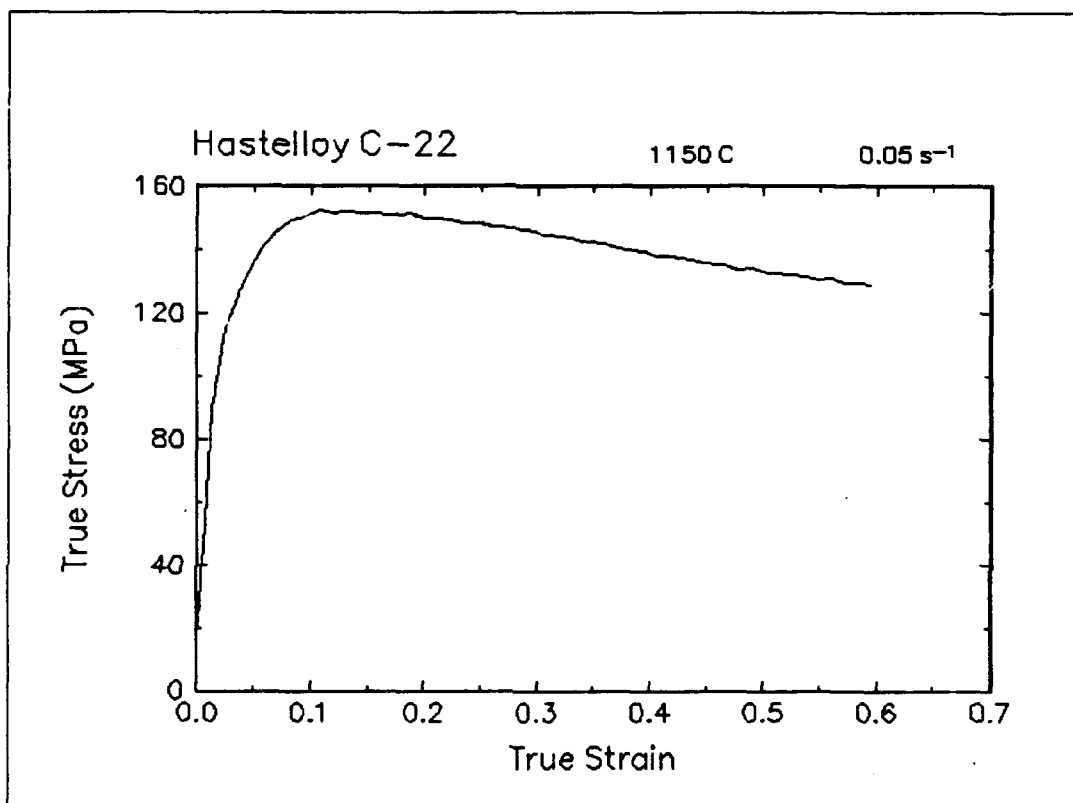
Figure 40. True stress-true strain curve, 1125 C and 5 s^{-1}.

Figure 41. True stress-true strain curve and an optical micrograph from the center of the compressed sample cut through the compression axis, 1125 C and 20 s^{-1}.
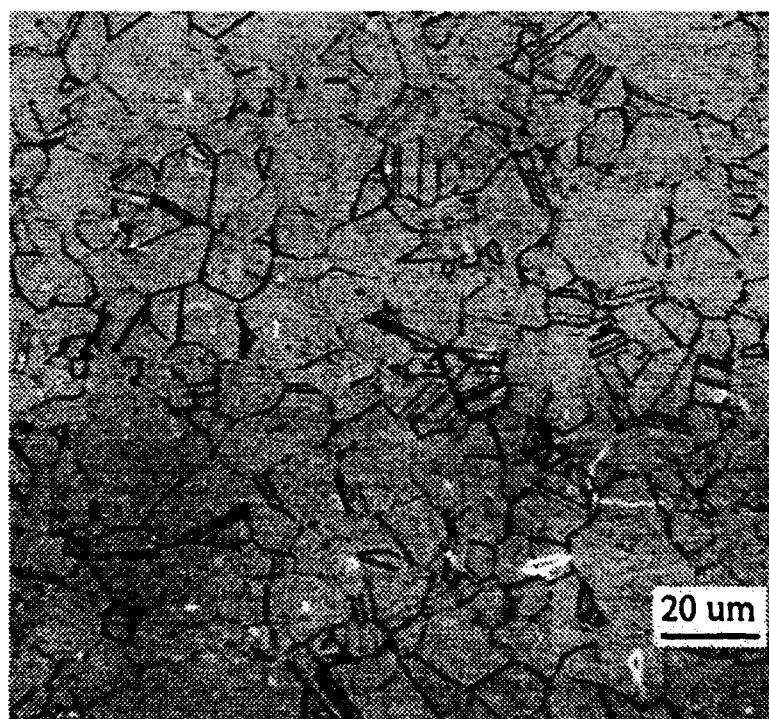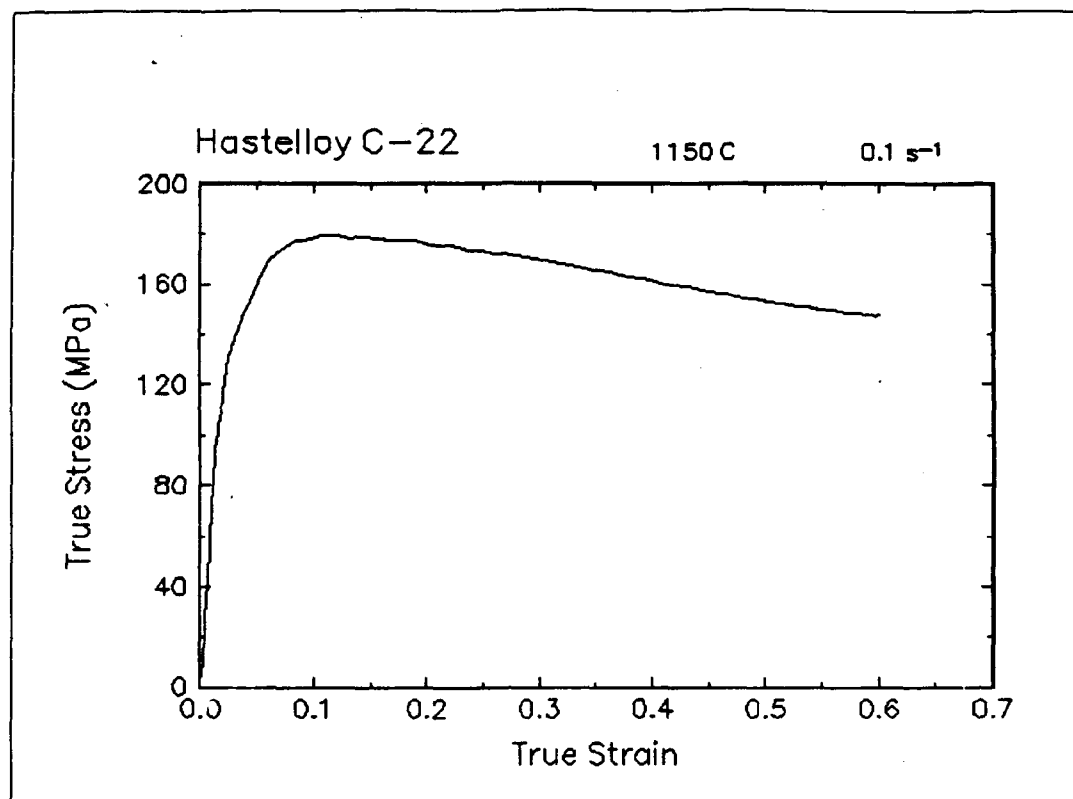
Figure 42.   True stress-true strain curve and an optical micrograph from the center of the compressed sample cut through the compression axis, 1150 C and 0.001 s^{-1}.

Figure 43. True stress-true strain curve and an optical micrograph from the center of the compressed sample cut through the compression axis, 1150 C and 0.01 s⁻¹.

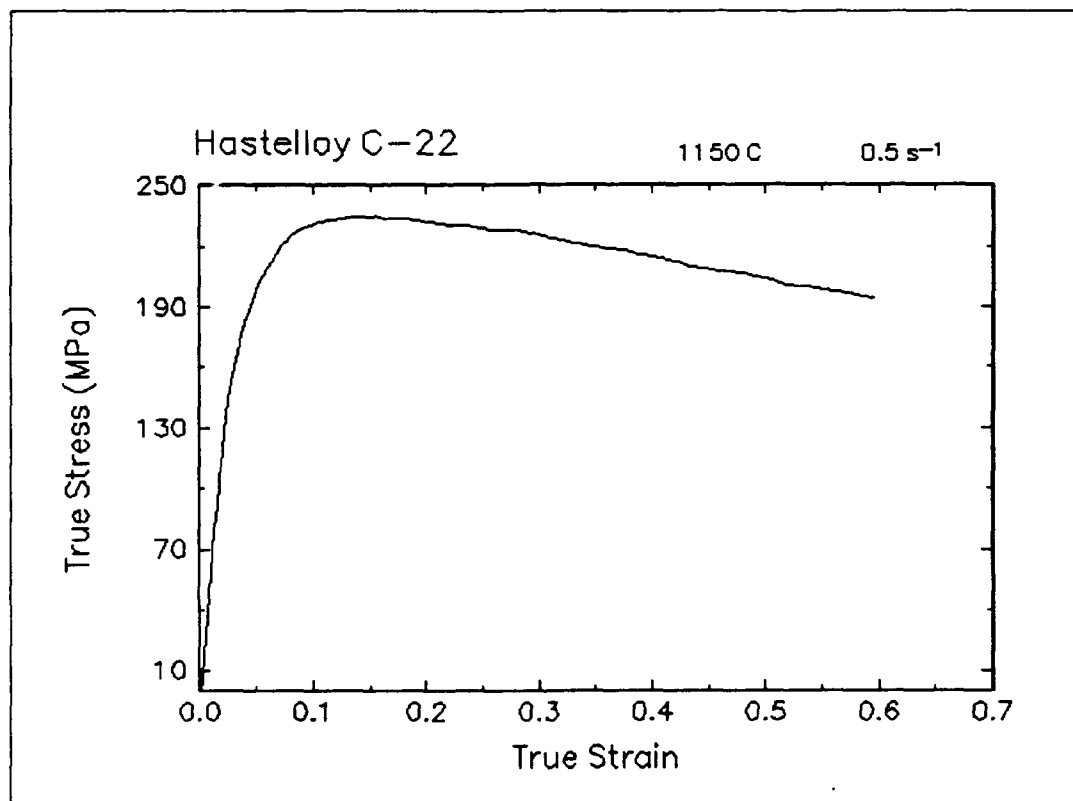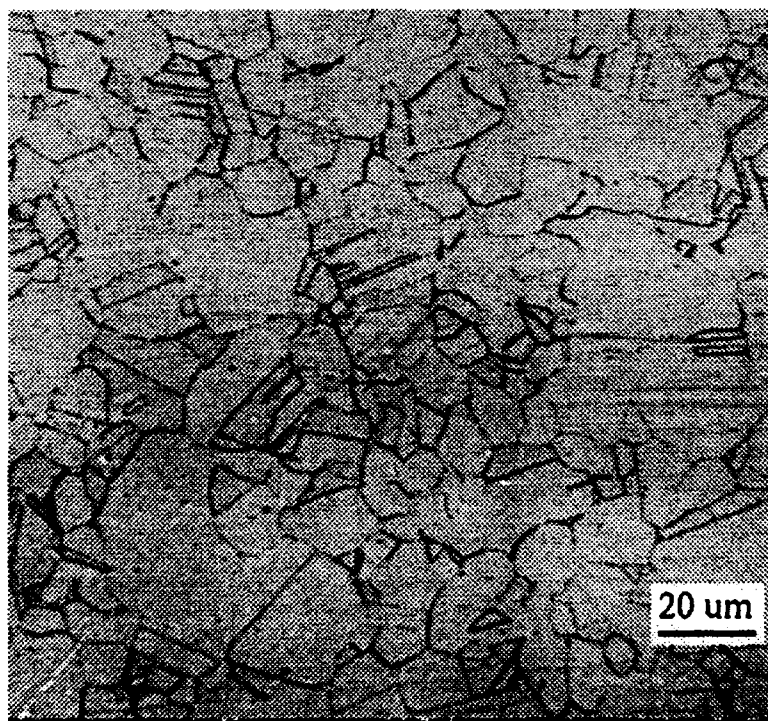Figure 44. True stress-true strain curve, 1150 C and 0.05 s^{-1}.

Figure 45. True stress-true strain curve and an optical micrograph from the center of the compressed sample cut through the compression axis, 1150 C and 0.1 s^{-1}.

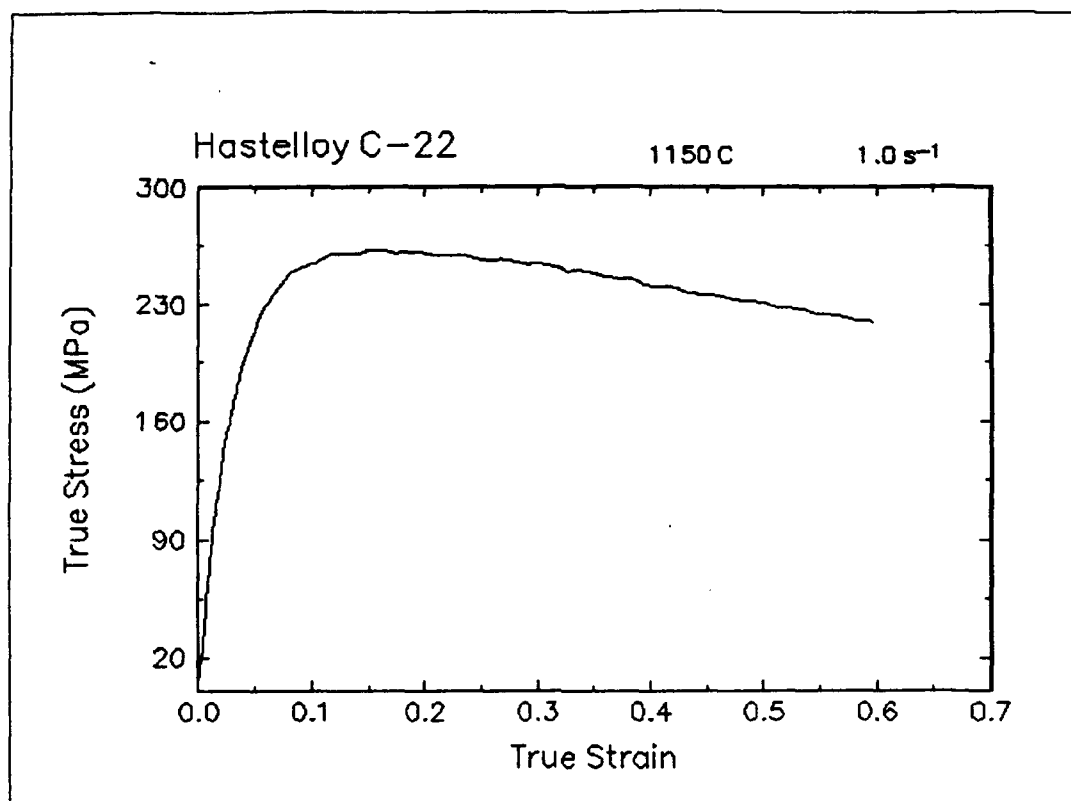Figure 46. True stress-true strain curve, 1150 C and 0.5 s⁻¹.

Figure 47. True stress-true strain curve and an optical micrograph from the center of the compressed sample cut through the compression axis, 1150 C and 1 s^{-1}.
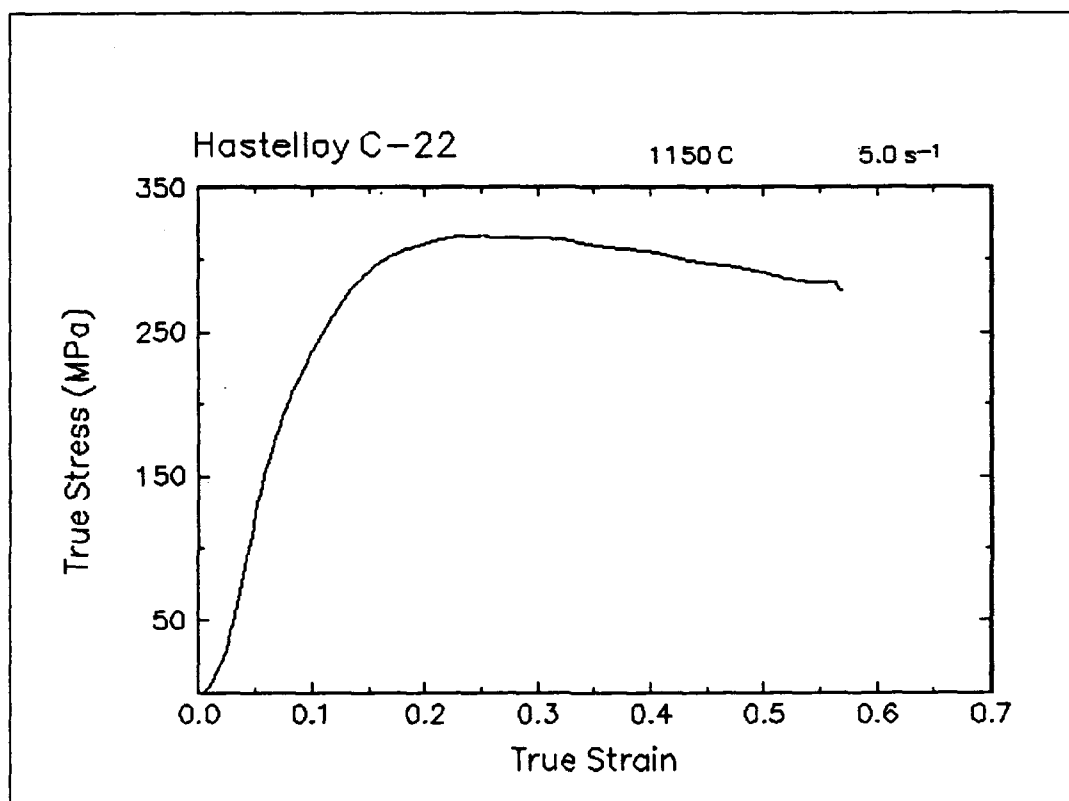
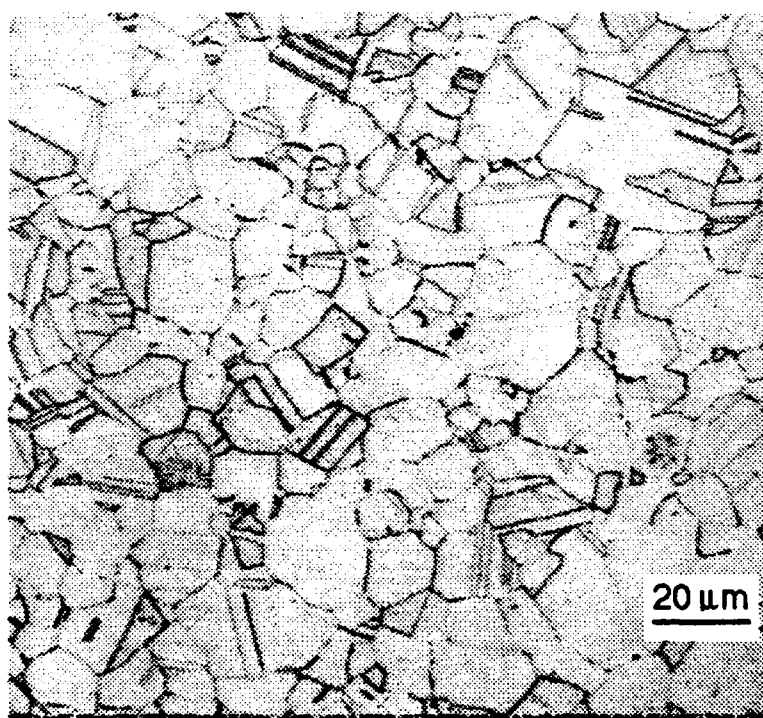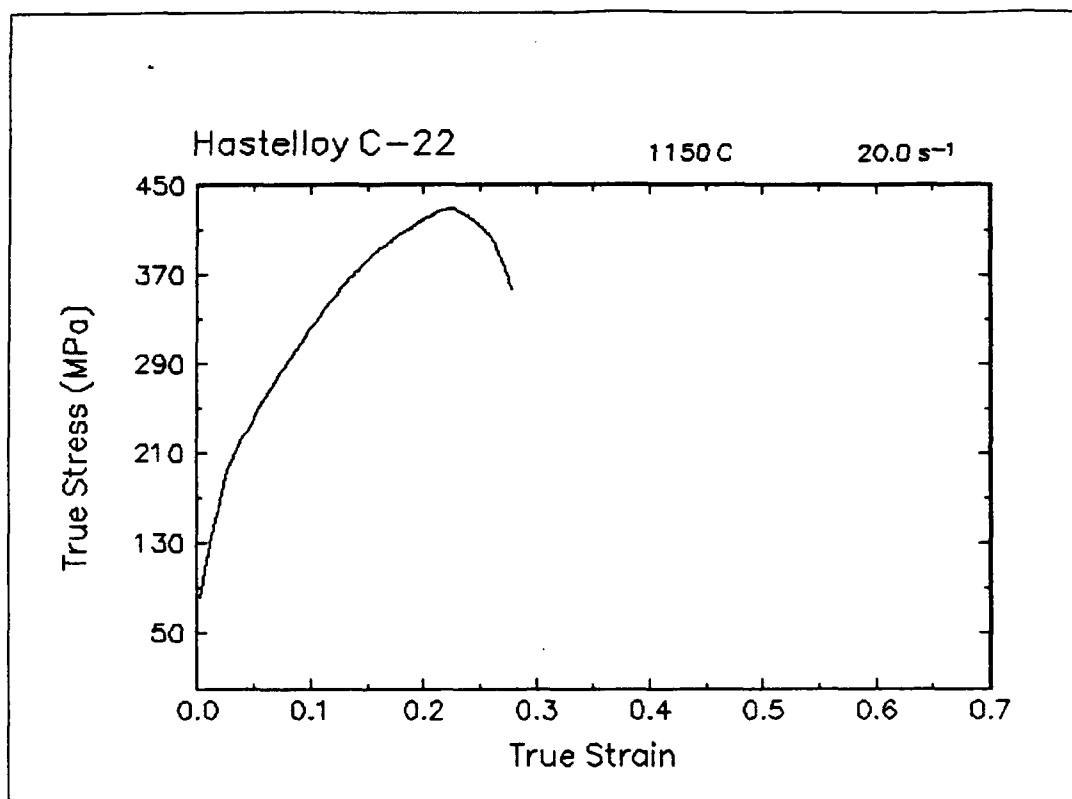Figure 48. True stress-true strain curve, 1150 C and 5 s^{-1}.

Figure 49.   True stress-true strain curve and an optical micrograph from the center of the compressed sample cut through the compression axis, 1150 C and 20 s^{-1}.
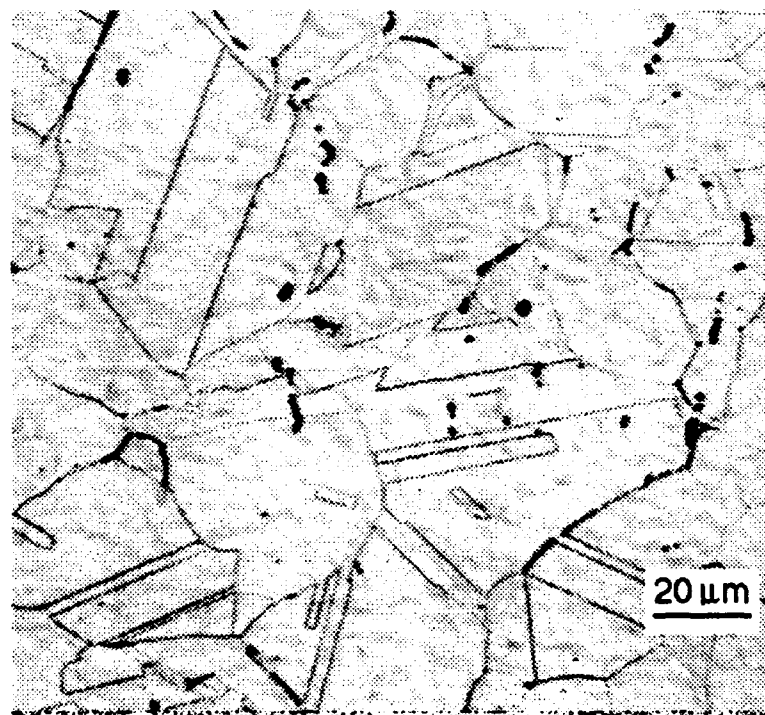
Figure 50. True stress-true strain curve and an optical micrograph from the center of the compressed sample cut through the compression axis, 1200 C and 0.001 s^{-1}.

Figure 51. True stress-true strain curve, 1200 C and 0.01 s^{-1}.
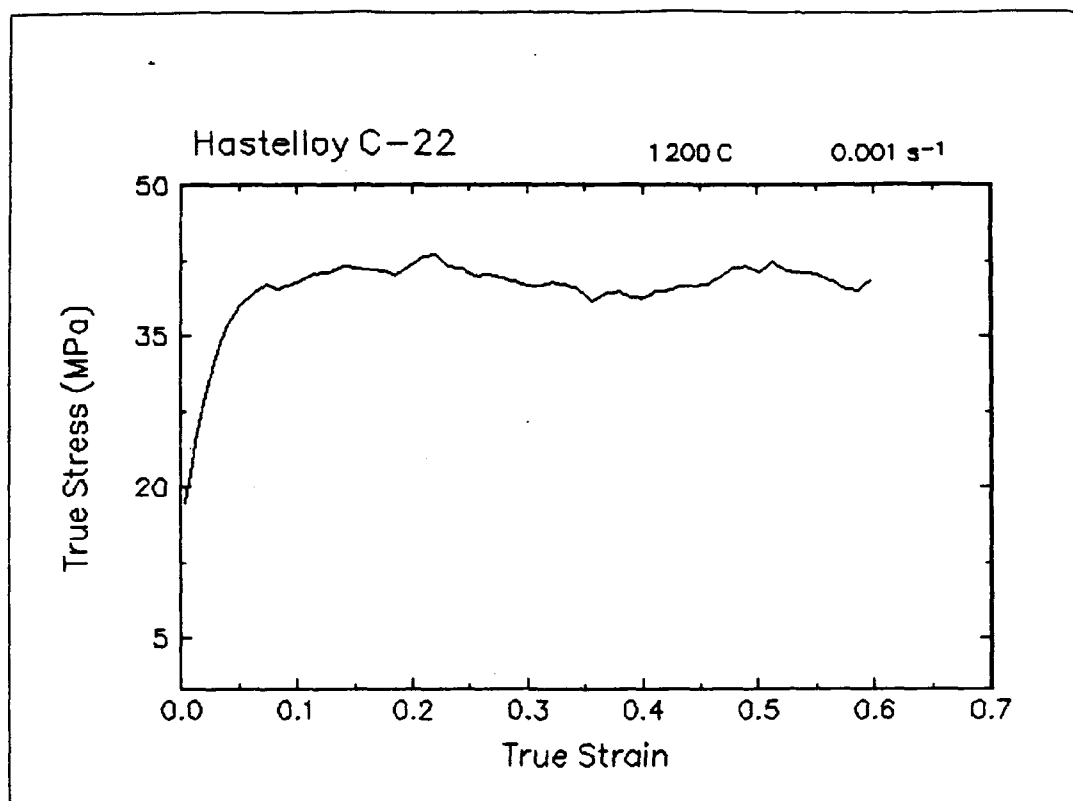
Figure 52. True stress-true strain curve and an optical micrograph from the center of the compressed sample cut through the compression axis, 1200 C and 0.05 s^{-1}.
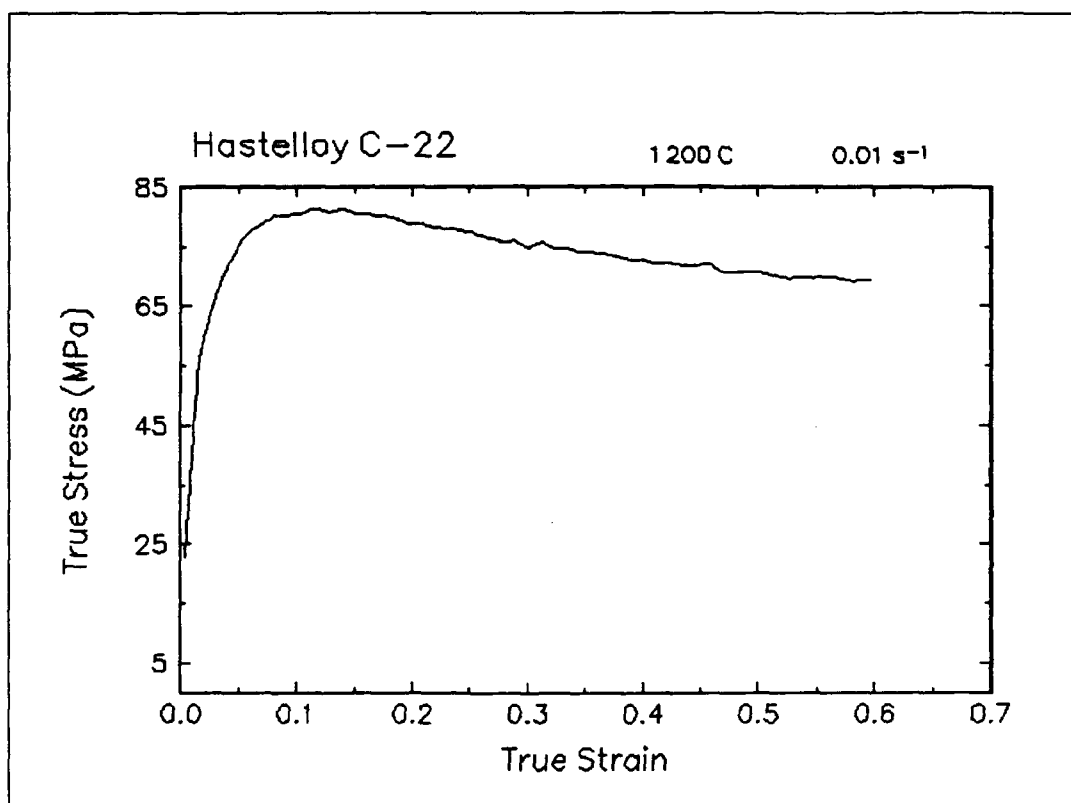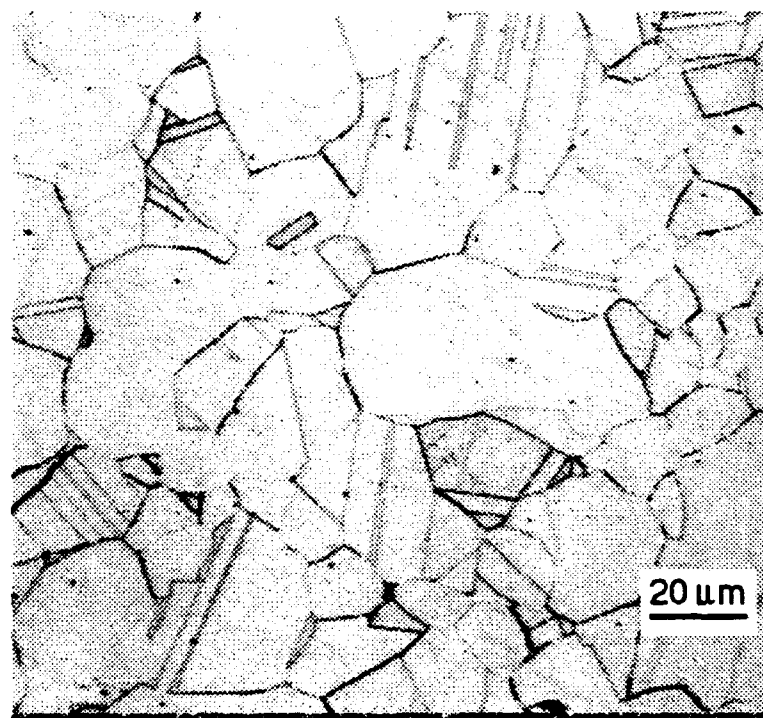
Figure 53.   True stress-true strain curve and an optical micrograph from the center of the compressed sample cut through the compression axis, 1200 C and 0.1 s⁻¹.

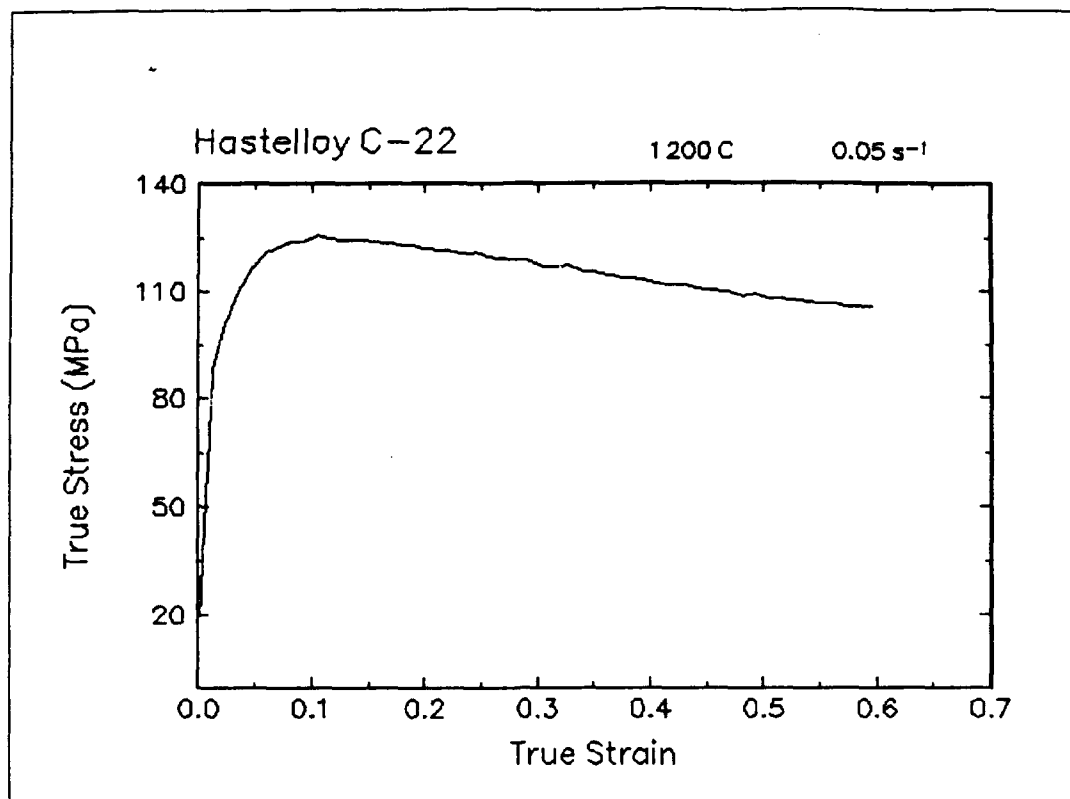Figure 54. True stress-true strain curve, 1200 C and 0.5 s⁻¹.

Figure 55. True stress-true strain curve and an optical micrograph from the center of the compressed sample cut through the compression axis, 1200 C and 1 s^{-1}.

Figure 56. True stress-true strain curve, 1200 C and 5 s^{-1}.
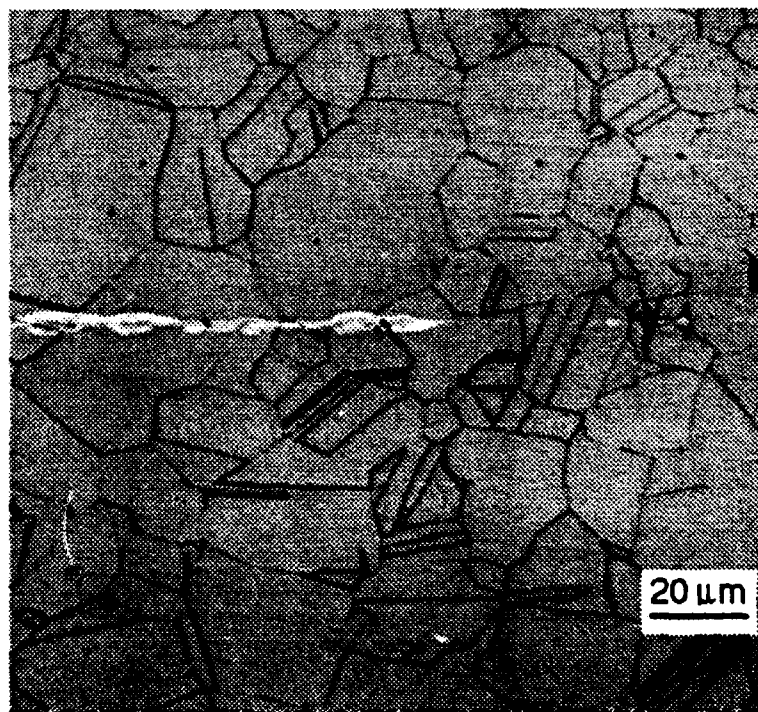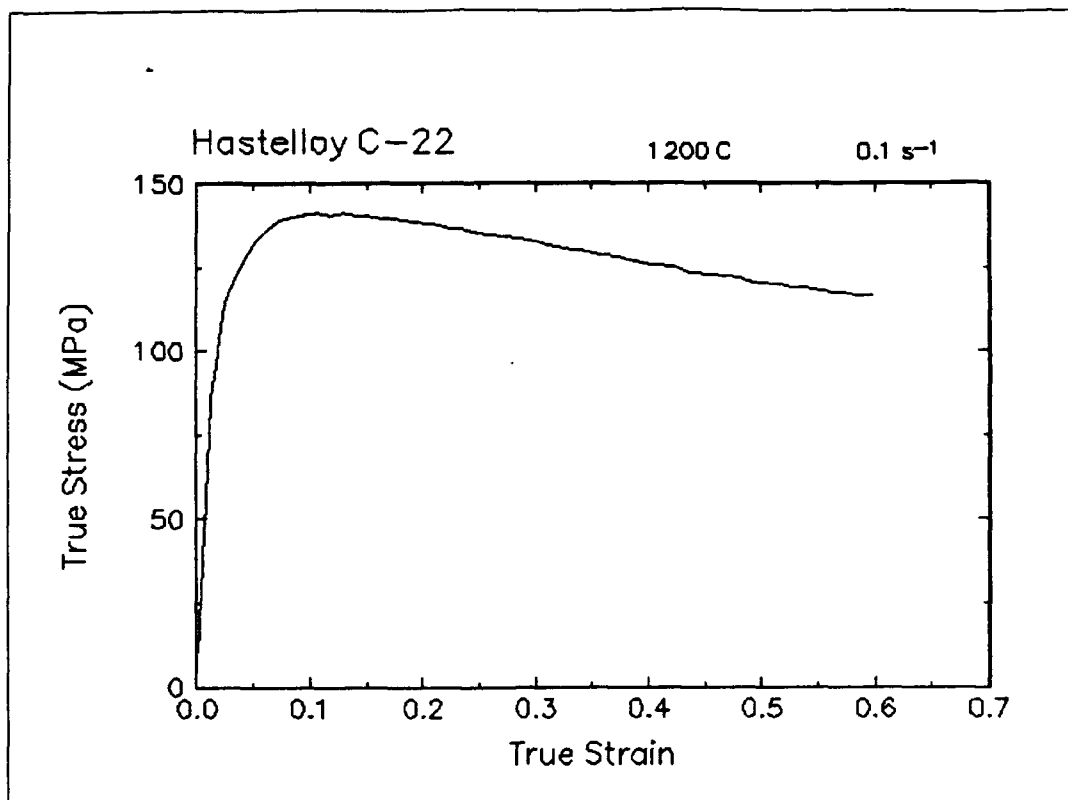
Figure 57. True stress-true strain curve and an optical micrograph from the center of the compressed sample cut through the compression axis, 1200 C and 20 s^{-1}.
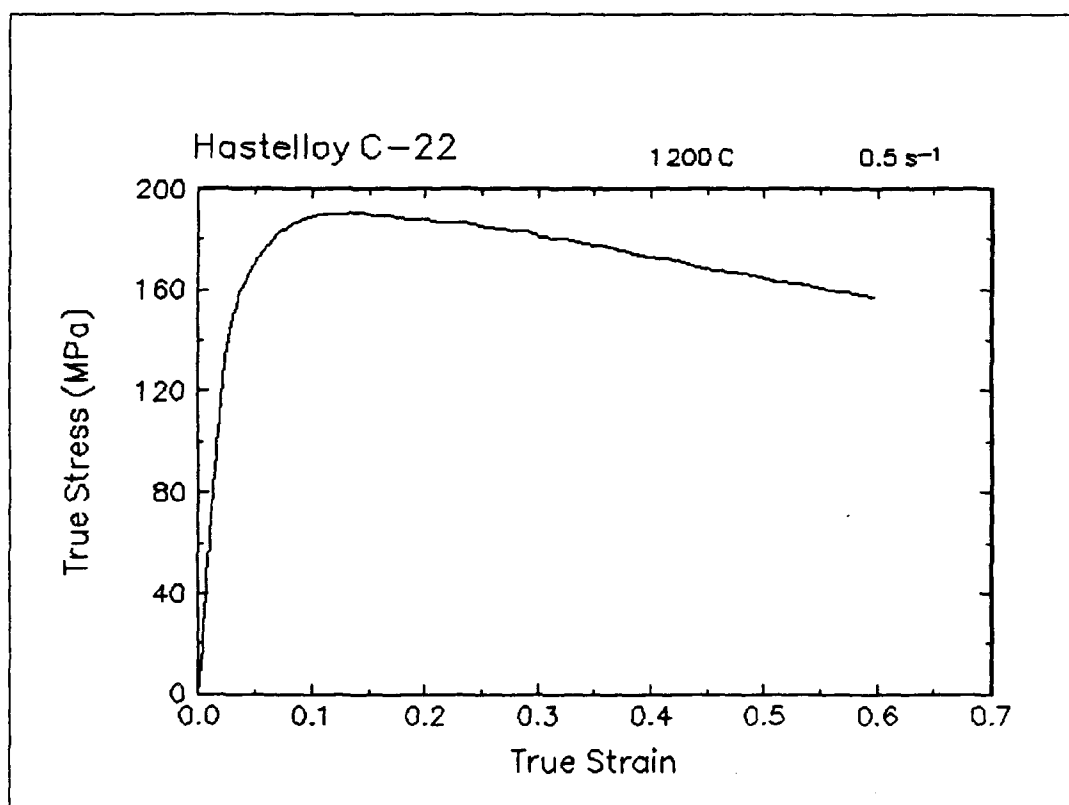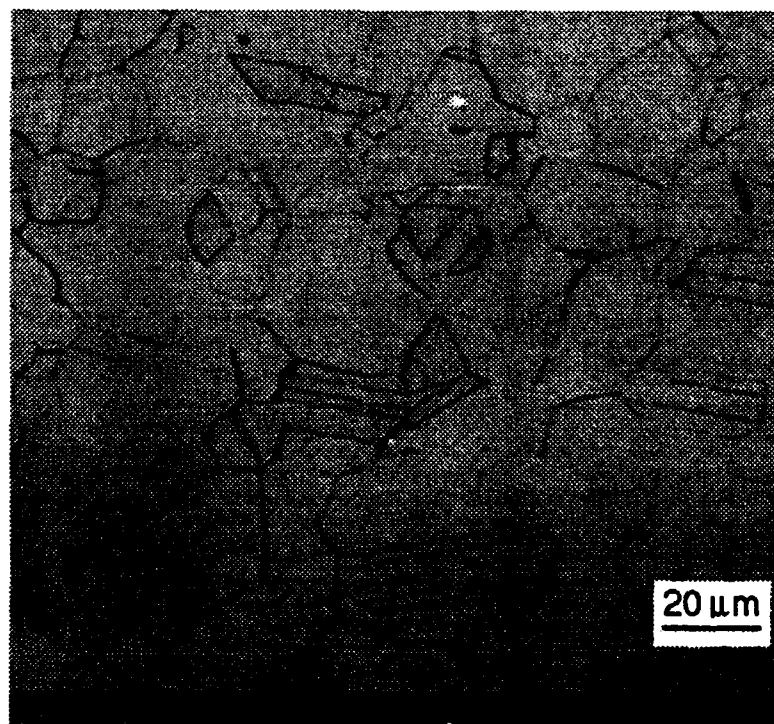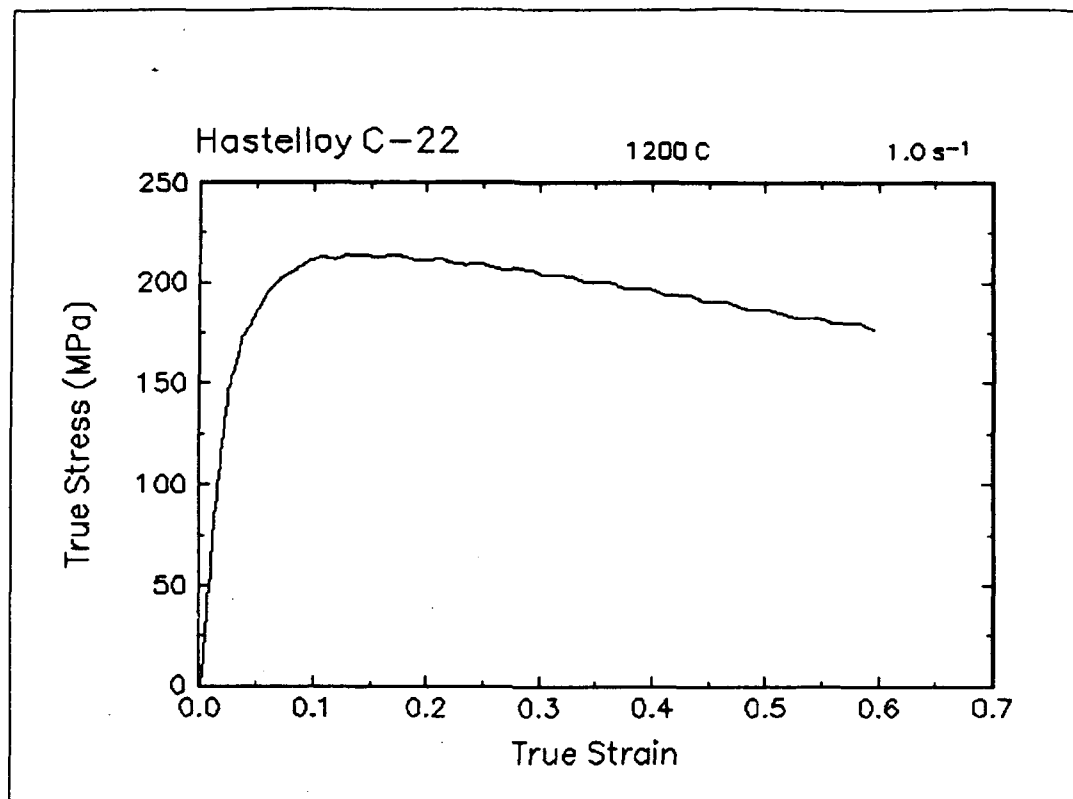
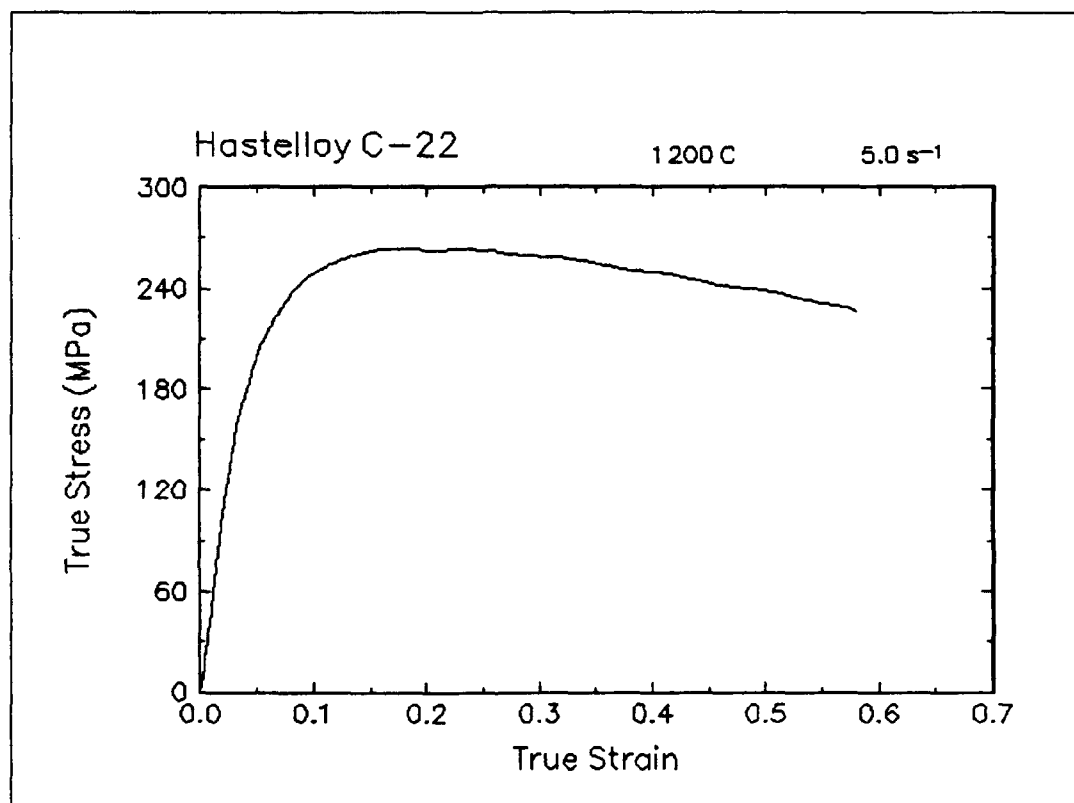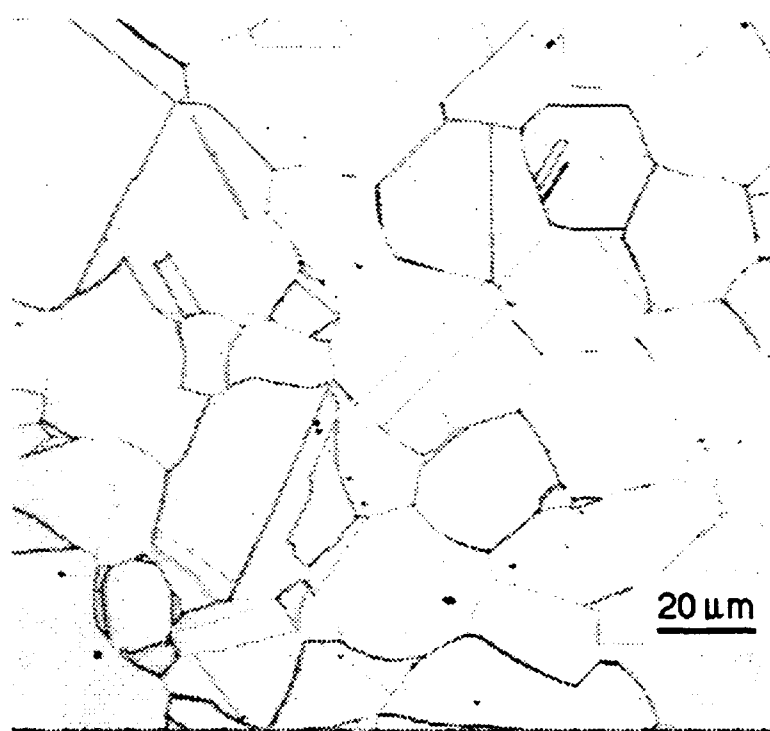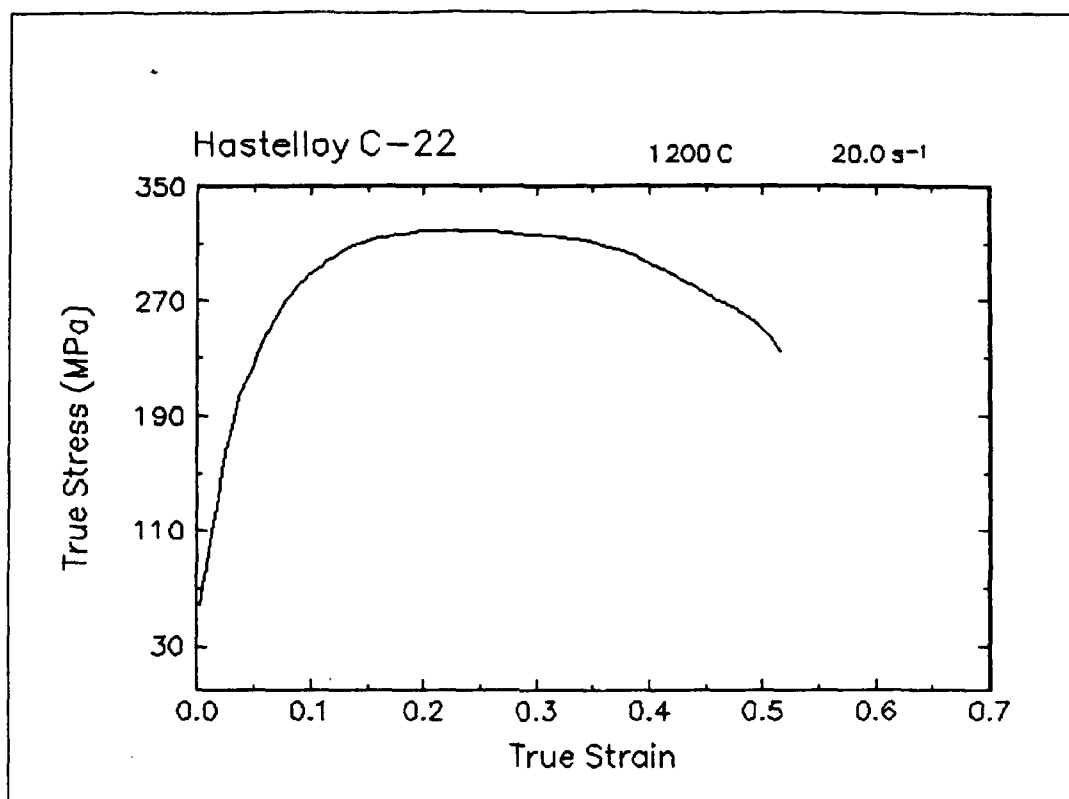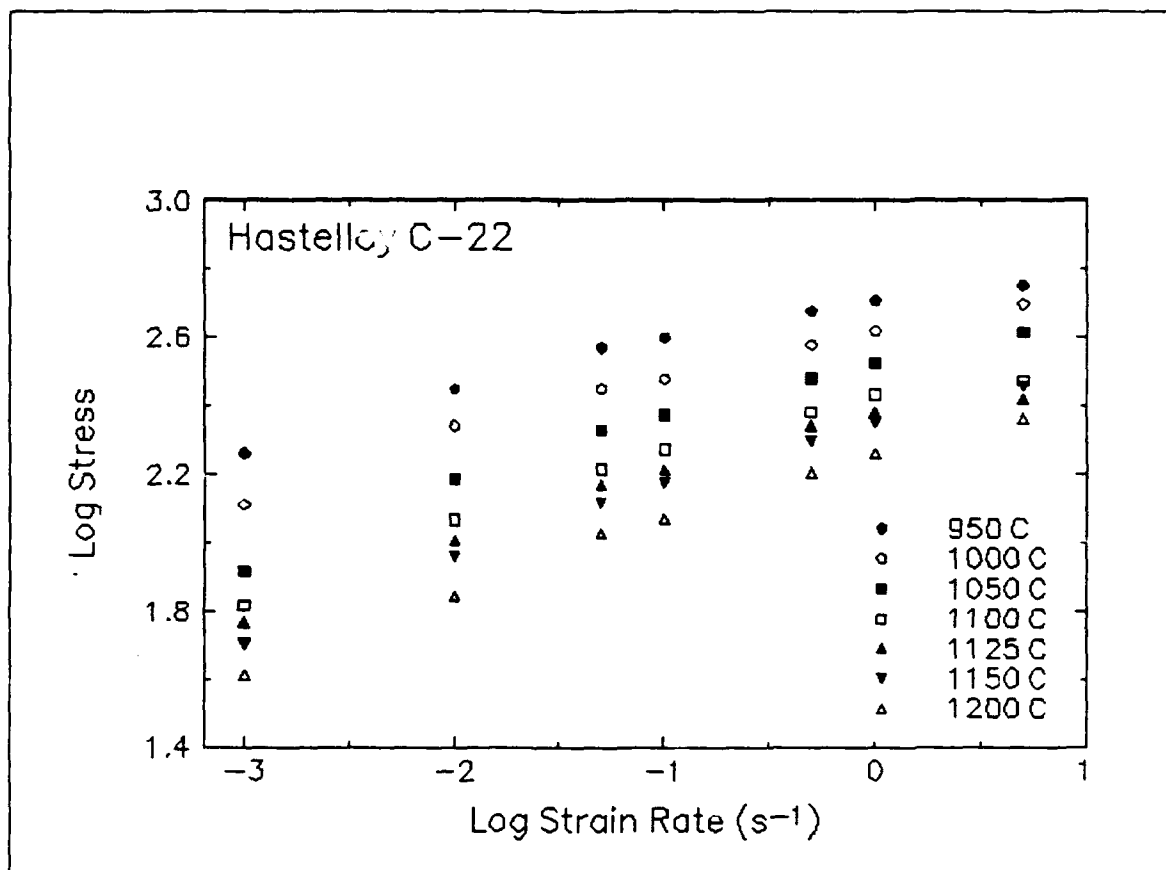Figure 58. Effect of strain rate on stress in log-log scale at a true strain of 0.55 for Hastelloy C-22.
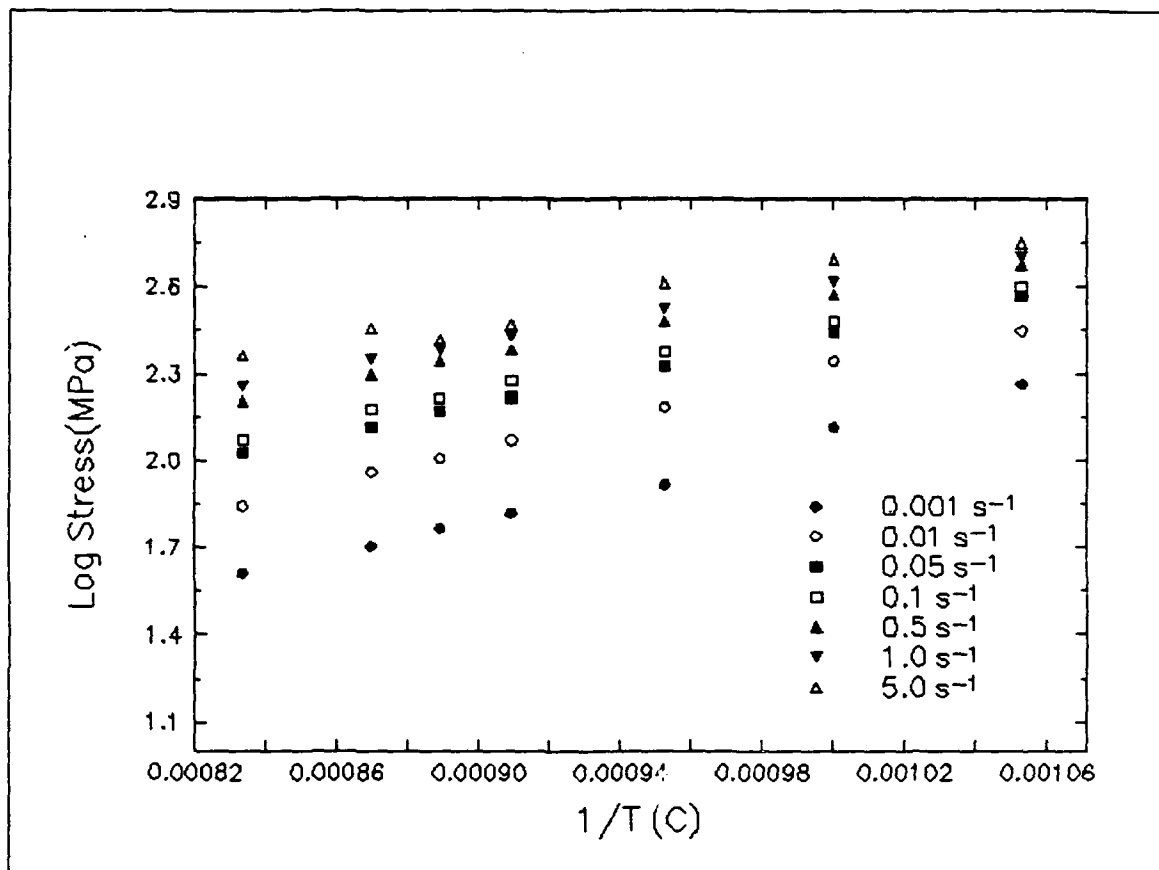
61

Figure 59. Effect of temperature on stress at a true strain of 0.55 for Hastelloy C-22.
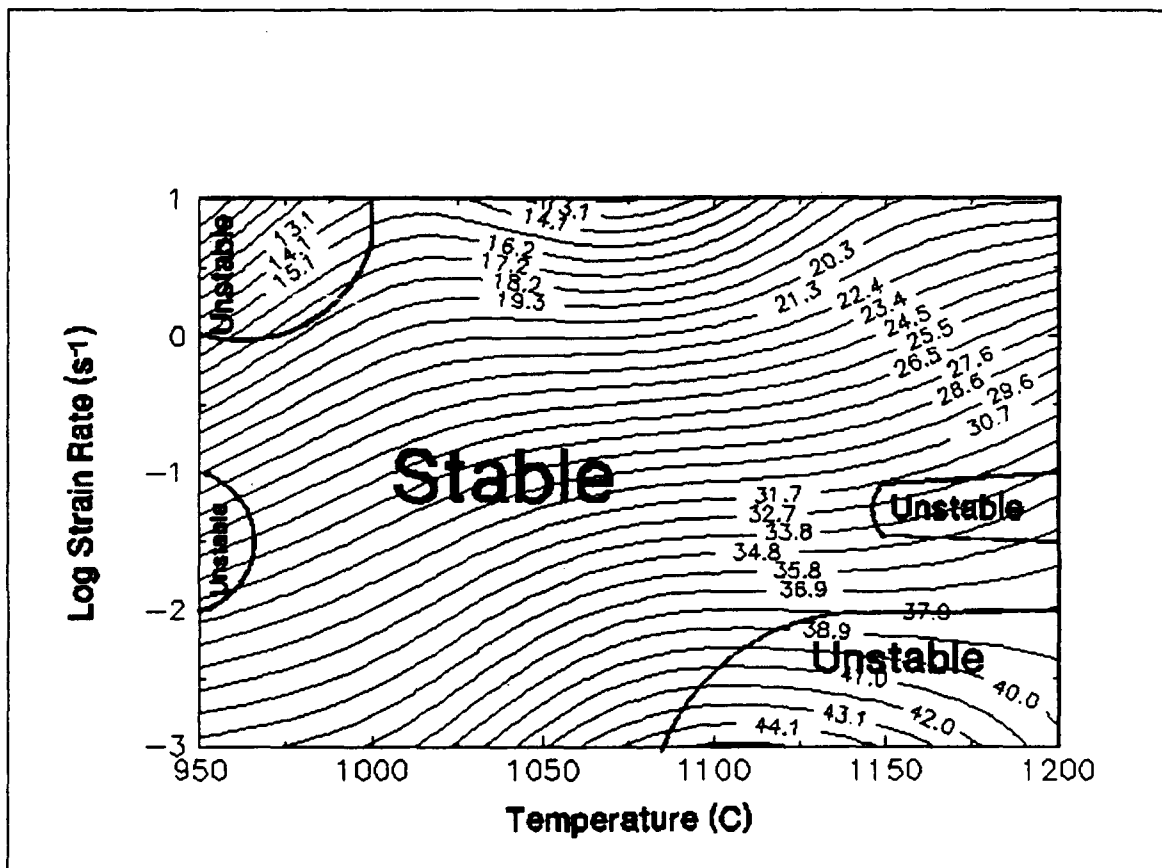
Figure 60. Processing map of Hastelloy C-22 at a true strain of 0.55.

Summary

Compression tests have been performed on Hastelloy C-22 over a wide range of temperatures and strain rates. The experimental conditions used in this work are representative of those used in metalforming practices. From the stress-strain curves, the flow behavior was characterized and a processing map indicating the optimum processing condition was generated. This condition is approximately 1050 C and 0.001 s^{-1}.

The deformed microstructures were characterized from the quenched specimens by optical microscopy and are presented for selective testing conditions together with the stress-strain curves.

Implementation of Data Provided by the Atlas of Formability

The Atlas of Formability program provides ample data on flow behavior of various important engineering materials in the temperature and strain rate regime commonly used in metalworking processes. The data are valuable in design and problem solving in metalworking processes of advanced materials. Microstructural changes with temperature and strain rates are also provided in the Bulletin, which helps the design engineer to select processing parameters leading to the desired microstructure.

The data can also be used to construct processing map using dynamic material modeling approach to determine stable and unstable regions in terms of temperature and strain rate. The temperature and strain rate combination at the highest efficiency in the stable region provides the optimum processing condition. This has been demonstrated in this Bulletin. In some metalworking processes such as forging, the strain rate varies within the workpiece. An analysis of the process with finite element method (FEM) can ensure that the strain rates at the processing temperature in the whole workpiece fall into the stable regions in the processing map. Furthermore, FEM analysis with the data from the Atlas of Formability can be coupled with fracture criteria to predict defect formation in metalworking processes.

Using the data provided by the Atlas of Formability, design of metalworking processes, dynamic material modeling, FEM analysis of metalworking processes, and defect prediction are common practice in Concurrent Technologies Corporation. Needs in solving problems related to metalworking processes can be directed to Dr. Prabir K. Chaudhury, Forming Department Manager of *Concurrent Technologies Corporation*, by calling (814) 269-2594.